UNIVERSITÀ
DEGLI STUDI
FIRENZE

DOTTORATO DI RICERCA IN
FISICA E ASTRONOMIA

CICLO XXX

COORDINATORE Prof. Raffaello D'Alessandro

Coulomb excitation of low-lying states in ^{66}Zn with the SPIDER array

Settore scientifico disciplinare: FIS/04 Fisica nucleare e subnucleare

Dottorando

Dott. Marco Rocchini

Tutore

Prof. Adriana Nannini

Coordinatore

Prof. Raffaello D'Alessandro

Anni 2014 / 2017

To Andolina (my grandmother)

"If I could remember the names of all these particles, I'd be a botanist."

Enrico Fermi

CONTENTS

Overview **1**

1 Introduction **5**

1.1 Models in Nuclear Structure 7

1.1.1 *Ab Initio* Methods 9

1.1.2 Modern Shell Model 11

1.1.3 Mean Field Approaches 13

1.2 Nuclear Observables 13

1.2.1 The Nuclear Shape 15

1.3 Structure of the Zn Isotopes 17

2 Low-Energy Coulomb Excitation **25**

2.1 Theory of the Coulomb Excitation Process 26

2.1.1 First-Order Perturbation Theory 32

2.1.2 Second-Order Perturbation Theory 32

2.2 Quadrupole Sum Rules 34

2.3 Kinematics and Doppler Effect 36

2.4 Experimental Considerations 39

2.5 The GOSIA Code 41

3 Experimental Setup **43**

3.1 The GALILEO Array 44

3.2 The SPIDER Array 46

3.2.1 Study of the Doppler Correction Capabilities 50

3.2.2 SPIDER Commissioning at LABEC 53

3.3 Acquisition System 55

3.4 Event Structure 58

4 Calibrations and Data Reduction **61**
4.1 GALILEO 61
4.1.1 Energy calibration 61
4.1.2 Pileup Rejection 62
4.1.3 Compton Suppression 63
4.1.4 Efficiency Measurement 65
4.2 SPIDER 66
4.2.1 Energy calibration 66
4.2.2 Pileup Rejection 68
4.3 Selection of Coincidences 69
4.3.1 Time Coincidences 69
4.3.2 Multiplicity Selection 72
4.3.3 Particle Energy Selection 72
4.4 Further Applications of the Doppler Correction 73
4.4.1 SPIDER Angles Optimization 75
4.4.2 SPIDER Energy Optimization 77
4.4.3 Particle Energy Without SPIDER 78
4.5 Final γ-particle Coincidence Spectra 79

5 SPIDER Analysis **83**
5.1 Radiation Damage 83
5.1.1 Effects on Energy Spectra and Signal Shapes 87
5.1.2 Conclusions 89
5.2 Pulse-Height Correlation Matrices 91
5.3 Particle Energy Spectra 95
5.3.1 Target Contaminants 97
5.3.2 Target Thickness 99
5.3.3 RBS Measurement at LABEC 100

6 Coulomb Excitation Analysis **105**
6.1 The GOSIA Code Analysis 105
6.1.1 Preliminary Analysis 111
6.1.2 Final Analysis 113
6.2 Comparison with Previous Measurements 117
6.3 Comparison with Model Predictions 118

7 Conclusions and Further Perspectives **123**

Acknowledgements **127**

Bibliography **129**

List of Figures **137**

List of Tables **147**

OVERVIEW

The subject of this thesis is the set up of a new heavy-ion detector for low-energy Coulomb excitation measurements, SPIDER (Silicon PIe DEtectoR), and its first use in an experiment aimed to investigate the structure of the low-lying states in ^{66}Zn.

Low-energy Coulomb excitation is a well-established experimental method to study the electromagnetic properties of low-lying nuclear states such as, for example, transition probabilities and quadrupole moments. These properties are sensitive to the nuclear shape and their study brings us closer to understand the nuclear many-body problem. The basic assumption in the Coulomb excitation method is that the excitation of nuclear states is caused solely by the electromagnetic field acting between the reaction partners, while the contribution of short-range nuclear forces can be neglected. For this reason, the main advantage of the Coulomb excitation method is that, unlike in other nuclear reactions, the interaction process can be described by the well-known theory of the electromagnetic interaction, allowing the nuclear structure to be studied in a model-independent way.

The nuclear chart contains less than 300 stable nuclides along the so-called valley of β stability. About 3000 α- or β-unstable nuclides have been produced in laboratories, and more than 6000 nuclides are thought to be bound by the nuclear force, i.e. stable against proton or neutron emission. At present, experimental nuclear structure studies aim to investigate nuclei far from the valley of β stability and to obtain more accurate and extended data in the entire nuclide chart. It is a vast and very active field of research, in which the technological breakthroughs are twofold: advances in the accelerators and ion sources on the one hand, and in the detectors for the experiments on the other.

Advances in accelerator and ion-source technologies have made it possible to produce Radioactive Ion Beams (RIBs) and have thus opened many horizons to investigate the structure of exotic nuclei. Coulomb excitation is a powerful tool in such studies, as the low intensities of currently available exotic beams can be compensated by the large

cross-section of the excitation process. The Selective Production of Exotic Species (SPES) facility [1], currently under construction at INFN Laboratori Nazionali di Legnaro (LNL), aims to produce RIBs using the Isotope Separation OnLine (ISOL) technique with a particular focus on neutron-rich beams in the vicinity of ^{78}Ni and ^{132}Sn, where detailed nuclear structure information is scarce. The development of an experimental setup to perform low-energy Coulomb excitation measurements at LNL, which typically consists of an array of γ–ray detectors coupled to a segmented charged particle detector, represents a crucial requirement for the SPES project. To this end, SPIDER has been developed to be used in conjunction with state-of-the-art γ–ray detector arrays, such as GALILEO (Gamma Array of Legnaro Infn Laboratories for nuclEar spectrOscopy [2]) and AGATA (Advanced GAmma Tracking Array [3]).

The preliminary tests performed at the INFN division of Firenze, including an in-beam commissioning using a ^{7}Li beam at LABEC (LAboratorio di tecniche nucleari per i BEni Culturali), are presented in this thesis. The results obtained from the laboratory and in-beam tests have been used in order to choose the detector design and the related electronics. SPIDER is easily assembled in the GALILEO vacuum chamber and can also be rapidly dismounted to be replaced by other ancillary devices. The planning and the data analysis of the first Coulomb excitation experiment of SPIDER, performed coupling the heavy-ion detector with the GALILEO γ–ray spectrometer recently installed at LNL, are also described. The methods for the calibration of the detectors and the data reduction process have been implemented during this thesis, starting from the existent GALILEO data analysis software based on the CERN Root suites of codes [4]. An accurate on-line monitoring of the Coulomb excitation experiment is now possible with the SPIDER and GALILEO set up, thanks to the various data structures that are available in the data sorting.

The Coulomb excitation of ^{66}Zn was the first physics experiment with this new setup. High-precision measurements of transition probabilities and spectroscopic quadrupole moments for the first excited states of this nucleus have been achieved, analysing the data with the Coulomb excitation code GOSIA [5]. Using this data, it has been possible also to obtain the intrinsic shape of ^{66}Zn in its first two 0^{+} states. The isotope was carefully chosen: some nuclear observables were known with high accuracy, offering the possibility to have a stringent test for the setup. However, some observables necessary to the ^{66}Zn structure description had never been measured, and, for others, conflicting results were available in the literature. For this reason, the results obtained in this work represent an important benchmark to test state-of-the-art shell model and "beyond mean field" calculations, typically used to interpret the structure of the stable zinc nuclei.

Radiation damage and cross-talk/charge-sharing effects induced by energetic heavy

ions in segmented silicon detectors have been also investigated, thanks to the high flexibility of the data acquisition system of GALILEO, in which SPIDER has been fully integrated. The results coming from the radiation damage analysis will help to optimize the beam current in future experiments.

The SPIDER geometry has been also included in the existent GEANT4 [6] simulation package of GALILEO and in the input file of the Coulomb excitation GOSIA code. It is now possible to perform a full simulation of a planned experiment by including γ–ray yields estimated using GOSIA into the GEANT4 code. A simplified Monte Carlo code has been developed, to estimate the resolution of the γ–ray peak in a faster way with respect to the full GEANT4 simulation.

All the methods that are used and described in the present thesis have been implemented with the idea of supplying useful tools to plan and analyse future experiments with SPIDER.

This work provides the opportunity of performing Coulomb excitation measurements using the SPIDER and GALILEO arrays with the high-quality stable beams currently available at the Tandem-ALPI-PIAVE accelerator complex at LNL, paving the way to experimental campaigns with the radioactive beams that will be provided by the SPES facility at LNL.

* * *

The thesis is organized as follows: **chapter 1** introduces the general framework of this work, describing some of the theoretical approaches currently used in nuclear structure and the nuclear observables relevant in the considered experiment. The structure of the zinc isotopes is also discussed in detail. The low-energy Coulomb excitation technique is described in **chapter 2**, focusing on the main aspects that are relevant for the ^{66}Zn experiment. The experimental setup composed by SPIDER and GALILEO is presented in **chapter 3**, with particular attention to the choice of the SPIDER design and the tests performed for this detector. The acquisition system and the event structure of the acquired data used in the ^{66}Zn experiment are also presented. Since this was the first experiment using SPIDER coupled to GALILEO, a detailed description of calibrations and data reduction is provided in **chapter 4**. In **chapter 5** the SPIDER response during and after the experiment is discussed, while the final Coulomb excitation analysis is presented in **chapter 6**, together with a comparison of the obtained results with state-of-the-art shell model and "beyond mean field" calculations.

CHAPTER 1

INTRODUCTION

The most ambitious goal of nuclear structure physics is to describe the fundamental properties of all the atomic nuclei, starting from their building blocks, protons and neutrons.

Despite the fact that Ernest Rutherford first discovered the atomic nucleus over a hundred years ago (1911), we are still far from a comprehensive understanding of this system. Only about half of the predicted bound nuclei have been observed up to date; moreover, exhaustive experimental data are available only for some nuclei close to the stability valley. From the theoretical point of view, several models have been developed to describe the complexity of this quantum many-body system, characterized by strong correlations. In order to extend our understanding of nuclear structure, considerable efforts are now pursued, from both the experimental and theoretical points of view.

The development of facilities capable to accelerate RIBs is of primary importance in this context. The use of RIBs offers the possibility to perform experiments with nuclei far from the stability valley and, therefore, to populate nuclei in mass regions not accessible to stable ion beams. The main techniques used to produce RIBs are the in-flight production and the ISOL. In the former case, a primary heavy-ion beam accelerated at intermediate or relativistic energies (from $\sim$ 50 MeV up to $\sim$ 1.5 GeV) impinges on a thin target. The products of the reaction (typically fragmentation) exit from it with an energy close to the one of the primary beam, and are identified in mass and charge using an electromagnetic spectrometer. To date, in the ISOL technique, a thick target is bombarded with light charged-particles or a neutron beam. The reaction products are extracted as ions, selected in mass by an electromagnetic separator and then accelerated. The two techniques are in many aspects complementary. For instance, with the in-flight technique it is possible to obtain RIBs composed by nuclei with short lifetimes (down to about $\sim$ 100 ns), but the

final beam contains several nuclear species. The ISOL technique requires more time to extract the products from the target, therefore only RIBs of species with half-lives in the range of ~ 1 ms or grater can be produced. However, thanks to the high selectivity of the ionizing process combined with the mass separation, these RIBs are generally more pure than the ones produced with the in-flight technique and the use of a post-acceleration stage offers high quality in terms of energy and focusing, comparable to that achieved with stable beams. Radioactive beam facilities such as ISOLDE (Isotope Separator On-Line DEvice [7]) at CERN (Switzerland), ISAC (Isotope Separator and ACcelerator [8]) at TRIUMF (Canada) and RIBF (Radioactive Isotope Beam Factory [9]) at RIKEN (Japan) are already operative. An ISOL facility, SPES, is currently under construction at INFN LNL. The use of the existent superconducting ALPI (Acceleratore Lineare Per Ioni [10]) linac at LNL enables to achieve post-accelerated energies above 10 MeV/A and a mass separator with high resolution (1/20000) will increase the number of RIBs at high purity. Beam intensities of $10^7 - 10^8$ particles per second in a wide range of mass ($60 < A < 160$) are finally expected.

The low-energy Coulomb excitation technique represents one of the most used methods to study the collectivity of short-lived nuclei far from the stability valley. Experiments using this technique are likely to be the first ones to be performed with the post-accelerated SPES beams (as it happened at other ISOL facilities, such as ISOLDE).

Alongside with the development of new RIB accelerators, the improvement of detection systems plays a crucial role in the nuclear structure investigation, in which γ–ray spectroscopy is one of the most used methods. The last generation of γ–ray detector array uses highly-segmented germanium crystals and sophisticated tracking algorithms to reconstruct the trajectories of the incident γ–rays. In this way, high efficiency and resolution can be achieved. One of these arrays is AGATA [3] which, in its final configuration, will consist of 180 encapsulated high-purity germanium crystals (9 cm length, 8 cm diameter), each subdivided into 36 segments. AGATA belongs to an European collaboration and it is shared among European laboratories. At present, it is installed at GANIL (France) and it will return to LNL when SPES will be operative. A stationary γ–ray detector array, GALILEO (which will be described in detail in section 3.1), has been developed at LNL using tapered HPGe detectors. GALILEO has been coupled to a variety of ancillary detectors, among which SPIDER, implemented during this thesis, has been designed for low-energy Coulomb excitation measurements.

In this chapter, some of the modern theoretical approaches used for the description of the nuclear structure are introduced (1.1), the observables interesting for the ^{66}Zn experiment are defined (1.2) and the structure of zinc isotopes is discussed, focusing on ^{66}Zn (1.3).

1.1 Models in Nuclear Structure

Closed-form analytical solutions for the N-body problem are not possible already considering $N = 3$, both in classic and quantum mechanics. Many different approaches have been developed in order to overcome this difficulty, very often shared between different fields of physics. The general idea adopted to describe an N-body system can be summarized in the following steps.

1. **The choice of the relevant degrees of freedom which characterize the system**. In the nuclear structure case, it is possible to neglect the behaviour of the constituents of the nucleons, the quarks, and the contribution of the atomic electrons. This is due to the fact that the nuclear structure energy scale can be confined in the range of $\sim 1 - 100$ MeV, while the Quantum ChromoDynamics (QCD) binding energy is nearly the 99% of the nucleon mass (~ 1 GeV) and the atomic ionization energies are of the order of $\sim 1 - 100$ eV.

2. **The description of the interaction between the constituents**. This is one of the most problematic steps in the nuclear structure case. While the gravitational and electromagnetic forces are nowadays well known, respectively from the theory of general relativity and from Quantum ElectroDynamics (QED), the strong Nucleon-Nucleon (N-N) interaction is still not completely understood. Simple interacting systems, such as two single nucleons, are already complicated to describe. In the case of the QCD also the force carriers, the gluons, interact with each other, since they have a color charge. This is a crucial difference with respect to the QED case, in which the force carriers, the photons, have no electric charge. Moreover, even if the N-N interaction of two free nucleons could be described, a nucleon inside a nucleus resides in the mean-field which is due to the average interaction between all the nucleons, and also the Pauli principle has to be taken into account. Different approaches have been used in order to describe an effective N-N interaction, such as the development of realistic interactions based on the known properties of the strong force (one of the first notable examples is the Yukawa potential [11]), phenomenological interactions characterized by many parameters fitted to the experimental data (the Gogny [12] and Skyrme [13] forces are two of the most used to date) and interactions having the most general possible form consistent with all the symmetries which the system has to respect (one of the most promising classes of interactions of this kind are the ones obtained from the chiral Effective Field Theory (EFT) which is built on the symmetries of QCD).

3. **The definition of a method which is capable to overcome the intrinsic**

many-body description difficulties. The mean-field approximation is an example of a method which is shared by many models of the nuclear structure. The Hamiltonian of the system can be written as the sum of kinetic and interaction terms:

$$H = \sum_i T(i) + \sum_{i<j} V^{(2)}(i,j) + \sum_{i<j<k} V^{(3)}(i,j,k) \tag{1.1}$$

where the summations extend to all the nucleons and only two-body $V^{(2)}$ and three-body $V^{(3)}$ interactions are considered. The $V^{(3)}$ terms have been usually neglected in the past; however, their importance has been recently pointed out in several works [14,15]. One of the common approaches used to solve the Schrödinger equation of the atomic nucleus is the description of the motion of a single nucleon in a mean potential generated by all the others. This can be achieved by adding and subtracting an auxiliary one-body potential U to the Hamiltonian of the system. Considering, for simplicity, only the two-body interactions:

$$H = \left[\sum_i T(i) + \sum_i U(i)\right] + \left[\sum_{i<j} V^{(2)}(i,j) - \sum_i U(i)\right] \equiv H_0 + H_{res} \tag{1.2}$$

in this way the Hamiltonian is decomposed in two terms, one which describes the independent motion of the nucleons (H_0) and a residual interaction which is usually small compared with the first term (H_{res}). The nucleons can be thus considered as independent particles in a common mean field, while H_{res} can be treated as a perturbation.

These three steps are, for instance, on the basis of the shell model developed from the early fifties to describe the shell structure of the atomic nucleus. The shell closures are, similarly to the atomic case, characterized by magic numbers for protons and neutrons, and present enhanced stability which is reflected, for instance, in high excitation energies of the first excited states and relatively small transition probabilities. Other models, such as the liquid drop model [16], the vibrational/rotational models [16] and the Geometric Collective Model (GCM) [18] are based on a different approach, describing the nucleus on the basis of its collective behaviour. The shell and collective models are built on a phenomenological approach, their goal being to reproduce selected properties of nuclei. Other models, such as the Nilsson one [19], which is essentially an extension of the shell model to axially deformed nuclei, try to combine the macroscopic and microscopic degrees of freedom, while algebraic models, such as the Interacting Boson Model (IBM [20]) developed by Iachello and Arima, are based on group theory.

The recent access, from the experimental point of view, to more precise and reliable spectroscopic data, together with the development of new facilities that give the opportunity to study nuclei far from the valley of the stability, have shown new intriguing features

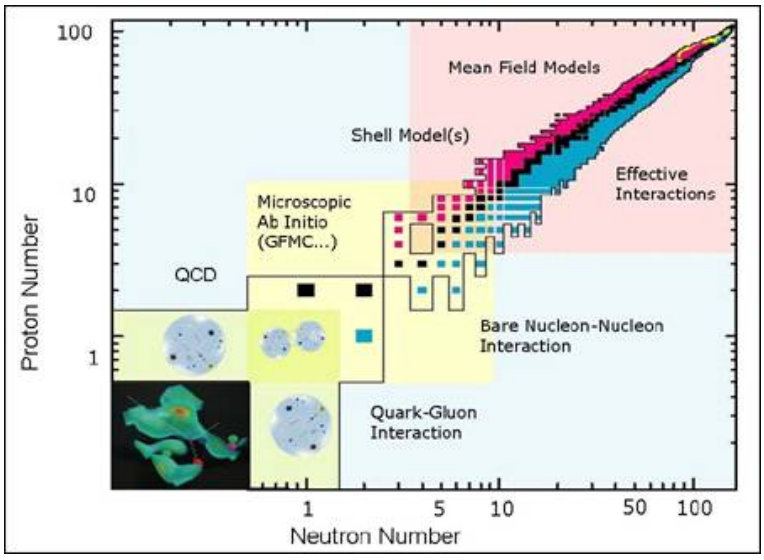

Figure 1.1: Logarithmic nuclide chart in which the regions of applicability of some of the modern theoretical approaches, used to describe the nuclear structure, are shown. To date, ab initio approaches are being extended up to heavy mass nuclei, as shown in figure 1.2. Figure taken from [17].

about nuclear structure. The necessity of high precision methods, capable to describe the nuclear properties in different region of mass, is therefore highly desirable.

In the following, the basic ideas of three of the most promising modern theoretical approaches [21] will be briefly presented[1]: the *ab initio* methods, the modern shell model and the mean-field approaches (their applicability regions are shown in figure 1.1). The last two will be used to analyse the results of the ^{66}Zn experiment discussed in this thesis (*ab initio* methods cannot be applied, at present, to Zn isotopes, due to the large number of involved nucleons).

1.1.1 *Ab Initio* Methods

As already mentioned above, the most commonly used approach to tackle the nuclear many-body problem is the use of an empirical approximation capable to simplify the description of the system. In spite of the great success obtained by these approaches in the study of the atomic nuclei, new efforts have been made in the last two decades to directly solve the Schrödinger equation without the introduction of any additional parameter. Many of the developed techniques are shared by different fields of physics (quantum chemistry, ultracold atomic and molecular systems, quantum dots and others). The exact

[1]The contents of the three discussed approaches are mainly taken from: [22] for the *ab initio* methods, [23] for the realistic shell model and [24] for the "beyond mean field" approaches.

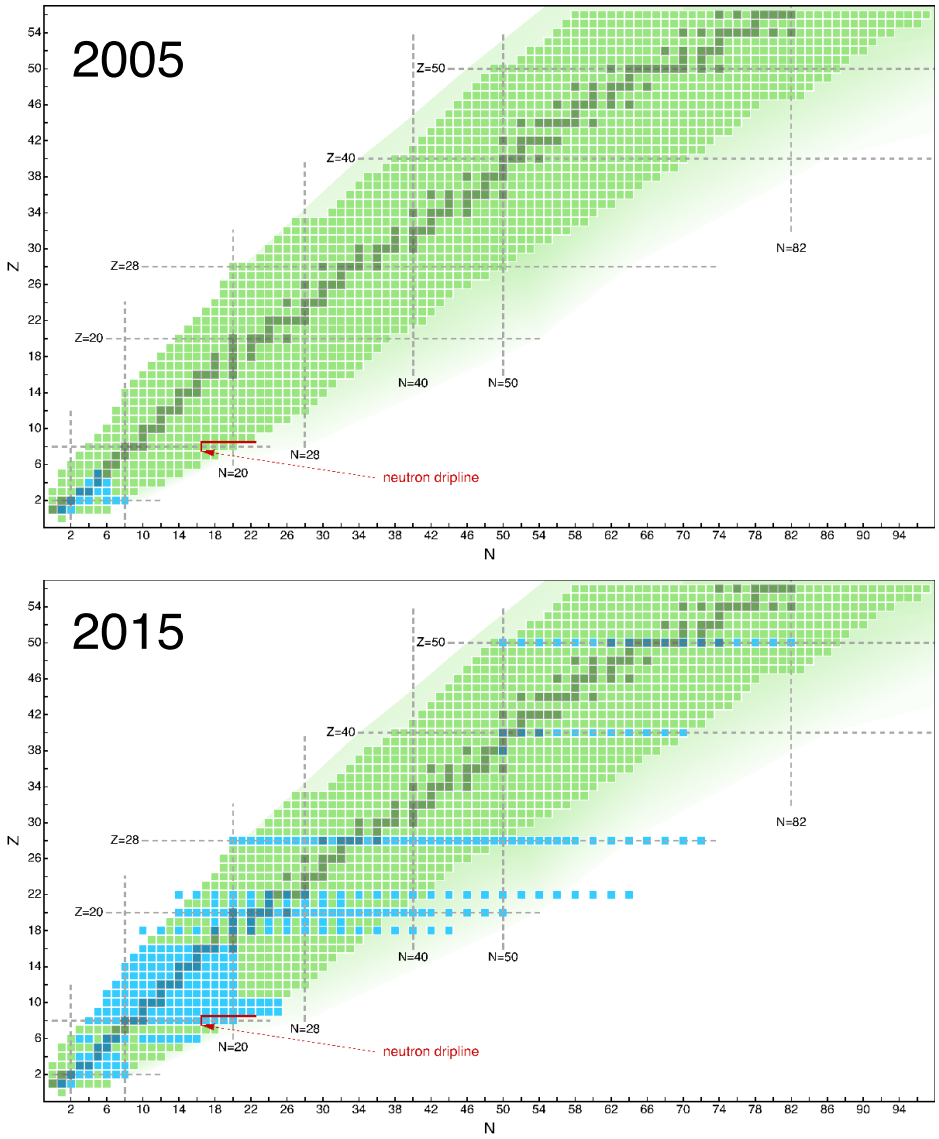

Figure 1.2: Nuclides chart with the reach of *ab initio* calculations in 2005 and 2015. Nuclei (including potentially unbound isotopes), for which *ab initio* calculations based on high-precision nuclear interactions exist, are highlighted. Figure taken from [25].

definition of an *ab initio* method is often discussed, however, in a very general picture, it consists of a method which enables to obtain quantum observables by solving the many-body equations, without any uncontrolled approximation. Controlled approximations are allowed if it is demonstrated that a convergence limit in the calculated observable values is reached. All the relevant degrees of freedom of the system have to be considered and the internal relative motion has to be correctly treated.

Since no additional parameters are introduced, these methods are particularly suitable to test the nuclear interaction. The observation of the importance of the three-body forces is one of the main results of the *ab initio* methods, applied to atomic nuclei.

The obvious limit of these methods is related to the complexity of the system which must be considered. To date, heavy nuclei, with a large number of nucleons, are impossible to describe. However, numerical methods such as Monte Carlo calculations can be applied to study the most complicated cases. Figure 1.2 shows the progress which have been made in the last decade using this approach.

1.1.2 Modern Shell Model

The nuclear Shell Model (SM) has been developed since the early fifties to the present day. Within this model, the complexity of the many-body problem (point 3 discussed above) is simplified by the empirical evidence for shell structure in nuclei (see figure 1.3). The system is approximated to an inert core composed of closed shells (doubly magic nucleus), which are filled up with neutrons and protons paired to angular momentum $J = 0$, plus a certain number of "valence" nucleons outside the magic shells that are constrained to move in a truncated Hilbert space, the so-called "model space". The SM Hamiltonian, acting only between the valence particles, should account for the neglected degrees of freedom, namely those of the core particles as well as of the excitations of valence particles above the chosen model space. To this end, one can resort to empirical interactions, requiring fitting procedures to reproduce the experimental data, or to the so-called "realistic effective interaction", derived from the free the N-N potential by means of many-body techniques.

Although the modern shell models show detailed and precise descriptions of many nuclear properties, severe computational difficulties arise when dealing with increasing number of valence particles in large model spaces. As in the case of the *ab initio* methods, Monte Carlo calculation techniques have been applied in the recent years (Monte Carlo Shell Model, MCSM), to extend the model to the interpretation of heavy nuclei.

Significant progress have been made within the realistic SM framework in the last 3 decades and a number of calculations has been performed using various N-N potentials, such as the CD-Bonn [26] or the Argonne [27] potentials, or those based on chiral perturbation theory [28]. Almost all the interactions, due to the presence of a strong short-range part, cannot be used directly in the derivation of the SM effective interaction. The effort to overcome this difficulty has resulted in the development of the G-matrix method [29] and the more recent V_{low-k} approach [30], which give an effective interaction within the nuclear medium removing the effects of the short-range repulsive core of the N-N potentials (the same problem is obviously shared with the *ab initio* methods when realistic interactions are considered). Many refinements have been applied over the years, among the others the inclusion of the three-body forces.

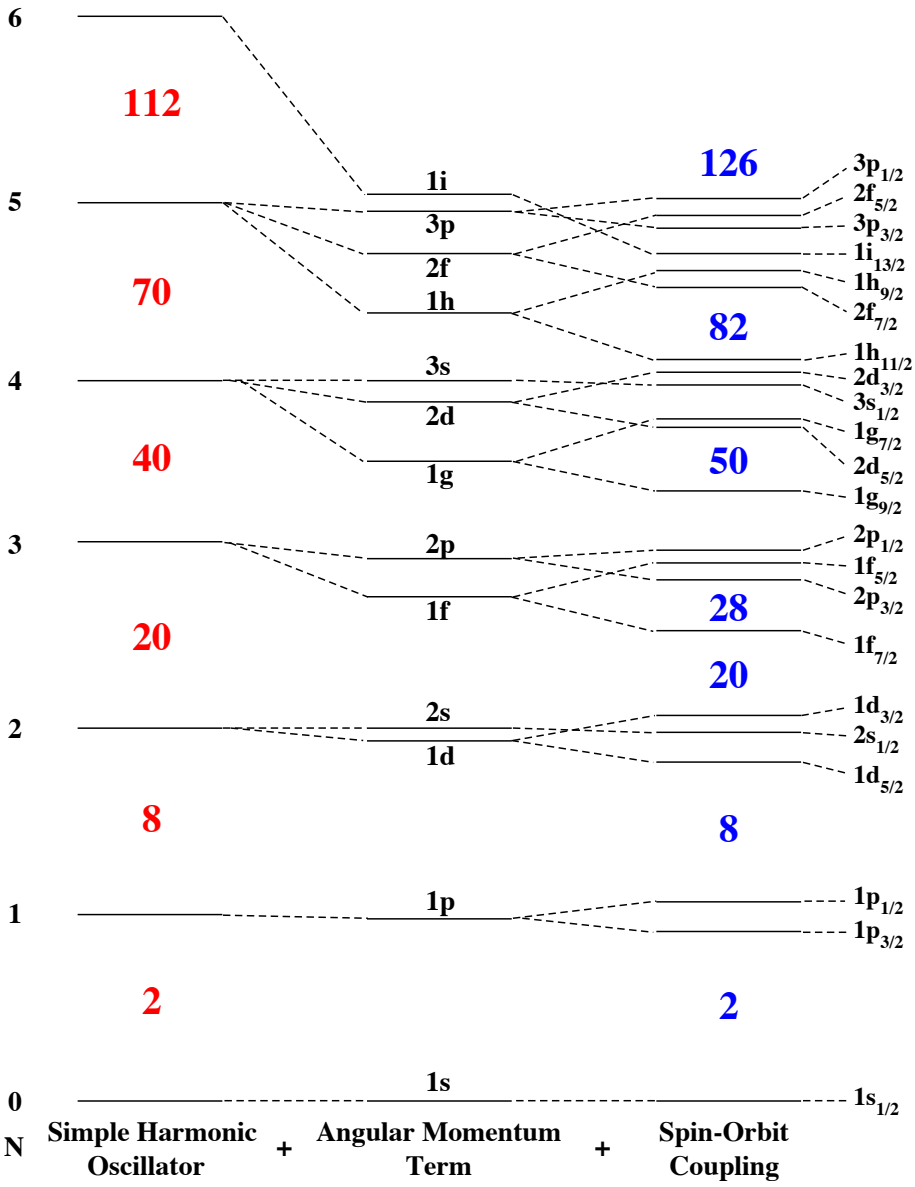

Figure 1.3: Schematic diagram of single-particle energy levels for spherical shell model. The break of degeneracy caused by the angular momentum and spin-orbit terms, which produces the emergence of the magic number in the shell closure, is also visible. The energy values in the first set are the ones of the simple harmonic oscillator. Figure taken from [31].

1.1.3 Mean Field Approaches

The basic idea of the mean field is based on the fact that, as a starting point, the nucleons composing the nucleus can be considered independent particles which feel a common, mean, potential. The Hartree-Fock (and its Hartree-Fock-Bogoliobov extension, which includes the pairing[2] effects) is the most general example of these approaches. The basic assumption is that the nuclear wave function can be approximated by a Slater determinant, which respects the Pauli principle. Then, it is assumed that there is a one-to-one correspondence between the external potential (i.e. the mean-field), the ground-state wave function of the system and its density. In this way, it is possible to express the energy of the ground state as a density functional (Energy Density Functional EDF), which can be minimized using the variational principle. One of the main challenges (which is also the final goal) is to define an EDF that is suitable to describe nuclei in the entire nuclide chart. Very often this is deduced from empirical forces, such as the Gogny [12] and Skyrme [13] ones. Within the mean field approach, it is possible to calculate ground state properties such as masses, radii and shapes of heavy nuclei. In particular, the precision of the calculations increases with the number of considered nucleons, as opposed to the previously discussed methods.

In order to obtain precise calculations also for the excited states, the model has to be extended to include correlations between particles (i.e. the wave function must be improved in order to deal with H_{res}). This is done in the so-called "Beyond Mean Field" (BMF) models. One of the ways to obtain this extension is to select degrees of freedom, to which the energy is especially sensitive, to be used as coordinates to generate correlated wave functions. This is the basic idea of the Generator Coordinate Method (GCM), which has been demonstrated to be a powerful tool to calculate both ground state and excited state properties. Within this approach it is possible, in principle, to obtain the solution of the nuclear many-body problem. However, due to computational limitations in realistic cases, it is more practical to consider only the relevant degrees of freedom that are of interest.

1.2 Nuclear Observables

In this section, the observables that characterise the atomic nucleus will be introduced, focusing on the ones which can be obtained using the low-energy Coulomb excitation

[2]The pairing interaction is a part of the nuclear force which is attractive and acts only on two identical particles in total angular momentum 0^+ states. It is responsible, for instance, of the fact that the ground state of all even-even nuclei has $J = 0^+$ and of the superfluidity phenomena in nuclei [19, 32].

technique.

A nucleus can be found in different quantum states characterized by energy, angular momentum and parity. The study of the discrete spectrum associated with the excited states provides information about the nuclear structure. The energy, the spin and the parity of the states can be obtained by measuring the energies, intensities, angular distributions and polarizations of the γ–rays emitted by the nucleus during its de-excitation. In order to obtain further and precise indications about the nuclear microscopic and macroscopic degrees of freedom, it is useful to measure also transition probabilities and electromagnetic static moments of the excited states.

Most of the experimental information that have been obtained about the nuclear excited states derive from studies concerning not the strong nuclear interaction, but the much weaker (and better understood) electromagnetic interaction. It is well known how the electromagnetic field can be decomposed by a multipole expansion into components, each carrying a definite angular momentum L (2^L is the multipole order). A transition with associated angular momentum L can be distinguished to have an electric (EL) or magnetic (ML) multipolarity. The parity associated to the multipoles are:

$$\pi\left(EL\right) = \left(-1\right)^{L} \qquad \pi\left(ML\right) = \left(-1\right)^{L+1} \tag{1.3}$$

Considering a γ–ray emitted by a nucleus in the de-excitation from an initial state of angular momentum J_i and parity π_i, to a final state with J_f and π_f, the conservation of the angular momentum and parity requires the following rules:

$$\left|J_i - J_f\right| \leq L \leq J_i + J_f \qquad (no\ L = 0) \tag{1.4}$$

and

$$EL:\ \pi_i \cdot \pi_f = \left(-1\right)^{L} \qquad ML:\ \pi_i \cdot \pi_f = \left(-1\right)^{L+1} \tag{1.5}$$

for electric and magnetic multipoles, respectively. The reduced transition probability for an electromagnetic transition of multipolarity Ω (electric E or magnetic M) can be expressed as

$$B\left(\Omega L; J_i \longrightarrow J_f\right) = \frac{1}{2J_i + 1}\left|\left\langle J_f \left|\left|M\left(\Omega L\right)\right|\right| J_i\right\rangle\right|^2 \tag{1.6}$$

where $M\left(\Omega L\right)$ is the electromagnetic operator. $B\left(EL\right)$ values are typically expressed in $e^2\mathrm{fm}^{2\mathrm{L}}$, while $B\left(ML\right)$ values in $\mu_N^2\mathrm{fm}^{2(\mathrm{L}-1)}$ where e is the electron charge and μ_N is the nuclear magneton. In both cases, barns units are also used instead of fm (1 b=100 fm^2). The Weisskopf estimates of the γ-decay probabilities, which give the possibility to compare different transition probabilities related to different nuclei and to different multipoles, are

expressed as:

$$EL: \ \ 1 \text{ W.u.} = \frac{1}{4\pi}\left(\frac{3}{\mathrm{L}+3}\right)^2 \left(1.2\mathrm{A}^{1/3}\right)^{2\mathrm{L}} \ e^2\mathrm{fm}^{2\mathrm{L}} \tag{1.7}$$

$$ML: \ \ 1 \text{ W.u.} = \frac{10}{\pi}\left(\frac{3}{\mathrm{L}+3}\right)^2 \left(1.2\mathrm{A}^{1/3}\right)^{2\mathrm{L}-2} \ \mu_{\mathrm{N}}^2\mathrm{fm}^{2(\mathrm{L}-1)} \tag{1.8}$$

The decay rate T for a transition of multipolarity Ω, expressed in Hz, is given by

$$T\left(\Omega L; J_i \longrightarrow J_f\right) = \frac{8\pi\left(L+1\right)}{L\left[(2L+1)!!\right]^2}\frac{1}{\hbar}\left(\frac{E_\gamma}{\hbar c}\right)^{2L+1} B\left(\Omega L; J_i \longrightarrow J_f\right) \tag{1.9}$$

where E_γ is the energy of the emitted γ–ray. The lifetime τ of a state is the inverse of the sum of the partial decay rates, considering all the possible final states and the different multipolarities that are involved. In the case of an $E2$ transition from a first excited state 2_1^+ to a ground state $0_{g.s}^+$ the relation is simply

$$\tau = \frac{1}{T\left(E2; 2_1^+ \longrightarrow 0_{g.s}\right)} \tag{1.10}$$

If a transition can have more than one multipolarity ΩL, for instance if both an $E2$ or an $M1$ transition is allowed by the selection rules, the mixing ratio δ can be defined as the ratio between the decay rates associated to the different multipolarities.

1.2.1 The Nuclear Shape

The nuclear shape can be expressed in a reference system fixed with the laboratory as follows:

$$R\left(\theta,\phi\right) = R_0\left[1 + \sum_{\lambda\mu}\alpha_{\lambda\mu}Y_{\lambda\mu}^*\left(\theta,\phi\right)\right] \tag{1.11}$$

where R_0 is the radius of a spherical nucleus with an equivalent volume, $Y_{\lambda\mu}$ are spherical harmonics as a function of the polar and azimuthal angles and $\alpha_{\lambda\mu}$ are spherical tensor components (transform as spherical harmonics under rotation of the coordinate system). The index λ indicates the type of deformation and $\mu = -\lambda, ..., \lambda$. Considering quadrupole deformations $\lambda = 2$ (the most frequent in the nuclei), the nuclear shape is characterized by five degrees of freedom: $\alpha_{2\mu}$ with $\mu = -2, -1, 0, 1, 2$. Three of these can be used to transform the reference system into the intrinsic one (fixed with the nucleus), by means of the Euler angles θ_1, θ_3, θ_3. This may be expressed formally by transforming the $\alpha_{2\mu}$ parameters using the following expression:

$$\alpha_{\lambda\mu} = \sum_{\nu=-2}^{2} a_{\mu\nu}D_{MK}^J\left(\theta_1,\theta_2,\theta_3\right) \tag{1.12}$$

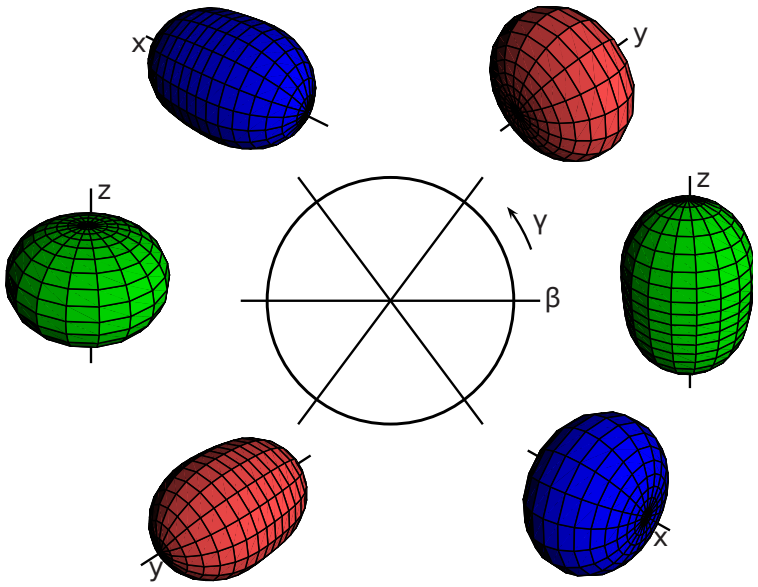

Figure 1.4: Quadrupole deformed shapes as a function of the Hill-Wheeler parameters. Different colors identify the axes of the intrinsic reference frame (green for z, red for y and blue for x). Figure taken from [33].

where $D^J_{MK}(\theta_1, \theta_2, \theta_3)$ is a rotation operator [16]. The remaining two degrees of freedom can be described by the parameters $a_{2,0}$ and $a_{2,2}$ ($a_{2,-2} = a_{2,2}$ and $a_{2,-1} = a_{2,1} = 0$). Instead of $a_{2,0}$ and $a_{2,2}$, the Hill-Wheeler parameters β and γ are typically used, defined as $a_{20} \equiv \beta \cos\gamma$ and $a_{22} \equiv \beta/\sqrt{2}\sin\gamma$. In this way, the nuclear shape in the intrinsic reference system for $\lambda = 2$ can be expressed as follows:

$$R(\theta, \phi) = R_0 \left[1 + \beta\sqrt{\frac{5}{16\pi}}\left(\cos\gamma\left(2\cos^2\theta - 1\right) + \sqrt{3}\sin\gamma\sin^2\theta\cos 2\phi\right)\right] \tag{1.13}$$

The β parameter is related to the extent of the deformation, while γ is related to the axial symmetry of the system. For instance, $\beta = 0$ corresponds to a spherical shape, and $\gamma = 0$ to an axially symmetric shape. Figure 1.4 shows the different shapes associated to different β and γ values. Due to the rotational symmetry of the system, it is sufficient to consider only $0° < \gamma < 60°$.

As previously shown, the off-diagonal matrix elements of the multipole operators are related to the transitions between different excited states. The diagonal matrix elements describe the transitions between the magnetic sub-states and are related to static moments. In particular, the diagonal $E2$ matrix element is related to the spectroscopic electric quadrupole moment Q_s, which can be expressed as follows:

$$Q_s(J) = \sqrt{\frac{16\pi}{5}}\frac{\langle JJ20|JJ\rangle}{\sqrt{2J+1}}\langle J\,||E2||\,J\rangle \tag{1.14}$$

where $\langle JJ20|JJ\rangle$ is a Clebsch–Gordan coefficient. The spectroscopic quadrupole moment is defined in the laboratory frame and provides an estimate of the non-sphericity of the nucleus in a given excited state. However, it cannot be immediately related to the nuclear shape, which is defined in the intrinsic frame. A typical example is a prolate deformed nucleus rotating at high frequency around an axis perpendicular to its axis of symmetry: an overall oblate deformation appears in the laboratory frame in this case. In order to obtain an indication of the deformation for axially symmetric nuclei, the intrinsic quadrupole moment Q_0 is defined (in the framework of the rotational model) as follows:

$$Q_s(J) = \frac{3K^2 - J(J+1)}{(J+1)(2J+3)} Q_0(J) \tag{1.15}$$

where K is the projection of the angular momentum J on the symmetry axis of the nucleus. The sign of Q_0 is positive for prolate shapes and negative for oblate shapes. It is also apparent that $Q_0 = 0$ if $J = 0$, thus this quantity cannot give any information about the shape of a 0^+ state, which is, by the way, the ground state of all the even-even nuclei.

The shape of the nucleus is not directly observable, but it can be studied by comparing the experimental results with model predictions. An alternative approach to obtain an indirect measurement of the Hill-Wheeler parameters in a model-independent way will be presented in section 2.2. Actually, due to the quantum nature of the nucleus, this corresponds only to a measurement of the mean shape. The possible diffused character (also called "softness") in both the parameters, can be also deduced with the same method.

At this stage, it is good to stress again how the quadrupole deformations are related to the properties of the $E2$ operator. If more complicate shapes are of interest, such as octupole or hexapole, the same treatment can be repeated referring to the $E3$ and $E4$ operators.

1.3 Structure of the Zn Isotopes

The microscopic and macroscopic degrees of freedom are both relevant in the structure of the zinc isotopes. Having only two protons outside the shell closure at $Z = 28$, it is possible not only to apply mean field models but also to perform realistic microscopic calculations using shell model. For these reasons, Zn isotopes have been widely investigated in the past and continue to attract much attention from both the experimental and the theoretical point of view.

Many collective phenomena have been predicted and observed in these isotopes. At first, even-even Zn nuclei have been interpreted within the collective vibrational model [34]. A comparison between the first low-lying levels of ^{66}Zn and the vibrational model level scheme is shown in figure 1.5. The mean energy of the 0_2^+, 2_2^+, 4_1^+ triplet is about

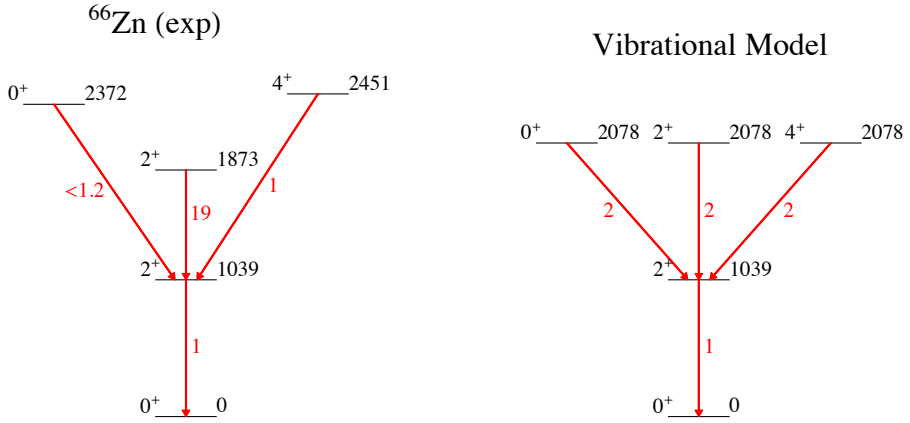

Figure 1.5: Comparison between the low-lying ^{66}Zn experimental decay scheme and the corresponding harmonic vibrational model prediction. The energy of the first 2^+ state has been fixed to the experimental value. In red are shown the predicted $E2$ transitions between the states and the corresponding $B(E2)$ values normalized to $B\left(E2; 2_1^+ \longrightarrow 0_1^+\right)$. The experimental data are taken from [37], more recent results are reported in the text.

twice the energy of the 2_1^+ state, in fair agreement with what expected for a vibrational nucleus. However, the vibrational description fails when further observables are considered, such as $B(E2)$ values. The ratio $B_{42} \equiv B\left(E2; 4_1^+ \longrightarrow 2_1^+\right) / B\left(E2; 2_1^+ \longrightarrow 0_1^+\right)$ is particularly sensitive to the specific collective characters of the nucleus [19]. For ^{66}Zn, this value is a factor of $2-2.5$ smaller than the vibrational model prediction $B_{42}^{vibr} = 2$ [35,36]. The value of the $B\left(E2; 2_2^+ \longrightarrow 2_1^+\right)$ reported in [37] is extraordinarily enhanced by a factor of 10 with respect to the vibrational model prediction. However, it has to be noted that such enhancement has not been observed in the other even zinc isotopes, and a more recent measurement [35] shows a better agreement with the vibrational model (in this case the ratio $B\left(E2; 2_2^+ \longrightarrow 2_1^+\right) / B\left(E2; 2_1^+ \longrightarrow 0_1^+\right)$ is about 2). Also the trend of the 0_2^+ state energy in the even Zn isotopes, as a function of the neutron number, cannot be reproduced by a simple vibrational scheme (see figure 1.6). A different interpretation, suggested for the ^{64}Zn isotope [34], groups the low-lying states in two different quasirotational[3] bands (with the exception of the 0_2^+ state that could be a core-excited configuration [38]). This interpretation reproduces also the enhancement of the $E2$ transition probabilities between the states in the ground band, and between the states in the excited band based on the 2_2^+ state, with respect to the ones of the inter-band transitions. However, the $B\left(E2; 2_2^+ \longrightarrow 2_1^+\right)$ value reported in [37] for ^{66}Zn cannot be reproduced

[3]The term "quasirotational" in this context refers to any spin sequence 0, 2, 4, 6, ... in which states are connected by strong $E2$ transitions, although in light nuclei such sequences can be understood within the framework of the shell model [39].

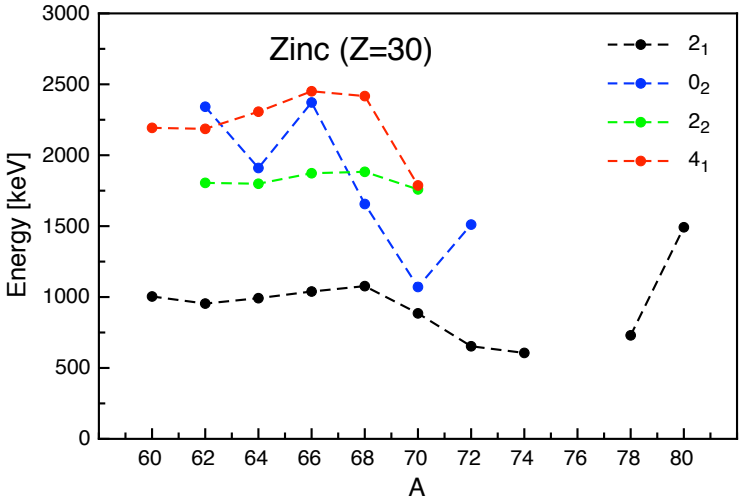

Figure 1.6: The energy levels of low-lying states for even Zn isotopes are reported as a function of the mass number. Data are taken from [37]. Only adopted values with definite spin and parity assignments have been considered.

in this interpretation. A γ-soft character[4] has been also proposed for the nearly stable zinc isotopes [35, 40]. Recent BMF calculations [41] predict that the collective character changes as a function of the neutron number, producing a shape evolution between a spherical shape to a γ-soft character, with ^{64}Zn as a turning point. The zinc isotopes are located in the transitional region between $N = 28$ and $N = 40$ magic numbers, in which the coexistence of different nuclear shapes is expected (see [42] for zinc isotopes and [43–46] for germanium and selenium isotopes). In [47, 48] it was also discussed the relevant role of the simultaneous treatment of quadrupole and octupole degrees of freedom in BMF calculations, as a consequence of shape coexistence. A particular focus on the case of ^{64}Zn was given in these works, where the predictions underestimate the value of the $B\,(E3)$ by two orders of magnitude.

As to the microscopical approach, many shell model calculations have been performed for zinc isotopes ([36,49–53] in the last two decades). The structure of nuclei in the $A \sim 60$ mass region was usually described considering only the negative-parity shell orbitals $1p_{3/2}$, $1f_{5/2}$, $2p_{1/2}$, outside a ^{56}Ni inert core $N = Z = 28$ (refer to figure 1.7). However, more recent calculations suggest that other orbitals must be included. The importance of core excitations in Ni isotopes has been pointed out, for instance, in Ref. [54] and explained by microscopic shell model calculations in Ref. [49], where it is shown how the contribution of the closed core configuration in the calculated ground state wave function of ^{56}Ni is

[4]The γ-soft nuclei are nuclei in which the Hill-Wheeler γ parameter, which describes the axial symmetry (see the previous section), has no definite value.

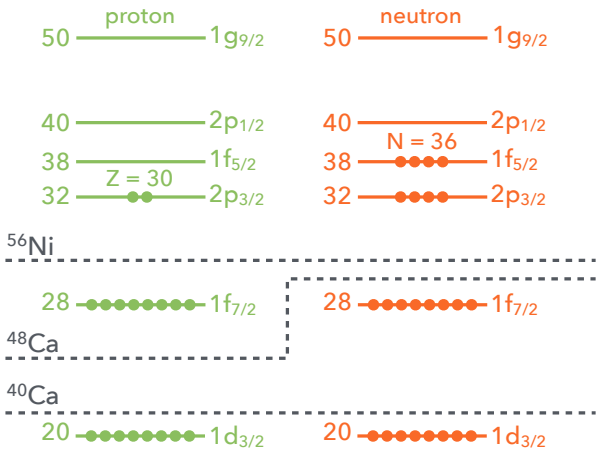

Figure 1.7: Single particle orbitals relevant for the Zn isotopes. The Fermi minimum configuration for ^{66}Zn, which is discussed in this thesis, is also shown, together with the three ^{40}Ca, ^{48}Ca, ^{56}Ni closed core configurations.

only $\sim$ 60% of the total (the contribution reaches $\sim$ 90% for the ^{48}Ca core, $Z = 20$, $N = 28$). The idea that ^{56}Ni can be considered an inert core in shell model calculations is thus debated, even though ^{56}Ni shows some of the typical features of a doubly magic nucleus (see figure 1.8). A g-factor measurement of the 2_1^+, 4_1^+ states of ^{62,64,66,68,70}Zn [50] suggests that a ^{48}Ca core could represent a better choice to describe the structure of the zinc isotopes without dramatically increasing the model space (and therefore the needed computational power). On the other side, the inclusion of the positive-parity neutron $1g_{9/2}$ has been proved to be important in many aspects. In odd zinc isotopes, the negative g-factor of low-lying $J = 9/2$ states can be explained considering the neutron $1g_{9/2}$ configuration as the dominant component in the nuclear wave function [37], while, in even zinc isotopes, the inclusion of neutron excitations in the $1g_{9/2}$ orbital could explain the decrease in energy of the 0_2^+ state [52, 55]. It was suggested in Ref. [51] that this orbital may be important also in the wave function of other states, such as the 4_1^+. The large population of the $1g_{9/2}$ neutron orbital seems also to be involved in the non-magicity of ^{70}Zn ($N = 40$) [55]. On the contrary, in its isotone ^{68}Ni [56], the harmonic oscillator magic number $N = 40$, typically ruled out by the spin-orbit term (figure 1.3), is restored.

Despite the fact that the zinc isotopic chain represents an ideal case to study all the above-mentioned aspects of nuclear structure, important experimental data are still missing, both for the stable and unstable isotopes, and where they are available many conflicting results are reported in the literature, preventing any stringent test of the theoretical models. Figure 1.9 shows the reported values of some of the observables important for the understanding of the low-lying structure of these nuclei. It is visible that all the $B\left(E2; 2_1^+ \longrightarrow 0_1^+\right)$ values agree within the error bars. The situation is different for

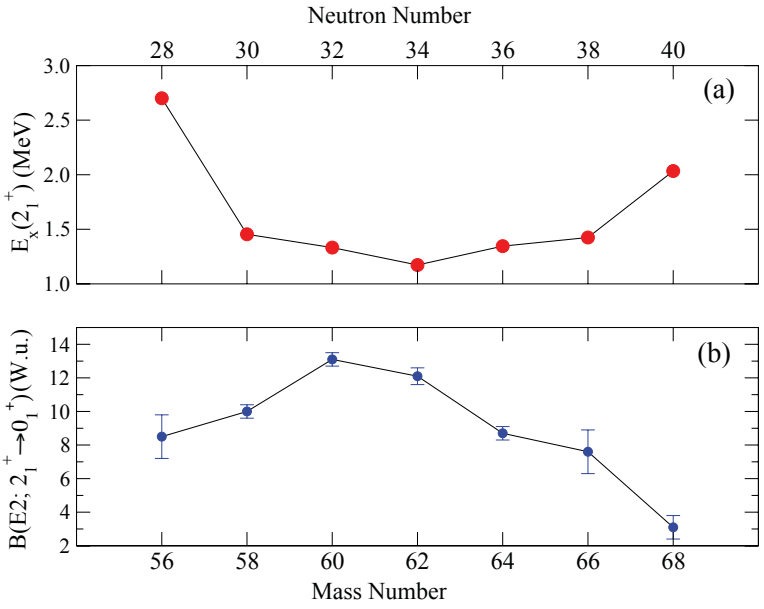

Figure 1.8: Experimental excitation energies of the 2_1^+ states (a) and $B\left(E2; 2_1^+ \longrightarrow 0_1^+\right)$ values (b) in even nickel isotopes reported as a function of the mass number. The typical parabolic trend of both the quantities is a signature of the magic character of ^{56}Ni and ^{68}Ni. Figure adapted from [57].

the $B\left(E2; 4_1^+ \longrightarrow 2_1^+\right)$ values, essential to evaluate the B_{42} parameter; conflicting results have been found using different techniques, such as Coulomb excitation measurements and lifetime measurements. A possible explanation could be an underestimation of the systematic errors during the analysis. The sources of systematic error in Coulomb excitation measurements will be extensively discussed in the following chapters. The feeding from unobserved states is a typical source of systematic error in lifetime measurements based on the Doppler effect [63]. This was discussed in details, for instance, in Ref. [62], to explain the conflicting $B\left(E2; 4_1^+ \longrightarrow 2_1^+\right)$ values measured in ^{74}Zn. Data relative to the $2_2^+ \longrightarrow 2_1^+$ and $0_2^+ \longrightarrow 2_1^+$ transitions are known only for few Zn isotopes. Quadrupole moments have been measured only in few cases, and only for the 2_1^+ states. Moreover, the results reported in Ref. [35] and Ref. [58] are in discrepancy with the adopted values reported in Ref. [37] not only in absolute value but also in the sign of Q_s, which, as already shown, is an indication of the quadrupole deformation of the nucleus.

More precise and reliable experimental results concerning the Zn isotopes are needed, as pointed out in several theoretical works (see for instance Ref. [49]). To this aim, a new campaign of Coulomb excitation measurements is ongoing at both the LNL (stable isotopes) and ISOLDE (neutron-rich isotopes) laboratories. The $^{74-80}$Zn isotopes were measured in 2016-2017 in the first HIE-ISOLDE measurement (the data analysis is in progress), while the Coulomb excitation of ^{62,64}Zn is the subject of two proposals submit-

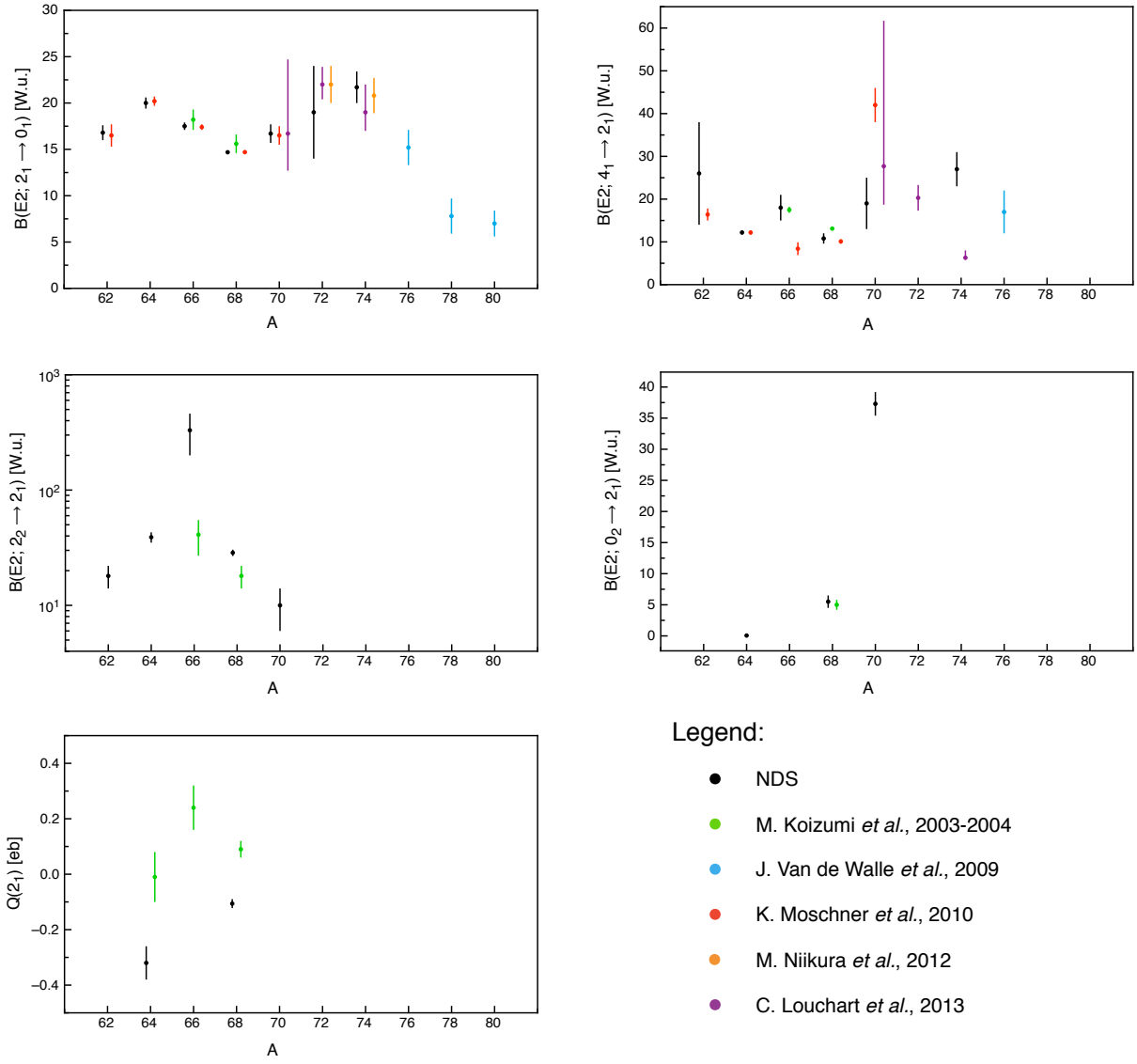

Figure 1.9: $B\,(E2)$ values of some of the transitions relevant for this work and $Q_s\left(2_1^+\right)$ value for the Zn isotopic chain are reported as a function of the mass. Different measurements corresponding to the same nucleus have been slightly mass-shifted in order to make comparison easier. The adopted values reported in [37] are shown in black. More recent measurements are reported with colors: green [35, 58, 59], blue [60], red [51], orange [61] and purple [62]. In order to simplify the comparison with the large adopted value in ^{66}Zn, the $B\left(E2; 2_2^+ \longrightarrow 2_1^+\right)$ values are reported in logarithmic scale. Only model-independent analyses have been considered.

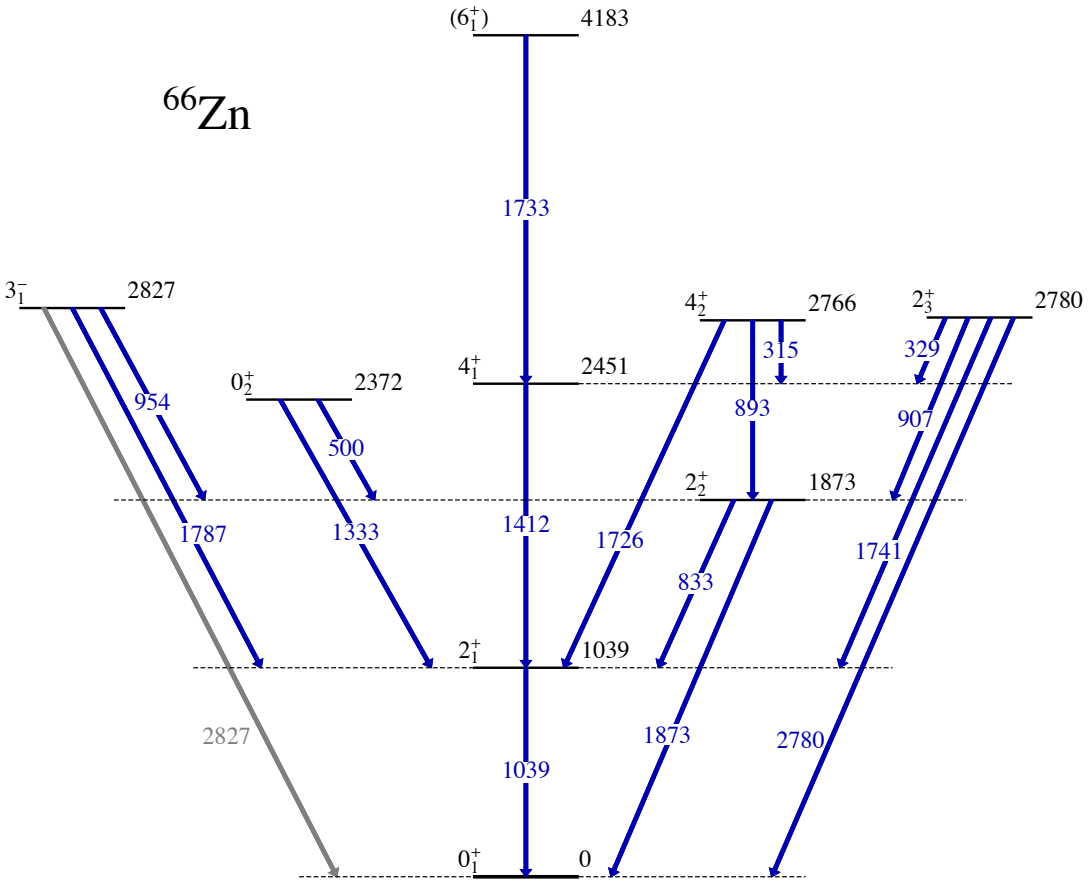

Figure 1.10: Low-energy decay pattern of ^{66}Zn of interest for the present work. Levels are shown in black, while transitions in blue (all the values are given in keV). Data taken from [37]. The transition $3_1^- \longrightarrow 0_1^+$ is reported in gray since it has never been directly observed. However, the $B\left(E3; 3_1^- \longrightarrow 0_1^+\right)$ was measured in an electron scattering measurement, as reported in [64].

ted at ISOLDE and LNL respectively. The Coulomb excitation of the ^{66}Zn isotope is the subject of the present thesis.

The part of the spectrum that is relevant to this experiment is shown in figure 1.10. The fact that the $B\left(E2; 2_1^+ \longrightarrow 0_1^+\right)$ and $Q_s\left(2_1^+\right)$ values are known with high precision in ^{66}Zn represents a stringent test for SPIDER. A new measurement of the $Q_s\left(2_1^+\right)$ could also help to solve the puzzle of its sign. The positive value found in ^{66}Zn indicates an oblate shape, which is not reproduced by any shell model calculation available in the literature but has been suggested for ^{74}Zn, combining results from Coulomb excitation [60] and lifetime [62] measurements. Also, new spectroscopic data could be investigated. The $B\left(E2; 4_1^+ \longrightarrow 2_1^+\right)$ value obtained by a Coulomb excitation measurement and the one obtained by a lifetime measurement disagree by a factor of two, preventing the use of the B_{42} to investigate the collectivity of ^{66}Zn. The very large value adopted for the

$B\left(E2; 2_2^+ \longrightarrow 2_1^+\right)$ [37] is rather uncommon for nuclei in this mass region. The more recent value obtained in [35] agrees better with the trend shown in figure 1.9. Due to the important role of the 0_2^+ state in the understanding of the contribution of the $1g_{9/2}$ orbital, the measurement of the $B\left(E2; 0_2^+ \longrightarrow 2_1^+\right)$ is of primary importance, also in order to confirm the trend shown in figure 1.9. Furthermore, using the Coulomb excitation technique, it is possible to obtain the deformation of the ground state, which is important to investigate the collective character of this nucleus and to test, in particular, BMF predictions.

CHAPTER 2

LOW-ENERGY COULOMB EXCITATION

Coulomb excitation is an inelastic scattering process in which two nuclei interact during the relative motion. In low-energy Coulomb excitation, the interaction occurs at an energy sufficiently below the Coulomb barrier so that the nuclear forces are excluded and only the electromagnetic field is involved. A model-independent analysis can be performed, to obtain diagonal and transitional matrix elements (including their relative signs).

The possibility of exciting atomic nuclei through the electromagnetic field generated by the interaction between colliding ions was realized already in the 1930s. In the first Coulomb excitation experiments, light ions were used as projectiles, so that the electromagnetic interaction was too weak to populate more than the first excited state [65]. Only after the theoretical description of deformed nuclei by A. Bohr and B. Mottelson [66] and the construction of accelerators for heavy ions in the 1950s, this process was experimentally confirmed [67, 68]. In the following years, experiments resulting in the excitation of different rotational bands up to spin $10 - 12\ \hbar$ were performed [69, 70]. The code developed by Winther and de Boer [71] was the first tool to analyse the data from the early Coulomb excitation measurements. Once the complexity of the acquired data had grown, data analysis started to require more sophisticated tools. The GOSIA code [5], developed in the 1980s in a collaboration between the University of Warsaw (Poland) and the University of Rochester (USA), is, until now, the most advanced tool for both data analysis and the reaction cross-section simulation for Coulomb excitation. The low-energy Coulomb excitation technique is a well-established experimental method used to study the electromagnetic properties of low-lying states in atomic nuclei, such as transition probabilities and quadrupole moments [72, 73]. These quantities are sensitive to the nuclear shape and represent the observables of the nuclear collective degrees of freedom. For this

reason the technique is widely used in experiments with stable and radioactive beams, in order to study shape-related phenomena (such as shape coexistence [74], superdeformation [75] and octupole shapes [76]) and to provide crucial information for the validation of modern theoretical models.

In this chapter, the theoretical description of the Coulomb excitation process will be briefly summarized (section 2.1), based on the detailed description that can be found in [77]. The quadrupole sum rule method [78], which allows to determine the collective shape parameters, will be introduced in section 2.2. The kinematics of the process will then be described (section 2.3), in relation to the Doppler effect that affects the energy of the de-exciting γ–ray energies, as measured in the reference frame of the laboratory system. The experimental considerations taken into account in Coulomb excitation experiments will be discussed in section 2.4 and lastly, in section 2.5, the GOSIA code will be introduced.

2.1 Theory of the Coulomb Excitation Process

Coulomb excitation is a scattering process that occurs between projectile and target nuclei, identified by their charge and mass numbers (Z_P, A_P and Z_T, A_T).

In order to ensure that the nuclear interactions can be neglected, the distance between the surfaces of the two colliding nuclei has to be sufficiently large. This hypothesis can be quantified introducing the impact parameter b, defined as a function of the scattering angle in the center of mass system (θ_{CM}) as follows:

$$b\left(\theta_{CM}\right) = a\left(1 + \frac{1}{\sin\frac{\theta_{CM}}{2}}\right) \tag{2.1}$$

where a is half the distance of closest approach in a head-on collision given by

$$a = 0.71999\left(1 + \frac{A_P}{A_T}\right)\frac{Z_P Z_T}{E_P} \quad \text{[fm]} \tag{2.2}$$

and E_P[MeV] is the kinetic energy of the beam in the laboratory frame. The nuclear interactions can be neglected, for a certain scattering angle θ_{CM}, if

$$b\left(\theta_{CM}\right) > R_P + R_T + \Delta \tag{2.3}$$

where R is the mean radius of the projectile (P) and target (T) nuclei and Δ is a parameter that has to take into account the surface diffuseness and the density distribution of the projectile and target nuclei, leading to the empirical value $\Delta = 5$ fm [78]. The criterion can be expressed in terms of beam energy (Cline's safe energy criterion): considering the nuclear radius $R = 1.25 \cdot A^{1/3}$ [fm], the so-called "safe energy" can be defined as the maximum bombarding energy for which $E_P\left(\theta_{CM}\right)$ respects the following inequality

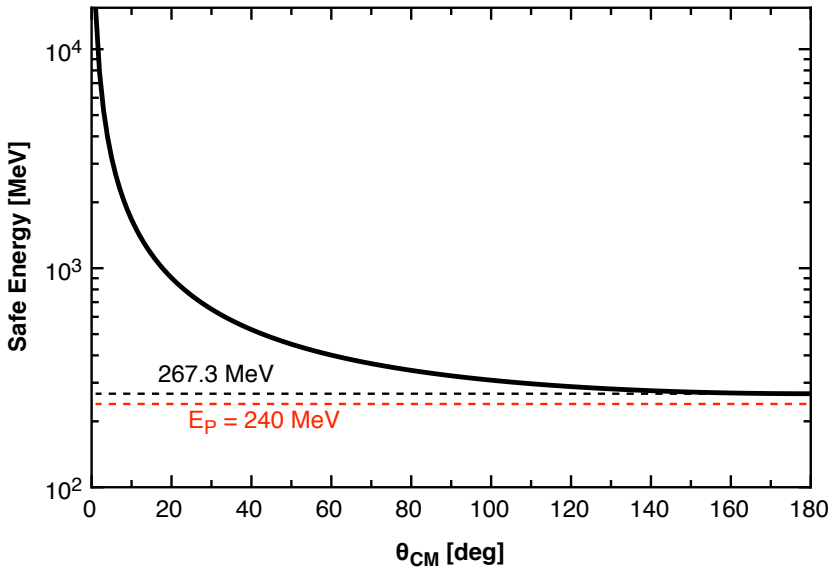

Figure 2.1: Safe energy, defined in equation 2.4 as a function of the scattering angle in the center-of-mass system. The plot refers to the ^{66}Zn experiment discussed in this thesis, where an enriched ^{208}Pb target was used. The chosen beam energy of 240 MeV is also shown.

$$E_P\left(\theta_{CM}\right) < 0.72 \cdot \frac{Z_P Z_T}{1.25\left(A_P^{1/3} + A_T^{1/3}\right) + 5} \cdot \frac{A_P + A_T}{A_T} \cdot \left(1 + \frac{1}{\sin\frac{\theta_{CM}}{2}}\right) \quad \text{[MeV]} \quad (2.4)$$

This inequality is usually satisfied for a beam energy of the order of $4 - 5$ MeV/A, and can be fulfilled by looking only to a partial angular range of θ_{CM}, using an appropriate experimental setup. Clearly, the minimum value of the safe energy is achieved in projectile backscattering at $\theta_{CM} = \pi$. In figure 2.1 the calculated safe energy for the Coulomb excitation of ^{66}Zn experiment discussed in the present thesis, as a function of the scattering angle, is presented. In order to ensure the condition 2.4, and also due to technical limitations related to the accelerator, a beam energy of 240 MeV was chosen in the experiment.

If the beam energy is maintained below the safe energy the process involves only the electromagnetic interaction. Since the theory of the electromagnetic interaction is well known, a full quantum mechanics treatment can be applied. In practice, however, due to the long range of the Coulomb interaction and to the complex structure of the level scheme of the nuclei involved in the scattering process, a semi-classical approach is applied, i.e. a classical treatment of the relative motion of the projectile and the target with a quantum treatment of the excitation process. This approach, originally introduced by K. Alder and A. Winther [79], is based on the fact that the interaction in the Coulomb excitation process is dominated by the Rutherford term $Z_P Z_T e^2/r$ (where e is the electron

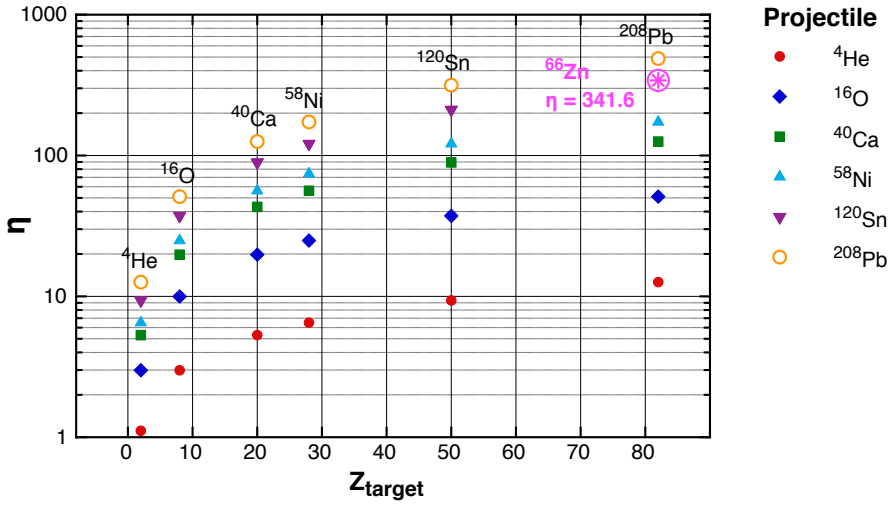

Figure 2.2: Sommerfeld parameter η calculated for different combinations of projectiles and target nuclei. The pink star marks the η parameter calculated for the Coulomb excitation of ^{66}Zn experiment.

charge and r the distance between the projectile and the target) and provides a significant simplification of the data analysis, without any loss of accuracy (see [77] for the errors associated with this treatment). Two conditions must be fulfilled in order to apply the semi-classical treatment. First, the wavelength λ associated to the projectile must be small compared to the typical length a of the process, i.e. $\lambda/2\pi \ll a$. This requirement can be expressed by means of the Sommerfeld parameter as follows:

$$\eta_i = \frac{2\pi a}{\lambda} = \frac{Z_P Z_T e^2}{4\pi\epsilon_0 \hbar v_i} \gg 1 \tag{2.5}$$

where v_i is the relative projectile velocity before the collision (corresponding to the initial projectile velocity in the laboratory system), $\hbar$ is the Plank's constant and ϵ_0 is the vacuum permittivity. Condition 2.5 is strictly related to the safe energy definition. The second requirement is that the excitation energy ΔE (which can be referred to both the projectile and/or the target) must be small compared with the kinetic energy E in the center-of-mass reference system:

$$\Delta E \ll E \tag{2.6}$$

The conditions 2.5 and 2.6 are well satisfied in Coulomb excitation experiments involving heavy ions (where $\eta_i \sim 50 - 100$, $E \sim 0.1 - 1$ [GeV], $\Delta E \sim 0.1 - 5$ [MeV]), but they are not when light nuclei are involved (where $\eta_i \sim 5$, $E \sim 50$ [MeV], $\Delta E \sim 5 - 10$ [MeV]). In the latter case, a full quantum analysis is required. Figure 2.2 presents the Sommerfeld parameter calculated for different combinations of projectile and target nuclei, considering a beam energy equal to the safe energy at $\theta_{CM} = 180°$. Considering the conditions of

the ^{66}Zn experiment, a value of $\eta = 341.6$ is obtained; the uncertainty introduced by the semi-classical treatment on the final results can be roughly evaluated as $\sim 1/\eta = 0.3\%$. The condition 2.6 is also well satisfied, as the beam energy of 240 MeV is much higher than the energy of the investigated excited states, which are below 3 MeV (see figure 1.10).

Following the semi-classical approximation, it is possible to classically describe the hyperbolic trajectories, resulting from the Rutherford scattering, and use quantum mechanics for the description of the excitation/de-excitation process writing

$$i\hbar\frac{\partial}{\partial t}\left|\Psi\left(t\right)\right\rangle = \left[H_0\left(P\right) + H_0\left(T\right) + W\left(P,T,\vec{r}\left(t\right)\right)\right]\left|\Psi\left(t\right)\right\rangle \tag{2.7}$$

where H_0 is the Hamiltonian of the free projectile (P) and target (T) nuclei and W is the time-dependent mutual electromagnetic interaction (the position vector of the origin of P with respect to the origin of T is denoted by $\vec{r}(t)$). The wave function of the system $\left|\Psi\left(t\right)\right\rangle$ can be written as the product of the intrinsic projectile and target eigenstates:

$$\left|\Psi\left(t\right)\right\rangle = \left|\psi_P\left(t\right)\right\rangle\left|\psi_T\left(t\right)\right\rangle \tag{2.8}$$

The electromagnetic interaction can be decomposed in multipole components:

$$W\left(P,T,\vec{r}\left(t\right)\right) = W_E\left(P,T,\vec{r}\left(t\right)\right) + W_M\left(P,T,\vec{r}\left(t\right)\right) + W_{EM}\left(P,T,\vec{r}\left(t\right)\right) \tag{2.9}$$

where W_E is the mutual electric multipole-multipole interaction, W_M is the mutual magnetic multipole-multipole interaction and W_{EM} is the interaction between the electric and the magnetic multipole moments caused by the relative motion of the two systems. The main term in equation 2.9 is the electric monopole-monopole interaction, corresponding to the Coulomb interaction $Z_P Z_T e^2/r$, which determines the relative motion of the two nuclei. The next most important terms are the ones describing the interaction between the monopole moment of the projectile (target) with the electric multipole moment of the target (projectile), which give rise to the target (projectile) excitation. Higher-order electric multipole-multipole excitation is usually less important, as well as the W_M and W_{EM} interactions, which contain a term $(v/c)^2$, typically small in low-energy Coulomb excitation ($\sim 0.1 - 0.25\%$). The most important terms of 2.9 can be approximated as

$$W_E\left(P,T,\vec{r}\left(t\right)\right) \sim V_E\left(P,\vec{r}\left(t\right)\right) + V_E\left(T,\vec{r}\left(t\right)\right) + \frac{Z_P Z_T e^2}{r} \tag{2.10}$$

where only electric monopole-monopole and monopole-multipole interactions are considered. Assuming that only the target is excited, the interaction can be written as follows:

$$V_E\left(T,\vec{r}\left(t\right)\right) = \sum_{\lambda\geq 1,\mu}\frac{4\pi Z_P e}{2\lambda+1}M_T\left(E\lambda,-\mu\right)\left(-1\right)^{\mu}\left[\vec{r}\left(t\right)\right]^{-\lambda-1}Y_{\lambda\mu}\left(\theta,\phi\right) \tag{2.11}$$

where M_T is the electric multipole moment [32], Y are the spherical harmonics and θ, ϕ are the polar and azimuthal angles of the projectile in the reference system where the target is fixed in the origin. The Schrödinger equation 2.7 becomes:

$$i\hbar\frac{\partial}{\partial t}\left|\psi_T\left(t\right)\right\rangle = \left[H_0\left(T\right) + V_E\left(T, \vec{r}\left(t\right)\right)\right]\left|\psi_T\left(t\right)\right\rangle \tag{2.12}$$

The excitation of the projectile nucleus corresponds merely to the interchange of the roles of target and projectile.

Considering the initial conditions $W = 0$ and that the nuclei are in their ground states when $t \to -\infty$, it is possible to solve the equation 2.12 and obtain $\left|\psi\left(+\infty\right)\right\rangle$[1]. The wave function can be expanded as

$$\left|\psi\left(t\right)\right\rangle = \sum_n a_n\left(t\right)\left|\varphi_n\right\rangle \tag{2.13}$$

where $\left|\varphi_n\right\rangle$ are the eigenstates of the free Hamiltonian H_0 and n indicates the possible final states:

$$H_0\left|\varphi_n\right\rangle = E_n\left|\varphi_n\right\rangle \tag{2.14}$$

By substituting equation 2.13 in equation 2.12 a set of coupled equations for the time-dependent excitation amplitudes $a_n\left(t\right)$ is obtained:

$$i\hbar\frac{da_k\left(t\right)}{dt} = \sum_n a_n\left(t\right)\left\langle\varphi_k\right|V\left(t\right)\left|\varphi_n\right\rangle \exp\frac{it}{\hbar}\left(E_k - E_n\right) \tag{2.15}$$

By solving the system of coupled equations 2.15, it is possible to determine the $a_n\left(t\right)$ coefficients, related to the excitation probability. In the case of a single-step excitation from the ground state to an excited state, described using the a_n amplitude, the excitation probability can be determined as follows ($a_n \equiv a_n\left(t \to +\infty\right)$):

$$P_n = \left|a_n\right|^2 \tag{2.16}$$

From 2.16 it is possible to deduce the Coulomb excitation cross-section:

$$\frac{d\sigma_{clx}}{d\Omega} = \frac{d\sigma_R}{d\Omega}\cdot P_n \tag{2.17}$$

where $d\sigma_R/d\Omega$ is the Rutherford cross-section. It should be noted that n specifies the level and the magnetic quantum number and therefore, to calculate the cross-section from 2.17, the sum and the average over all the magnetic substates has to be performed.

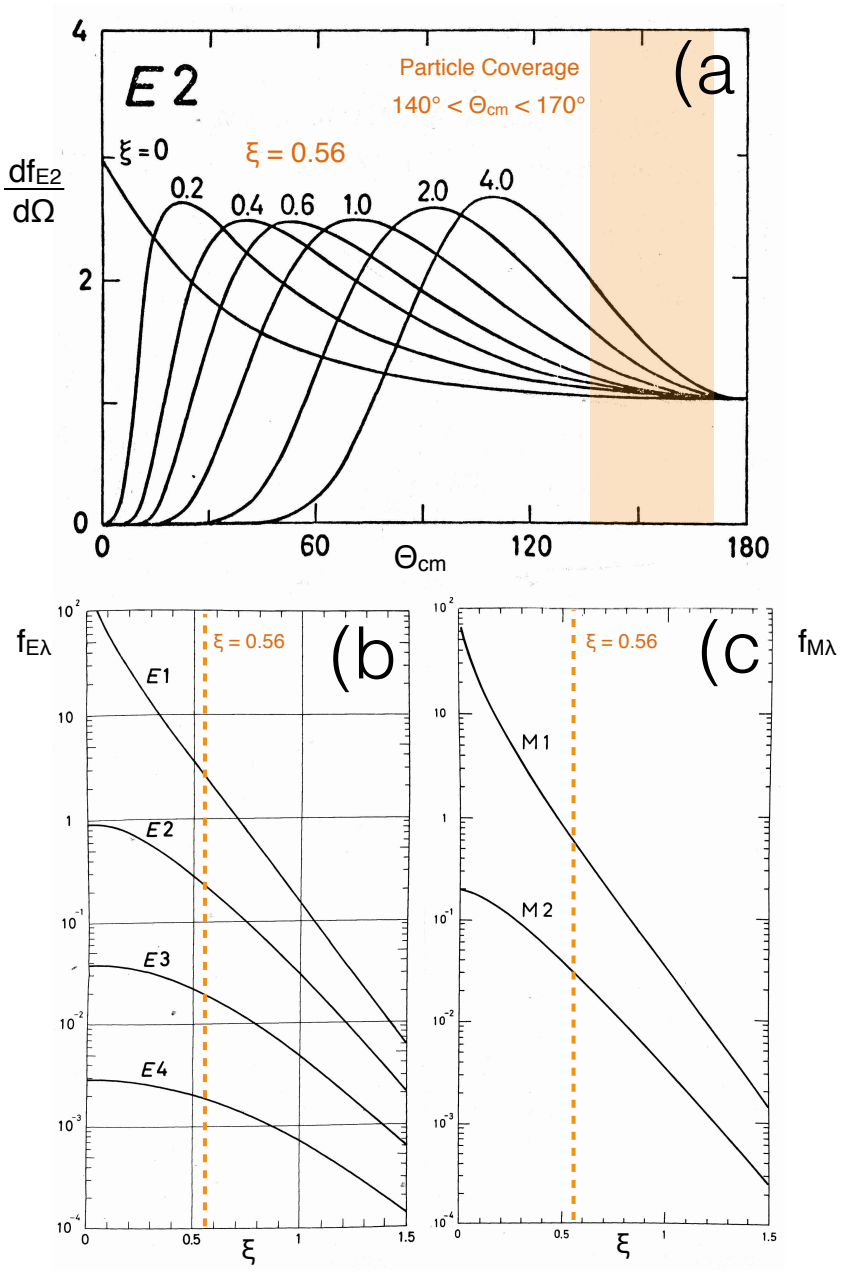

Figure 2.3: (a) The differential cross-section function $df_{E2}(\theta, \xi)$ is shown, as a function of the center-of-mass scattering angle, for different values of the adiabaticity parameter. The curves have been normalized to unity at $\theta_{CM} = 180°$. (b)-(c) The total cross-section functions $df_{E\lambda}$ and $df_{M\lambda}$ are shown with respect to the adiabaticity parameter and the multipolarity λ. The pictures have been adapted from [77]. The values related to the ^{66}Zn experiment are shown in orange.

2.1.1 First-Order Perturbation Theory

If the interaction between the projectile and the target nuclei is weak[2], the first-order perturbation theory can be applied to solve the system of coupled equations 2.15, obtaining the set of a_n coefficients that can be used to calculate the differential cross-section. Considering an electric transition of multipolarity λ and the target nucleus, the following dependency is obtained:

$$d\sigma_{E\lambda} = \left(\frac{Z_P e}{\hbar v_P^i}\right)^2 a^{-2\lambda+2} B\left(E\lambda, I_0 \longrightarrow I_f\right) df_{E\lambda}\left(\theta_{CM}, \xi\right) \tag{2.18}$$

(it is possible to obtain the magnetic excitation replacing $E \to M$, $v_P^i \to c$). The differential cross-section function $df_{E\lambda}(\theta, \xi)$ depends on θ_{CM} and on the so-called "adiabaticity parameter" ξ, which can be expressed as the difference between the final and initial Sommerfeld parameter:

$$\xi = \eta_f - \eta_i = \frac{Z_P Z_T e^2}{4\pi\epsilon_0 \hbar}\left(\frac{1}{v_f} - \frac{1}{v_i}\right) \tag{2.19}$$

where v_f is the relative velocity of the projectile-target system after the collision, which takes into account the excitation energy ΔE. In figure 2.3, the functions df are shown for different combinations of ξ, θ_{CM} and multipolarities. It can be noted that an increase of one unity in λ roughly corresponds to an order of magnitude decrease in the value of df. Moreover, for the same multipolarity λ, $df_{E\lambda}$ is higher than $df_{M\lambda}$ and it can be demonstrated that $d\sigma_{E2}$ is also generally higher than $d\sigma_{M1}$: considering the kinematics conditions of the ^{66}Zn experiment and an excitation from a 2^+ state to a higher lying 2^+ state, assuming a 1 W.u. excitation for both the $E2$ and $M1$ transitions, $d\sigma_{E2} \sim 300\, d\sigma_{M1}$.

2.1.2 Second-Order Perturbation Theory

The first-order perturbation theory provides a method to calculate the Coulomb excitation cross-section for processes involving the ground states of both the projectile and the target nuclei and their excited states. The dependence of this quantity from the reduced transition probability is expressed by equation 2.18. Using the second-order treatment it is possible to include the multi-step excitation and the reorientation effect. The excitation amplitude is written as:

$$a_n = a_n^{(1)} + a_n^{(2)} \tag{2.20}$$

[1]Since the effective collision time in Coulomb excitation is of the order of 1 zs, which is 10^8 times shorter than the typical lifetimes of the excited states ($\sim 1 - 10$ ps), it is possible to consider $|\psi(+\infty)\rangle$ as the wave function after the collision.

[2]This condition can be quantified requiring that the excitation probability connecting the involved excited states must be small compared to unity.

where the superscripts refers to first (1) and second (2) order.

To understand the importance of multi-step excitation it is useful to consider the population of the 0_2^+ and 4_1^+ states in an even-even nucleus, as in the case of ^{66}Zn (figure 1.10). $E0$ excitation is strictly forbidden, thus two-step excitation is the only way to populate the second 0^+ state, even if the de-excitation to the ground state via the emission of an internal conversion electron is allowed. The 4_1^+ state can be populated from the 0_1^+ state in two ways: directly, via an $E4$ excitation, or with an $E2$ two-step excitation through the 2_1^+ state. Figure 2.3 shows how the probability of exciting a given state through an $E4$ transition is much smaller than through the $E2$ excitation. It is clear that in this case, double-step excitations become the most important contribution, even though they can be considered second-order effects with respect to the one-step excitation process. In other cases, a single-step and double-step excitations may be competitive, for instance for a nucleus with a second, higher energy, 2^+ state. Such a state can be populated both by a direct $E2$ transition from the ground state, as well as by a two-step excitation through the 2_1^+ state. This case offers a typical example to explain how the sensitivity to the matrix element signs arises in Coulomb excitation. Considering, for instance, the transition $0_{g.s}^+ \longrightarrow 2_2^+$, the total excitation probability is written as follows:

$$P\left(0_{g.s}^+ \longrightarrow 2_2^+\right) = \left|a^{(1)}\left(0_{g.s}^+ \longrightarrow 2_2^+\right) + a^{(2)}\left(0_{g.s}^+ \longrightarrow 2_1^+ \longrightarrow 2_2^+\right)\right|^2 \tag{2.21}$$

This quantity (and therefore the cross-section) is composed by the matrix element associated to the single excitation ($\left\langle 2_2^+ \left|\left| E2 \right|\right| 0_{g.s}^+ \right\rangle^2$), by the one associated to the double excitation ($\left\langle 2_2^+ \left|\left| E2 \right|\right| 2_1^+ \right\rangle^2 \left\langle 2_1^+ \left|\left| E2 \right|\right| 0_{g.s}^+ \right\rangle^2$) and by the interference term

$$\left\langle 2_2^+ \left|\left| E2 \right|\right| 0_{g.s}^+ \right\rangle \left\langle 2_2^+ \left|\left| E2 \right|\right| 2_1^+ \right\rangle \left\langle 2_1^+ \left|\left| E2 \right|\right| 0_{g.s.}^+ \right\rangle \tag{2.22}$$

The sign of the interference term depends on the relative signs of the involved matrix elements. Multi-step excitation is more probable for larger values of θ_{CM}, due to the fact that in this case the nucleus experiences (on average) a stronger electromagnetic field during the scattering process.

The reorientation effect [80], another important second-order process, provides a tool to measure the static quadrupole moments of excited nuclear states. This effect can be explained as a double-step excitation in which the intermediate state is identical to the initial or to the final state, but the magnetic substate is different. First, an excited state is populated via Coulomb excitation from the ground state. Then, the nucleus continues to interact with the quadrupole moment of the excited state, thus producing a change in its orientation (i.e. a transition between magnetic substates). Considering the case of a 0^+ ground state and an excited 2^+ state, the total excitation probability can be written,

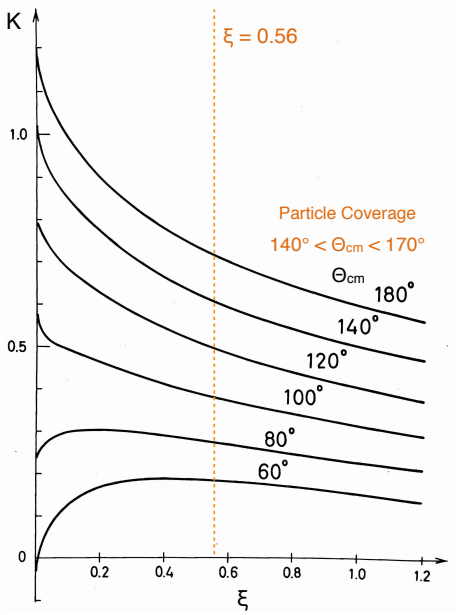

Figure 2.4: The quantity $K(\theta_{CM}, \xi)$ is reported as a function of ξ for different values of θ_{cm}. The picture has been adapted from [77]. The values related to the ^{66}Zn experiment are shown in orange.

including the reorientation effect, as

$$P\left(0^+_{g.s} \longrightarrow 2^+_1\right) = P^{(1)}\left(0^+_{g.s} \longrightarrow 2^+_1\right) \cdot \cdot \left[1 + \frac{4}{5}\sqrt{\frac{2\pi}{7}}\frac{A_P \Delta E}{Z_T\left(1 + A_P/A_t\right)} Q_s\left(2^+_1\right) K\left(\theta_{CM}, \xi\right)\right] \tag{2.23}$$

where ΔE is the excitation energy and the quantity $K(\theta_{CM}, \xi)$ is shown in figure 2.4. From this picture, it can be seen how the effect is enhanced for high θ_{CM} values.

2.2 Quadrupole Sum Rules

Electromagnetic multipole operators are spherical tensors and, thus, zero-coupled products of such operators can be formed that are rotationally invariant (i.e. identical in the intrinsic system of the nucleus as well as in the laboratory system, see section 1.2.1). Considering the electric quadrupole operator $E2$, it is possible to express the components of the electric moments along the principal axis system, in terms of two parameters Q

and δ:

$$E(2,0) = Q\cos\delta \tag{2.24}$$

$$E(2,1) = E(2,-1) = 0 \tag{2.25}$$

$$E(2,+2) = E(2,-2) = Q\sin\frac{\delta}{\sqrt{2}} \tag{2.26}$$

This description is general and the Q, δ parameters can be related to the Hill-Wheeler parameters β, γ respectively, defined in section 1.2.1. The zero-coupled products of $E2$ operators can be evaluated in the principal axis system:

$$\{E2\times E2\}^0 = \frac{1}{\sqrt{5}}Q^2 \tag{2.27}$$

$$\left\{[E2\times E2]^2\times E2\right\}^0 = -\frac{\sqrt{2}}{35}Q^3\cos 3\delta \tag{2.28}$$

$$\left\{[E2\times E2]^0[E2\times E2]^0\right\}^0 = \frac{1}{5}Q^4 \tag{2.29}$$

...

It is possible to express the expectation values of the $E2$ invariants, for a given state n in the laboratory system, using the experimental $E2$ matrix elements:

$$\langle Q^2\rangle = \frac{\sqrt{5}\,(-1)^{2I_n}}{\sqrt{2I_n+1}}\sum_m M_{nm}M_{mn}\begin{Bmatrix} 2 & 2 & 0\\ I_n & I_n & I_m\end{Bmatrix} \tag{2.30}$$

$$\langle Q^3\cos 3\delta\rangle = \mp\sqrt{\frac{35}{2}}\frac{1}{2I_n+1}\sum_{ml} M_{nl}M_{lm}M_{mn}\begin{Bmatrix} 2 & 2 & 2\\ I_n & I_m & I_l\end{Bmatrix} \tag{2.31}$$

...

where the abbreviation $M_{ab}\equiv\langle I_a\,||E2||\,I_b\rangle$ and the 6-j coefficients [81] are used. The sign in 2.31 is negative for integral spin systems and positive for half-integral spin systems.

The parameters Q, δ are estimated on the basis the $E2$ matrix elements using the equations 2.30 and 2.31. It is also possible to calculate the expectation value of higher order rotational invariants, as $\langle Q^4\rangle$, and define the so-called "softness" of the Q, δ parameters, i.e.

$$\sigma\left(Q^2\right) = \sqrt{\langle Q^4\rangle - \left(\langle Q^2\rangle\right)^2} \tag{2.32}$$

A similar definition applies to $\sigma\left(Q^3\cos 3\delta\right)$. The parameters Q, δ, and their "softness", define the quadrupole shape of a nuclear state and its softness character, in a completely model-independent way. The treatment can be extended also to other operators. Examples of applications of this techniques are provided in [70, 75].

The 6-j coefficients in equation 2.30, 2.31 define the set of matrix elements needed in order to perform the evaluation. In principle a complete set of matrix elements is necessary, since the unity operator is present in all the expectation values. The matrix elements

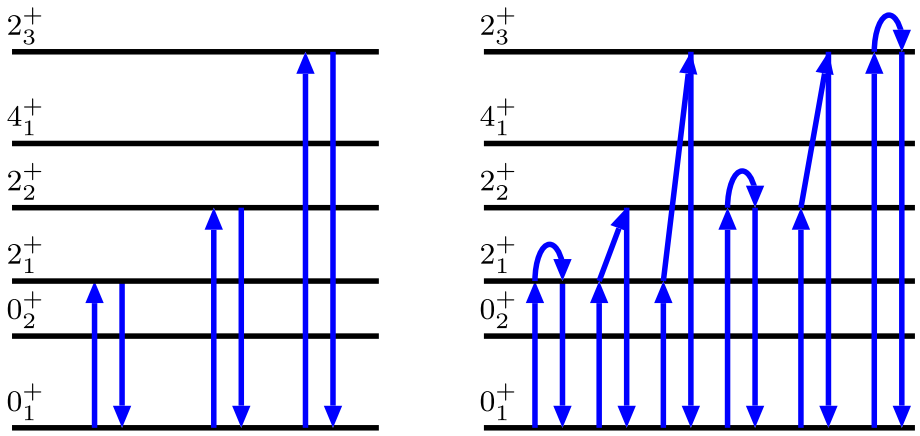

Figure 2.5: A schematic illustration of the $E2$ matrix elements necessary in order to evaluate Q (left) and δ (right) for a $0^+_{g.s.}$ state using the quadrupole sum rule method. Figure taken from [83].

involved in the evaluation of the Q and δ parameters for the ground state of an even-even nucleus are shown in figure 2.5. In most cases, the knowledge of the $\langle 2_1^+ ||E2|| 0^+_{g.s}\rangle$ matrix element is sufficient to obtain Q. For the evaluation of the δ parameter also the second-order $\langle 2_i^+ ||E2|| 2_1^+\rangle$ and $\langle 2_i^+ ||E2|| 2_i^+\rangle$ matrix elements are needed, where 2_i^+ are the higher lying 2^+ states of the nucleus. It can be seen also how the sign of the matrix elements is necessary evaluate the δ parameter. The error associated to approximations in the quadrupole sum rule method, used in real experiments, was studied for instance in [82].

2.3 Kinematics and Doppler Effect

The two-body kinematics of the Coulomb excitation process is shown in figure 2.6, considering the center-of-mass and the laboratory reference systems. Since the typical beam energies in Coulomb excitation experiments are of the order $4 - 5$ MeV/A (the Lorentz factor is $\gamma \sim 1.001$), and the mass of the involved nuclei are of the order $10 - 200$ GeV, it is possible, in a first approximation, to neglect relativistic effects. Considering a beam of E_P energy, the relative velocity before the collision v_i is given by

$$v_i = \sqrt{\frac{2E_P}{m_P}} \tag{2.33}$$

where m_P is the projectile mass and v_i is the projectile velocity in the laboratory system before the collision. In the center-of-mass system the velocity of the projectile u_P and the

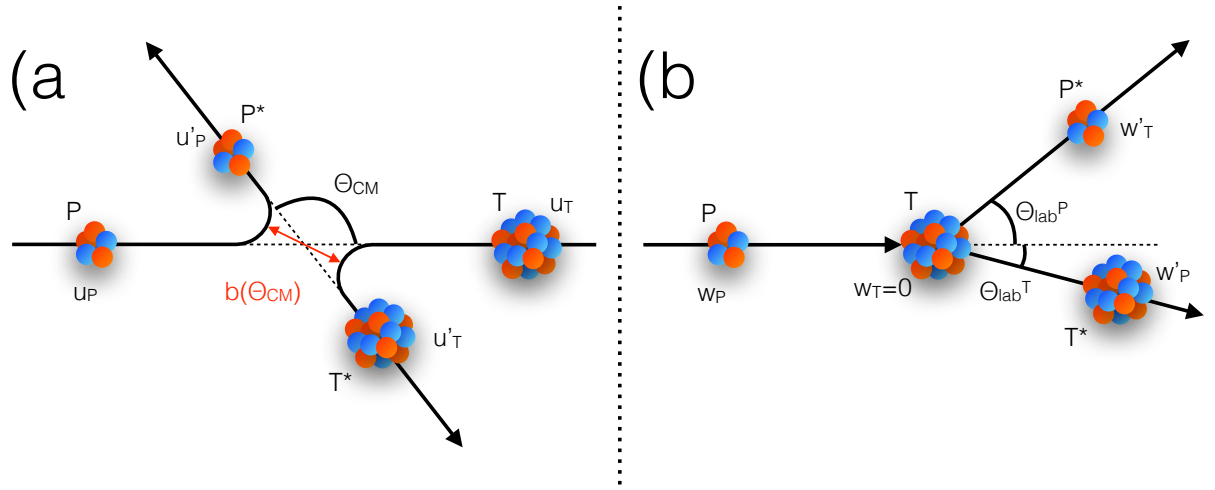

Figure 2.6: Coulomb excitation kinematics in the center-of-mass system (a) and in the laboratory system (b). The impact parameter defined in 2.1 is also shown.

target u_T can be expressed as follows:

$$u_P = v_i \frac{m_T}{m_P + m_T} \tag{2.34}$$

$$u_T = v_i \frac{m_P}{m_P + m_T} \tag{2.35}$$

where m_T is the target mass. Considering an excitation energy ΔE (which can be referred to both the projectile or to the target) the velocities in the center-of-mass system after the collision can be expressed as follows:

$$u'_P = \frac{m_T}{m_P + m_T} \sqrt{\frac{2}{m_P} \tilde{E}} \tag{2.36}$$

$$u'_T = \frac{m_P}{m_P + m_T} \sqrt{\frac{2}{m_P} \tilde{E}} \tag{2.37}$$

where

$$\tilde{E} = E_P - \Delta E \left(1 + \frac{m_P}{m_T}\right) \tag{2.38}$$

The scattering angles in the two reference system, defined in figure 2.6, are related by the expressions:

$$\frac{\sin\left(\theta^P_{CM} - \theta^P_{lab}\right)}{\sin\left(\theta^P_{lab}\right)} = \frac{m_P}{m_T} \sqrt{\frac{E_P}{\tilde{E}}} \equiv \tau \tag{2.39}$$

$$\frac{\sin\left(\theta^T_{CM} - \theta^T_{lab}\right)}{\sin\left(\theta^T_{lab}\right)} = \sqrt{\frac{E_P}{\tilde{E}}} \equiv \tilde{\tau} \tag{2.40}$$

where $\theta^P_{CM} = \theta_{CM}$ and $\theta^T_{CM} = \theta_{CM} + \pi$. Using equations 2.39, 2.40 it is possible to find the final velocities in the laboratory system:

$$w'_P = \frac{m_T}{m_P + m_T} \frac{\sin\theta^P_{CM}}{\sin\theta^P_{lab}} \sqrt{\frac{2\tilde{E}}{m_P}} \tag{2.41}$$

$$w'_T = \frac{m_P}{m_P + m_T} \frac{\sin\theta^T_{CM}}{\sin\theta^T_{lab}} \sqrt{\frac{2\tilde{E}}{m_P}} \tag{2.42}$$

The energy of the projectile and the target after the collision can be expressed as follows:

$$E'_P = \left(\frac{m_T}{m_P + m_T}\right)^2 \left(1 + \tau^2 + 2\tau\cos\theta^P_{CM}\right) \tilde{E} \tag{2.43}$$

$$E'_T = \frac{m_P m_T}{(m_P + m_T)^2} \left(1 + \tilde{\tau}^2 + 2\tilde{\tau}\cos\theta^T_{CM}\right) \tilde{E} \tag{2.44}$$

Equations 2.33-2.44 completely define the kinematics of the Coulomb excitation process. When the excitation energy ΔE is equal to zero, the equations describe the Rutherford scattering kinematics.

The typical lifetimes of the excited states studied in Coulomb excitation experiments are several orders of magnitude smaller than the typical flight-time of the scattered ions from the target position to the particle detector[3]. Since the typical velocities of the scattered ions are of the order of $v/c \sim 1 - 5\%$, the energy of the de-excitation γ–rays is affected by the Doppler effect, i.e. it is shifted to lower or higher energies, depending on the kinematics. This effect is described to the first order in β by the equation

$$E_{det} = \frac{E_0}{\gamma\left(1 - \beta\cos\vartheta\right)} \tag{2.45}$$

where E_{det} is the detected energy of the γ–ray in the laboratory system (affected by the Doppler shift), E_0 is the γ–ray energy in the reference system of the nucleus (not shifted), β is the velocity of the excited nucleus ($\beta = v/c$) and γ is the Lorentz factor. The angle ϑ is the angle between the direction of the emitted γ–ray and the direction of the de-exciting scattered nucleus. It can be expressed using spherical coordinates as

$$\cos\vartheta = \sin\left(\theta_p\right)\sin\left(\theta_\gamma\right)\cos\left(\phi_p - \phi_\gamma\right) + \cos\left(\theta_p\right)\cos\left(\theta_\gamma\right) \tag{2.46}$$

where the angles $(\theta_\gamma, \phi_\gamma)$, (θ_p, ϕ_p) refer to the directions of the emitted γ–ray and the corresponding scattered nucleus respectively, in the laboratory system. If the directions of both the γ–rays and the scattered particles are measured during the experiment, the equation 2.45 can be inverted and an event-by-event Doppler correction can be applied. The quality of this procedure depends on the degree of segmentation of both the γ–ray and particle detectors.

[3]Isomeric states can be populated indirectly. When this happens, the nucleus can decay far from the target or also inside the particle detector.

2.4 Experimental Considerations

In order to obtain a set of matrix elements in Coulomb excitation studies, it is useful to overdetermine the system of strongly-coupled equations 2.15, corresponding to the possible excitation channels. This can be achieved by collecting the data over a wide range of scattering angles or beam energies, as well as by using different projectile (target) nuclei if the target (projectile) structure is studied.

Different detection techniques are utilized in Coulomb excitation experiments: particle, γ–ray and γ-particle coincidence spectroscopy. Particle spectroscopy can be applied only to study a few excited states in light nuclei ($A \lesssim 20$). In order to study many excited states in Coulomb excitation with heavy-ion beams, γ–ray spectroscopy is necessary. However, without detecting the direction of the projectile or target nuclei, it is impossible to perform a Doppler correction, thus, measurements in which only γ–rays are detected have limited energy resolution. Moreover, since different scattering angle ranges are not selectable, only one value of the intensity for each γ–ray transition is measured, which is insufficient to overdetermine the problem. Furthermore, the integration of the cross-section over the entire range of the scattering angle and the recoil energy is not straightforward. For these reasons, high-resolution coincident γ-particle spectroscopy, with the use of arrays of γ–ray and particle detectors with large angular coverages and large segmentations, is nowadays the most viable experimental technique for Coulomb excitation studies with heavy ions (see figure 2.7).

The detection of γ-particle coincidences offers the possibility to perform precise event-by-event Doppler correction to improve the energy resolution and, thus, to provide the chance to study nuclei in experiments where many excited states are populated. The segmentation of the particle detector allows to obtain, simultaneously, different sets of data corresponding to different scattering angles (the so-called a "differential measurement"). This method, besides overdetermining the problem, allows to exploit the dependence of the cross section on the quadrupole moments of the excited states. Furthermore, in high statistics cases, γ-γ-particle coincidences can be analysed to select the transitions of interest in experiments with many excited states.

When the target nucleus is investigated, the experimental sensitivity is limited by its isotopic purity. In the case of stable beams, since the purity of the accelerated species is usually much higher, Coulomb excitation of the projectile lead to a better reliability of the experimental results. In these experiments a lead ^{208}Pb target is often used since, due to its double magic character, its excitation probability is usually negligible, resulting in a simplification of the data analysis. Moreover, the high Z of the target enhances the cross-section, providing more sensitivity to second-order effects.

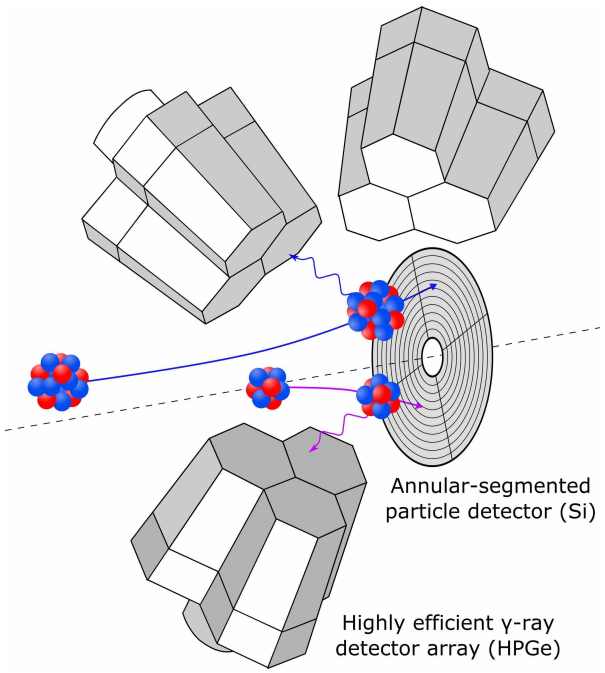

Figure 2.7: Typical experimental setup used in Coulomb excitation measurements when γ-particle coincidences are detected. Figure taken from [83].

To detect the recoil nuclei, parallel-plate avalanche, scintillators, or silicon detectors are commonly used. When detectors of the last type are chosen in experiments with stable beams, they are usually positioned at backward angles, in order to limit the radiation damage. In this conditions the mass of the projectile has to be smaller than the target's one, otherwise, both the target or projectile are scattered at forward angles. As mentioned above, multi-step excitation and reorientation effect are enhanced at backward angles, for this reason, if quadrupole moments and high-lying excited states are the focus of interest, the particle detection at backward angles is preferable. The detection of the scattered particles at forward angles is preferable, for instance, when the aim of the experiment is the measurement of the $B\,(E2)$ value of the transition from the first excited state to the ground state. In experiments with radioactive beams, the particle detection has to be performed at forward angles, to compensate for the low-intensity of the beams with a higher Rutherford cross section. Differential Coulomb excitation measurements in these cases are challenging but still possible, as demonstrated by the ISOLDE campaigns of measurements.

2.5 The GOSIA Code

The open source GOSIA code has been developed to plan and analyse Coulomb excitation experiments when single γ–rays or γ-particle coincidences are detected. It represents a powerful tool to determine the Coulomb excitation cross-section starting from a set of matrix elements (typically obtained from previous experiments or from models) or, vice versa, to extract the matrix elements from the measured γ–ray intensities. These are the direct observables in Coulomb excitation experiments and can be obtained for various transitions and in different kinematics conditions. The matrix elements are determined as strongly correlated parameters using a complex fit procedure in which the calculated γ–ray yields are compared to the experimental ones.

The GOSIA code exploits the semi-classical Coulomb excitation description discussed in section 2.1, in order to solve the system of coupled equation 2.15 and to calculate the excitation cross section. The code can also estimate the expected number of γ–rays or γ-particle coincidences. In the calculations, many effects are included, such as internal conversion de-excitation (competitive to the γ–ray decay), relativistic corrections, γ–ray angular distributions and the nuclear de-orientation in vacuum effect. The calculated cross sections are integrated over the scattering angle and the energy loss in the target (for this integration the stopping powers can be provided, for instance, by the SRIM code [84]). The geometry of the γ–ray detectors can be included, with their detection efficiency, as well as the particle detector geometry (examples are given in [72]). The intrinsic particle detector efficiency is assumed to be equal to one in the code, but many procedures have been developed and tested in order to take into account particle efficiencies lower than one [72].

Data sets corresponding to various projectile (or target) nuclei combinations and different beam energies or scattering angles can be simultaneously analysed by GOSIA, in order to overdetermine the problem and to gain sensitivity to second-order effects. In addition, known lifetimes of the excited states and experimental values of the branching and mixing ratios of decay transitions, obtained from complementary spectroscopic measurements, can also be used to further constrain the analysis.

A sophisticated χ^2 minimization procedure is implemented, which allows to extract the set of matrix elements from the experimental data, including error estimation. The additional available spectroscopic data are also included in the global χ^2 minimization procedure.

The exact calculation of the number of coincidences is complicated by the uncertainties related to the set-up geometry, to possible acquisition system dead-time and to the exact knowledge of the beam energy and intensity. For this reason absolute measurements

(comparison between experimental data and absolute cross section) are almost impossible. Different normalization procedures have been implemented and tested. One method is to normalize to the Rutherford cross section. This requires precise knowledge of the scattering angular range, of the efficiency of the particle detection system and of the acquisition system dead-time. Another method exploits the normalization to the known $B(E2)$ value of a transition of the nucleus that is studied. It is thus not necessary to know absolute values for detector efficiencies, beam intensity and target thickness. In these cases, the beam-target combination has to be chosen carefully, in order to avoid the energy overlapping of different transitions. This is the simplest normalization method when different states are excited in the same experiment, but the normalization transitions have to be observed with high statistics, and the relative γ efficiency has to be known with high precision. When it is possible, this is the preferred method, since everything is fitted by the code and there are no additional calculations required by the user. A third method, particularly used in Coulomb excitation experiments studying radioactive beams, exploits, together with GOSIA, the GOSIA2 code, with which the excitation probability of the projectile (target) can be normalized to that of the target (projectile) nucleus.

GOSIA is a complete analysis suite of codes that include, among other, a GUI (RACHEL), a quadrupole rotational-invariants fit code (SIGMA) and a code to fit the γ–ray detection efficiency data (GREMLIN). These last two codes have been used in the data analysis described in the following chapters. All the details regarding the code can be found in [85], including examples of input files for simulations and data analysis.

CHAPTER 3

EXPERIMENTAL SETUP

In this chapter, the low-energy Coulomb excitation setup used for the ^{66}Zn experiment (figure 3.1), performed at the INFN LNL, will be described. During this experiment, a ^{66}Zn beam with an energy of 240 MeV was provided by the LNL Tandem-XTU accelerator [10], impinging on a ^{208}Pb enriched target, also produced at LNL.

The γ–rays emitted by the de-exciting projectile and target nuclei were detected by the GALILEO array, described in section 3.1. The back-scattered projectiles were detected by the SPIDER array, described in section 3.2. In the same section the SPIDER

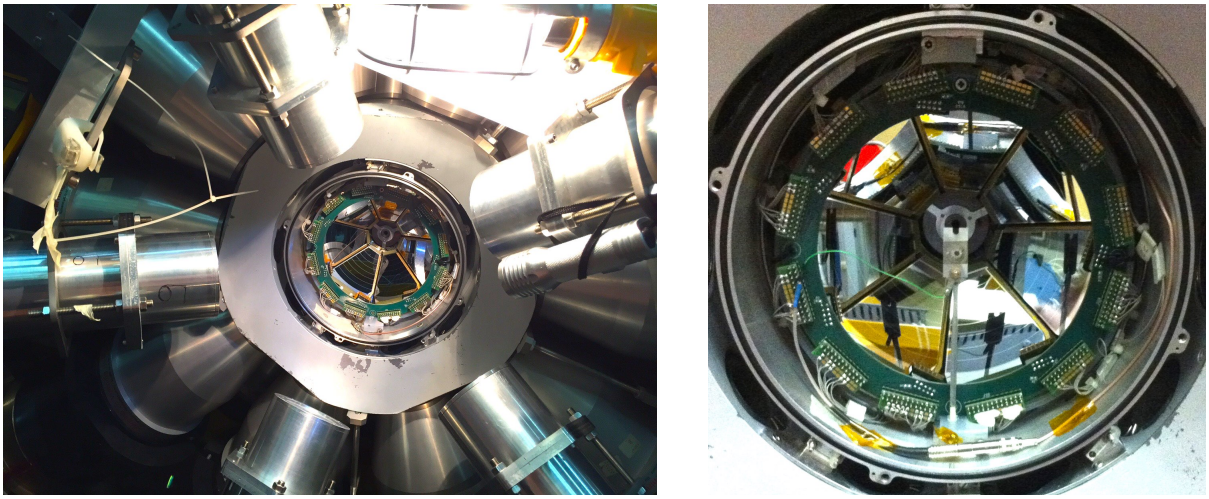

Figure 3.1: Left: the experimental setup used for the ^{66}Zn experiment composed of the GALILEO and SPIDER arrays. Five $LaBr_3$:Ce detectors are also present, not used in this experiment. Right: detail of the SPIDER array inside the reaction chamber of GALILEO.

commissioning experiment performed at the INFN LABEC[1] laboratory in Firenze, using a ^{7}Li beam impinging on a ^{27}Al target, will be also described. The fully digital acquisition system and the dedicated electronics, used for both the GALILEO and SPIDER arrays at LNL, is then described in section 3.3. The final data structure of the acquired events will be detailed in the last section.

3.1 The GALILEO Array

The GALILEO array has been developed at LNL as an advanced device for in-beam γ–ray spectroscopy experiments using the stable beams delivered by the Tandem-ALPI-PIAVE accelerator complex [10] and, in the near future, radioactive beams that will be provided by the SPES facility [1]. The final GALILEO array will become a 4π High Purity Germanium (HPGe) γ–ray spectrometer, composed of 30 GASP (GAmma–ray SPectrometer [86]) tapered detectors and 10 triple cluster detectors. In each cluster, three HPGe detectors will be mounted, sharing the same cryostat. The geometry of the array was designed to maximize the photo-peak efficiency under typical in-beam experimental conditions, achieving a value of $\sim 8\%$ at 1332.5 keV in the final configuration. The project is divided into two phases. In the first phase, currently operative, the GALILEO array consists of 25 GASP detectors, 15 positioned at backward angles and 10 perpendicular to the beam direction. These detectors can be coupled to large detectors, such as the Neutron Wall [87] or the Recoil Filter Detector [88] positioned in the forward direction. The former is designed to detect neutrons, thereby allowing, for instance, the selection of particular reaction channels in fusion-evaporation reactions. The latter one can be used to detect reaction recoils in order to study nuclei produced, for instance, in fission reactions. The first-phase GALILEO array has been coupled to a wide number of additional ancillary devices: light charged particle detectors (EUCLIDES [89] and TRACE [90]), $LaBr_3$:Ce detectors [91] for high energy γ–ray detection, a dedicated plunger device [92] for lifetime measurements and the heavy-ion detector SPIDER, which have been commissioned and used in experiments from 2015 onward. In the second phase, 5 additional GASP detectors (for a total of 30) and 10 triple cluster detectors will be added to complete the 4π γ–ray array, shown in figure 3.2.

Each GALILEO detector is enclosed in an anti-Compton shield composed by Bismuth Germanium Oxide (BGO) scintillators. These shields are needed since, in the usual energy range of the γ–rays detected in typical in-beam experiments ($\sim 0.1 - 2$ MeV), the probability of Compton scattering is larger than the one of photoelectric absorption, while

[1] LAboratorio di tecniche nucleari per i BEni Culturali (laboratory for nuclear techniques applied to cultural heritage).

Figure 3.2: View of the GALILEO array in the final configuration. The mechanical structure holding the HPGe detectors with their BGO shields is also shown. In this picture, the 10 triple cluster detectors are positioned at 90 degrees relative to the beam direction. Also some details of the automatic cooling system, used by the HPGe detectors, are visible.

the pair production is usually less important. When a γ–ray is Compton-scattered, usually only the energy of the recoil electron is released in the detector, resulting in a long tail of the detected energy distribution. The tail clearly deteriorates the peak-to-total ratio for the detection of other γ–rays present in the spectrum. Compton-suppression shields around the HPGe detectors are used, in order to reduce this background. The dimensions of the shields have to be kept as small as possible in order to maintain a high angular coverage by the HPGe array, thus avoiding a drastic reduction of the detection efficiency. For this reason, Compton shields are made of a high-Z material, with a high probability of γ–ray absorption. An ideal material for this purpose is the BGO, which has a high density (7.13 g/cm^3) and contains high-Z material (Bi Z=83). Using the amplitude and time properties of BGO shields, in conjunction with the ones of the HPGe detectors, it is possible to reduce the Compton background and thus enhance the peak-to-total ratio in the acquired γ–ray spectra.

In the ^{66}Zn experiment discussed in this thesis, the 25 GALILEO HPGe detectors were arranged in 4 rings: 5 detectors were placed at 152°, 5 at 129°, 5 at 119° and the last 10 detectors at 90° (all the angles are relative to the beam direction), as shown in figure 3.3.

At the center of the GALILEO array is positioned a vacuum chamber of 22 cm diameter that hosts the target and the ancillary detectors.

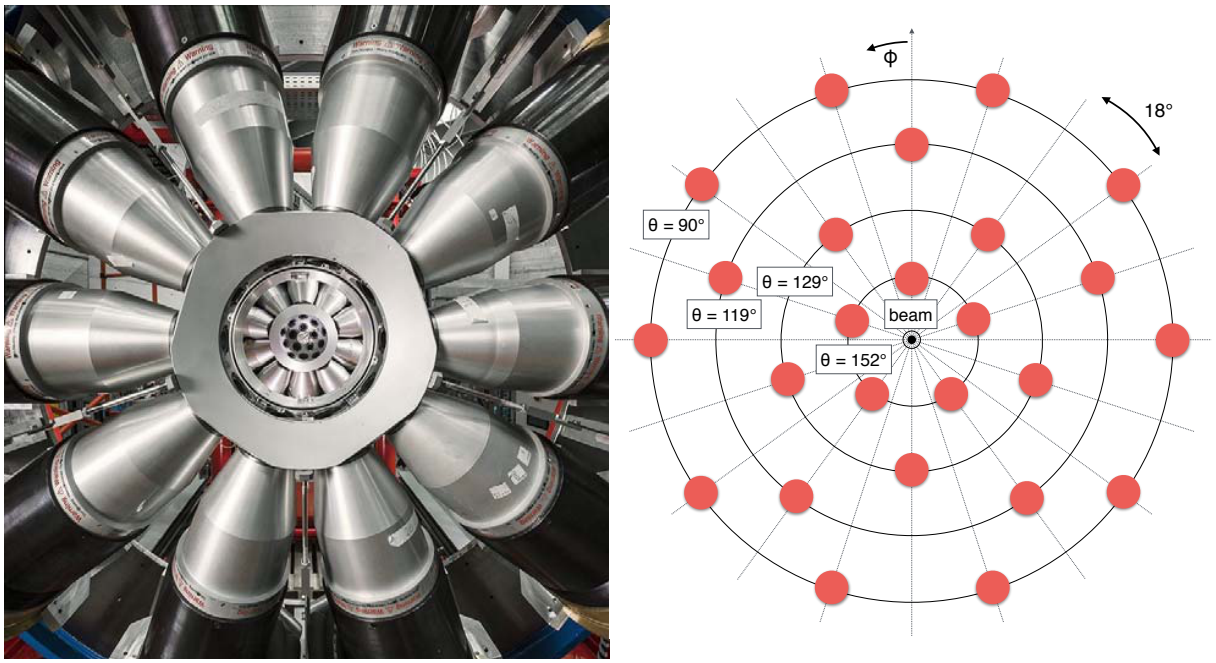

Figure 3.3: Left: the GALILEO array in the ^{66}Zn experiment configuration. Right: schematic view of the angular positions of the GALILEO HPGe detectors with respect to the beam direction.

3.2 The SPIDER Array

The SPIDER array is the ancillary device for low-energy Coulomb excitation measurements designed and implemented during this thesis. The original project is to use it in conjunction with modern γ–ray arrays, such as GALILEO and AGATA [3], to develop an experimental setup for Coulomb excitation measurements at LNL.

SPIDER consists of independent, trapezoidal-shaped, silicon detectors segmented on the front surface (junction side) into eight annular strips. Figure 3.4 shows the junction side of one of the SPIDER detectors. The back surface (ohmic side) is not segmented. Each detector covers one-eighth of 2π in the azimuthal angle; it is therefore possible to obtain a disk-shaped array using 8 detectors (see figure 3.5). The SPIDER strips are labelled starting from the bottom to the top from 0 to 7, as shown in figure 3.4. In the same figure it can be seen that strip 0 has a different shape with respect to the others, this because the inner section of a circular arc has been replaced by a segment in the cutting process of the silicon wafer. A guard ring is located all around the strips and, properly biased, minimizes the field distortion effects in the inter-strip regions, thus reducing cross-talk and charge splitting effects. Each silicon strip is 300 μm thick with dead layers of 50 nm on the junction side and 350 nm on the ohmic side. The bulk resistivity of the detector is of the order of 3400 Ωcm and the full depletion voltage is 100 V, with recommended bias of 120 V. The reverse current of each strip was below 1 nA before

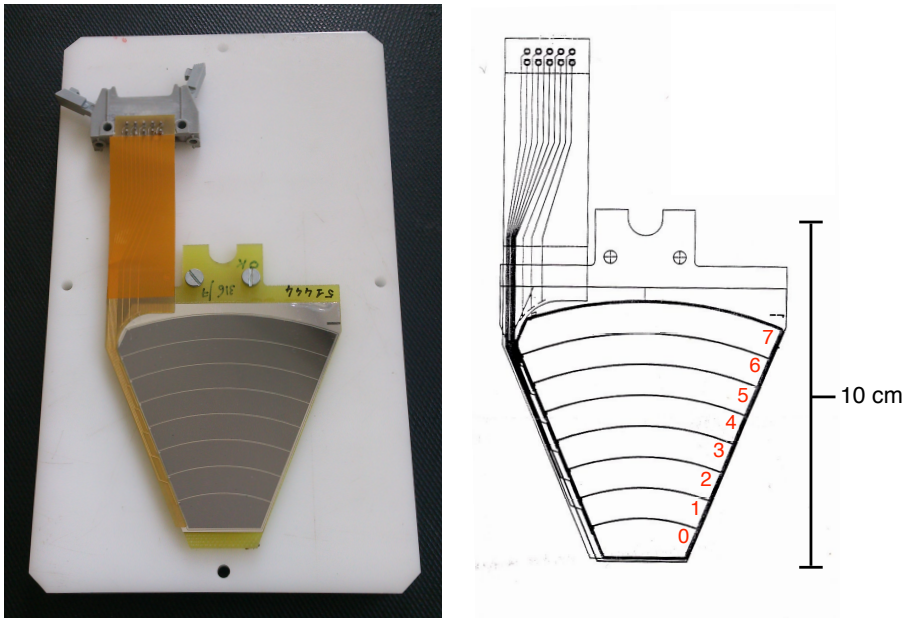

Figure 3.4: Picture (left) and schematic view (right) of one of the SPIDER detector from the junction side. The 8 strips and the guard ring are visible. In the schematic view, the labelling of the SPIDER strips that is used in this thesis is shown.

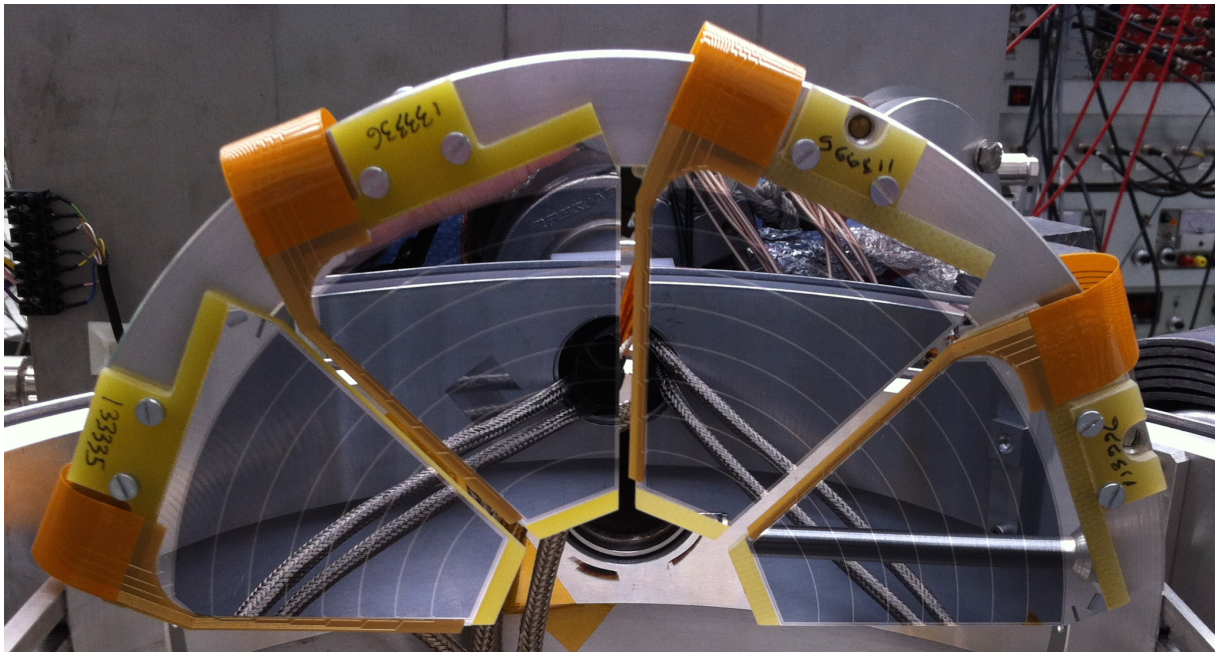

Figure 3.5: Half SPIDER array mounted in the disk configuration.

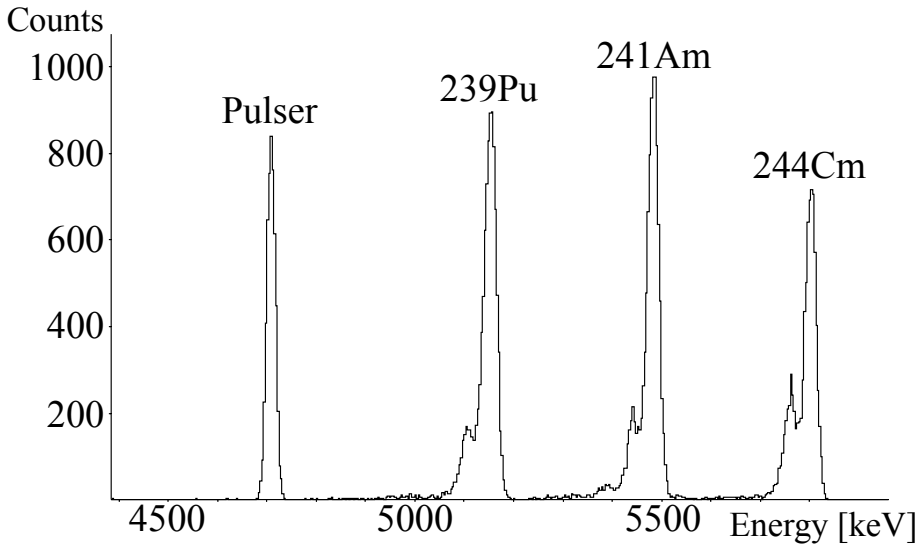

Figure 3.6: Alpha spectrum relative to strip 0, obtained using a triple alpha source (^{239}Pu + ^{241}Am + ^{244}Cm). The spectrum has been obtained in optimal conditions, in a dedicated test station.

the irradiation (factory conditions). Biasing of the detectors can be performed either independently for each strip or simultaneously for the whole detector. When coupled to GALILEO, the former method is used in order to have the possibility to power off dead or malfunctioning strips. The capacitance C of each strip was measured by applying the same 120 V bias voltage to the whole detector, resulting in $C \sim 100$ pF. Since the surfaces of the strips are different, this value slightly increases going from strip 0 to strip 7. The capacitance is crucial information in order to choose the SPIDER preamplifiers.

The energy resolution for each SPIDER strip was measured in a dedicated test station, using a triple alpha source ^{239}Pu+^{241}Am+^{244}Cm. A Full Width at Half Maximum (FWHM) of ~ 25 keV for alpha particle of ~ 5.5 MeV energy was obtained, corresponding to a resolution of $\sim 0.5\%$. As expected, the FWHM increases from strip 0 to strip 7 following the trend of the capacitance values. Using a pulser, it is possible to subtract the electronic contribution to the measured resolution: a value of $\sim 0.3\%$ is achieved in this way for the intrinsic resolution. A typical spectrum showing the α particles and pulser peaks is reported in figure 3.6. The energy resolution of the strips, when SPIDER is coupled with GALILEO, is worse: measured with a triple alpha source ^{239}Pu+^{241}Am+^{244}Cm, it is $\sim 1-2\%$. This is due to electronic noise introduced by the several electronic modules and to mechanical vibrations coming from the vacuum system at LNL.

Since the SPIDER array is composed of independent detectors, it is possible to arrange it into different configurations. This offers the possibility to adapt it to scattering chambers of different dimensions. In order to couple the SPIDER array with the GALILEO

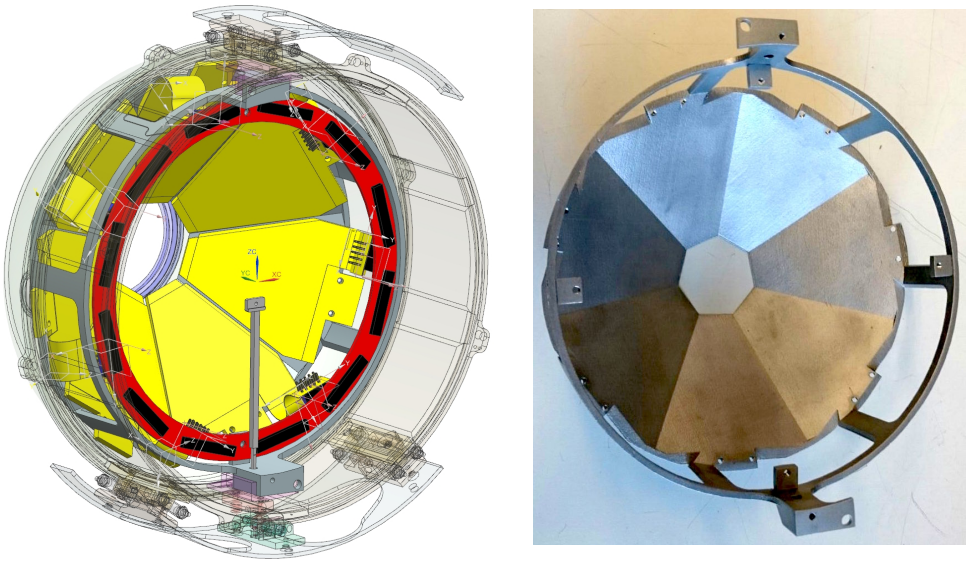

Figure 3.7: Left: the SPIDER array in the cone configuration inside the GALILEO vacuum chamber (the target holder is also visible). Right: 3D-printed aluminium holder used to arrange SPIDER inside the GALILEO vacuum chamber.

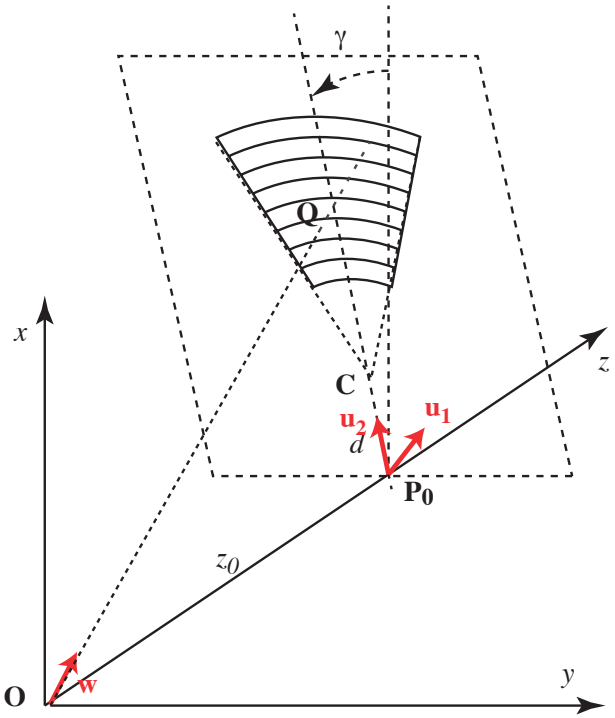

Figure 3.8: Geometrical description of one SPIDER detector in the cone configuration. The z-axis is opposite to the beam direction and **O** is the target position.

Strip	Theta Middle [deg]	Polar Coverage [deg]	Solid Angle [srad]
7	125.5	4.32	0.0505
6	129.9	4.53	0.0494
5	134.6	4.70	0.0471
4	139.3	4.81	0.0436
3	144.2	4.86	0.0389
2	149.0	4.83	0.0333
1	153.8	4.74	0.0271
0	158.5	5.59	0.0208

Table 3.1: In column 2 the angle between the z-axis and the $\mathbf{Q} - \mathbf{O}$ vector, where $\mathbf{Q}$ is the position in the middle of each strip, is shown (refer to figure 3.8). This value can be considered as the center-of-mass of the strips with good approximation. In column 3 and 4 are shown the polar and solid angular coverage of each strip.

vacuum chamber (22 cm diameter) a cone-like configuration of 7 detectors was implemented (see figure 3.7, left panel). An aluminium 3D-printed frame, shown in figure 3.7 right panel, was designed for this purpose. Since at the moment only stable beams are available at LNL, the array has been positioned at backward angles, a preferable configuration in these conditions as discussed in section 2.4. The geometry of this configuration is shown in figure 3.8. The distance between the vertex of the cone and the target position (z_0 in figure 3.8) is equal to 8.5 cm; each SPIDER detector covers a polar angle range of 37.4°, an azimuthal angle range of $2\pi/7 = 51.4°$ and the solid angle subtended by the entire array is equal to 17.3% of 4π. The polar and solid angles covered by each strip in the cone configuration are shown in table 3.1.

3.2.1 Study of the Doppler Correction Capabilities

The information about the angle between the de-exciting ion and the emitted γ–ray is needed in order to perform the Doppler correction of the γ–ray energy. A higher segmentation of the particle detector correspond to a higher precision in the determination of the kinematics, resulting in a superior Doppler correction. On the other hand, at a fixed distance of the particle detector from the target, a reduction in the number of sectors in a closed-cone configuration increases the angular coverage, improving the absolute efficiency of the particle detection and also the sensitivity to Coulomb excitation second-order effects. The use of seven sectors in the GALILEO chamber represents a good compromise between the two necessities. The polar angle segmentation of the SPIDER array is comparable with that of other particle detectors (e.g. double-sided silicon strip detectors [93] or

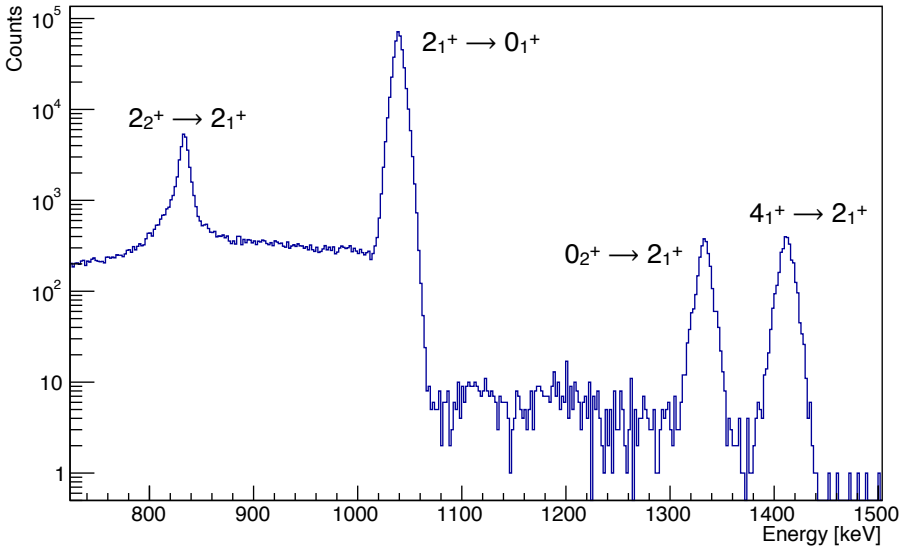

Figure 3.9: Simulated γ–ray spectrum for the Coulomb excitation of the ^{66}Zn experiment discussed in the present thesis.

parallel plate avalanche counters [94]) typically used in Coulomb excitation experiments, whereas the azimuthal angle segmentation is only equal to 2π divided by the number of used sectors.

In order to study the Doppler correction capabilities of the GALILEO and SPIDER setup, the geometry of both arrays has been implemented in the GEANT4 software [6]. The ^{66}Zn experiment has been simulated by introducing the GOSIA estimated γ–ray intensities into the GEANT4 code. The simulated γ–ray energy spectrum is shown in figure 3.9. In this spectrum, a coincidence between the γ–rays and the backscattered ^{66}Zn ions was required, and a Doppler correction procedure was applied considering the setup geometry and segmentation. The most intense transitions are clearly visible: $2_1^+ \longrightarrow 0_1^+$, $2_2^+ \longrightarrow 2_1^+$, $4_1^+ \longrightarrow 2_1^+$ and $0_2^+ \longrightarrow 2_1^+$. The simulated FWHM resolution of the $2_1^+ \longrightarrow 0_1^+$ transition, after the Doppler correction, is 11.8 keV.

The change of the detectors geometry in the GEANT4 software is not straightforward. For this reason, a dedicated Monte Carlo code has been developed during this thesis, in order to study the segmentation dependencies of the SPIDER array. In this code, the geometry of both the GALILEO and SPIDER arrays is analytically described and it is possible to change both the polar and the azimuthal angle segmentation of SPIDER. Different SPIDER configurations (as the disk or the cone-like) can be described, as well as HPGe arrays other than GALILEO (such as Mini Ball [95] and AGATA). It is possible to select the γ–ray energy and also the HPGe energy resolution. The effect of the energy loss in the target is taken into account as an average reduction of the backscattered ion

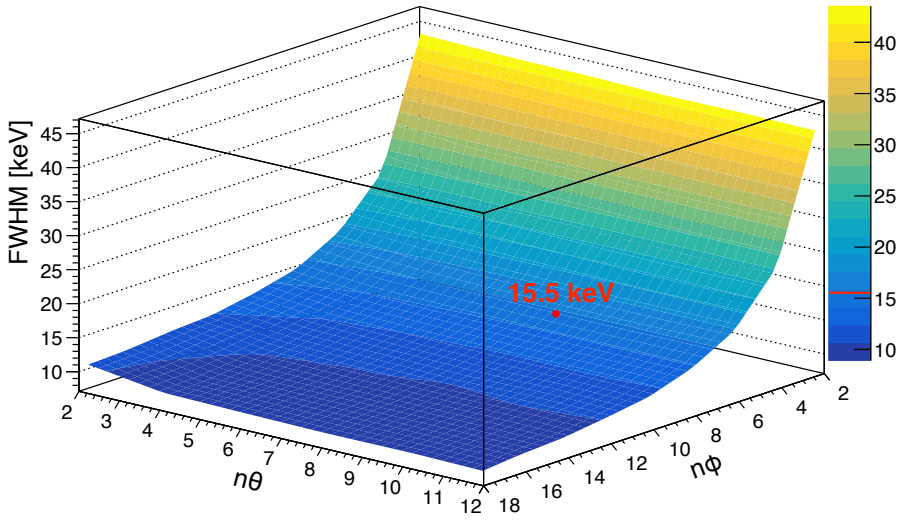

Figure 3.10: Simulated γ–ray FWHM as a function of the polar (nθ) and azimuthal (nϕ) segmentation in typical experimental conditions for Coulomb excitation experiments using stable beams (see the text for the details). In red is shown the value of the FWHM for the SPIDER configuration used in the ^{66}Zn experiment.

energies, while the effect of a non-uniform angular distribution for both the γ–rays and the scattered ions is neglected. The results obtained with this code were compared with the GEANT4 ones, proving the good agreement between the two simulations. In the case of the ^{66}Zn experiment the simulated FWHM for the $2_1^+ \longrightarrow 0_1^+$ transition, after the Doppler correction, is indeed 11.8 keV, the same value obtained from the GEANT4 simulation.

The FWHM simulated with the dedicated code is plotted as a function of the polar and azimuthal SPIDER angular segmentation in figure 3.10, considering γ–rays produced in a typical Coulomb excitation experiments with stable beams. In particular, the simulation considers 1332 keV γ–rays emitted in-flight by ^{60}Ni nuclei, which are scattered on a 1 mg/cm^2 ^{208}Pb target and detected at backward angles (with $\beta \sim 5\%$). The segmentation of the polar and azimuthal SPIDER angles nθ and nϕ refers to the number of considered strips and to the number of detectors, respectively. The disk configuration of SPIDER is assumed, since the cone-like configuration only slightly modifies the polar angle segmentation and does not change the azimuthal angle segmentation. The array is positioned at 8.5 cm from the target. The HPGe detectors of the phase 1 GALILEO array are considered, having a nominal intrinsic resolution of 2.1 keV. From figure 3.10 it is visible how the azimuthal segmentation of the SPIDER array is the most critical contribution to the γ–ray FWHM, which increase from $\sim$ 10 keV up to $\sim$ 45 keV going from 18 to 2 used detectors. The SPIDER polar segmentation is not crucial: already with

a segmentation of 6 used strips an asymptotic limit of $\sim$ 10 keV is reached. Doubling the segmentation in the azimuthal angle (from 7 detectors to 14) produces an improvement of 35% in the resolution, reaching a value close to the asymptotic limit. This limit is produced by other contributions, such as the energy loss in the target and the finite precision in the determination of the direction of the γ–rays when unsegmented tapered detectors are considered. For most Coulomb excitation measurements with SPIDER at backward angles and phase 1 GALILEO, an improvement of 35% is not crucial, thus a finer segmentation is, at present, unnecessary.

3.2.2 SPIDER Commissioning at LABEC

Before the installation at LNL, the SPIDER array has been commissioned at the INFN LABEC laboratory in Firenze, by measuring the Coulomb excitation of ^{7}Li. A beam of ^{7}Li impinging on a ^{27}Al target (0.5 mg/cm^2) was used in order to check the Doppler correction capabilities of the device and the radiation damage induced during the irradiation.

The calculated safe energy at 180° in this case is 6.35 MeV, a value close to the maximum energy provided by the LABEC accelerator for a ^{7}Li beam, 6 MeV, which was used during the experiment. The ratio between the mass of the projectile and the mass of the target is comparable to the one of the ^{66}Zn experiment, therefore similar kinematic conditions were achieved. Since this was the first in-beam irradiation of SPIDER, a minimum radiation damage effect was desired, which was ensured by the low charge of

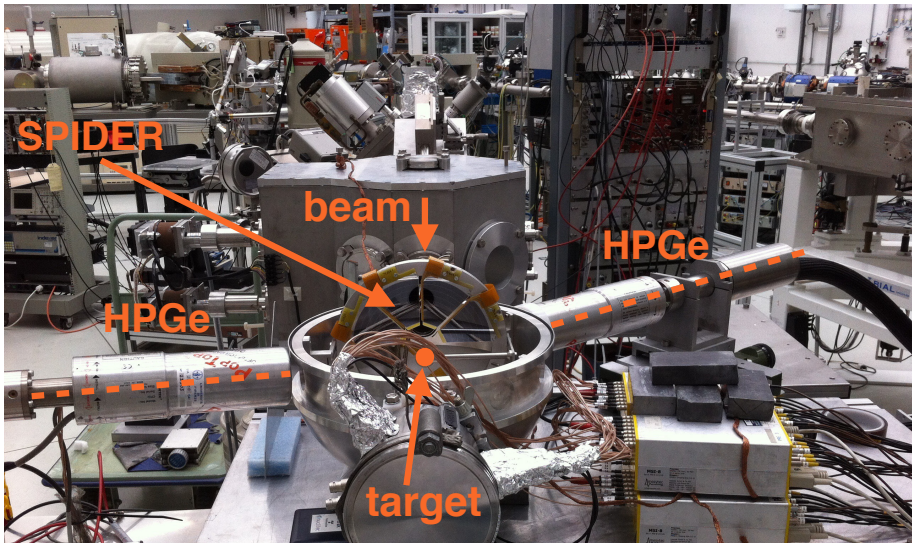

Figure 3.11: Experimental setup used for the SPIDER commissioning at the INFN LABEC laboratory. Two HPGe detectors and 4 SPIDER detectors, positioned at backward angles, where used in this test.

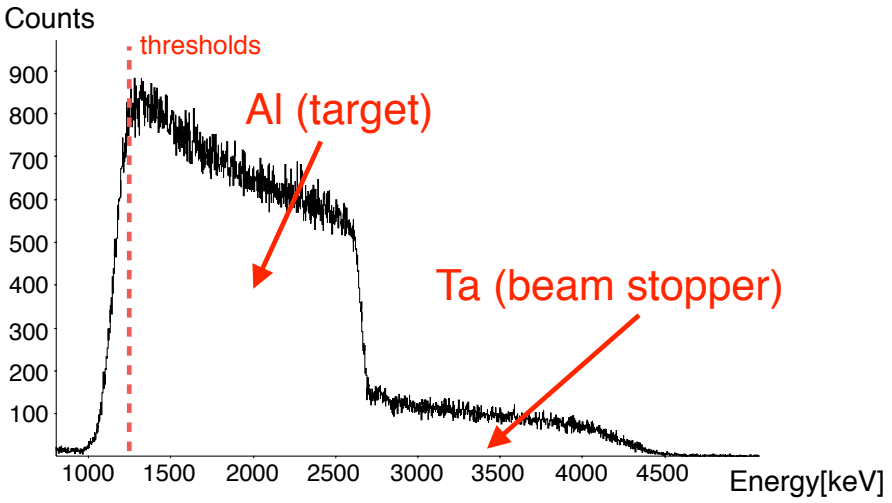

Figure 3.12: Particle energy spectra corresponding to a SPIDER strip positioned around $\theta = 120°$. The backscattered ^{7}Li ions impinging on the ^{27}Al target and on the tantalum beam dump positioned at ~ 10 cm from the target are indicated.

the projectile ($Z = 3$).

The setup used for this experiment is shown in figure 3.11. Two HPGe detectors were used, and 4 SPIDER detectors were positioned at backward angles in a half-disk configuration. The distance between the target and the detectors was 5 cm, resulting in a polar angular coverage of 28.1° and a solid angle range subtended by the entire array equal to 16.4% of 4π. An analog acquisition system, based on commercial modules, was implemented. In this experiment, it was possible to detect γ–rays using the two HPGe detectors, in coincidence with each SPIDER strip. An id-number for the germanium detectors and the SPIDER strips was also stored, thus giving the possibility to obtain the γ–ray and particle directions and to perform a Doppler correction. The energy spectra of 6 strips were also acquired, in order to monitor the interaction of the beam with the materials inside the vacuum chamber. An example of these spectra is shown in figure 3.12.

Data were collected during 31 h, at a mean beam current of 1.2 pnA. In figure 3.13 a portion of the total γ–ray spectrum acquired by two HPGe detectors, in coincidence with the entire SPIDER array, is shown. The broad peak at ~ 478 keV corresponds to the excitation of the first $1/2^{-}$ state in ^{7}Li, while the two peaks at 352 keV and 511 keV are due to the natural background. These two γ–ray peaks are visible since the rate for the real Coulomb excitation coincidences is comparable to the random coincidence rate, due to the low Z of both the projectile and target nuclei. In figure 3.13 it is also shown the same spectrum after applying the Doppler correction procedure, considering

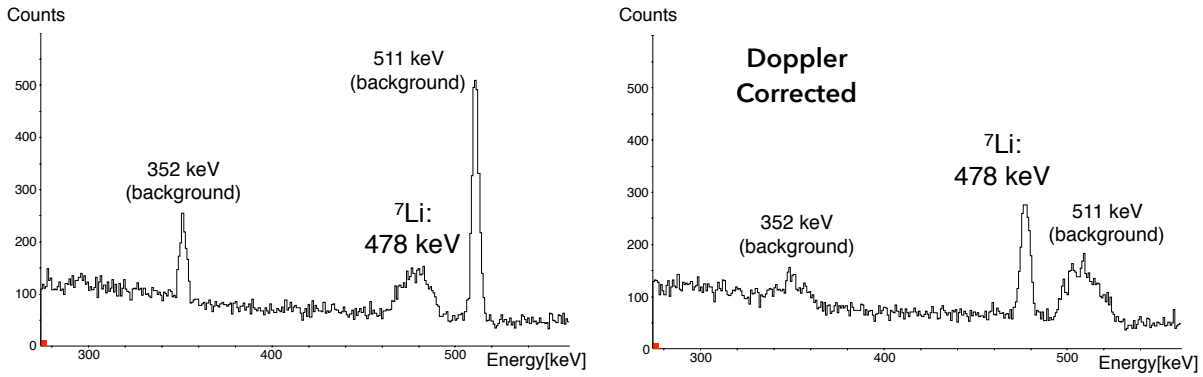

Figure 3.13: Left: the total γ–ray spectrum acquired during the ^{7}Li experiment. Right: the same part of the spectrum after the Doppler correction procedure.

the measured γ–ray and particle directions. Since the energy spectra were acquired for only 6 SPIDER strips, it was not possible to obtain the β value on an event-by-event basis. This value was therefore obtained from kinematics calculations. The resulting FWHM for the $1/2^{-} \longrightarrow g.s.$ transition, after applying the Doppler correction procedure, is 5.7 keV, which is in good agreement with the simulated value 5.4 keV obtained from the Monte Carlo code.

The bias modules used in the experiment gave the possibility to register the reverse current for each strip. At the end of the experiment the leakage current was $\sim$ 25 nA starting from a value below $\sim$ 1 nA. As it will be described in section 5.1 radiation damage effects were negligible.

The total number of counts obtained for the $1/2^{-} \longrightarrow g.s.$ transition is 2000(160), which is 20% lower than the GOSIA estimate. This discrepancy could be explained by an overestimation of the ^{27}Al target thickness and/or considering that the two conditions 2.5 and 2.6, needed for the semi-classical approximation to be applied, are not fully satisfied since the Sommerfeld parameter of this experiment is $\eta = 12.7$ and the ratio $\Delta E/E$ is $\sim 1/8$.

3.3 Acquisition System

The GALILEO project included the development of a novel digital electronics to be used also by the AGATA array. The use of a digital system enables a much more flexible treatment of the data and makes it possible to process data with rates of up to 50 kHz for each detector, using a configurable system with high integration, low power consumption and limited costs.

The GALILEO preamplifiers consist of a cold and a warm part. The cold part is lo-

cated in close proximity to the detector electrodes and operates at cryogenic temperatures. It consists of a low-noise silicon Field Effect Transistor (FET), a 0.5 pF feedback capacitance and a 2 GΩ feedback resistance. The warm part operates at room temperature and is located outside the cryostat. It comprises a low-noise trans-impedance amplifier, a pole-zero stage, a differential output buffer and a fast-reset circuitry.

SPIDER uses the same preamplifiers developed for the EUCLIDES light-particles array, described in [96]. Each preamplifier is composed by 16 differential channels arranged on a single card. The detectors are connected to the preamplifiers using cables[2] of $\sim$ 50 cm length, placed in vacuum. The dynamical range of the preamplifiers is $\sim$ 100 MeV, with a sensitivity of 45 mV/MeV. A dedicated Printed Circuit Board (PCB) was designed in order to couple the SPIDER detectors to the cables inside the GALILEO vacuum chamber. The board is fixed to the SPIDER holder and appears in figure 3.1 in green and in figure 3.7 (on left) in red. The use of this board makes it possible to mount or remove SPIDER for different experiments in only half an hour.

The scheme of the acquisition system is shown in figure 3.14. The differential output signals coming from the GALILEO and SPIDER preamplifiers are directly sent to the digitizers, each of them composed of six high-frequency ACD boards (Digi-Opt12) and two control cards. The Digi-Opt12 boards can handle 12 independent channels, providing for each of them a sampling of 100 Msps with a resolution of 14 bits (11.8 Effective Number Of Bits). Each control card is equipped with a Field Programmable Gate Array (FPGA) integrated circuit and manages three Digi-Opt12 boards, providing the synchronization between the different digitizers and performing other control processes described in details in Ref. [98]. The flux of data coming from the digitizer is sent to the pre-processing stage, executed by a front-end CPU (one for each digitizer) equipped with a read-out unit (RU) and in which is implemented the so-called "local filter" (LF). At this stage, a first-level trigger is fired when the corresponding energy of the input pulse exceeds a programmable threshold. The acquired channels are always grouped by two in what is called a "domain", individually the two channels of one domain are called "sub-domains". Only one of the two sub-domain can provide a trigger, the other is always acquired when the first fires a trigger. For GALILEO this is used to group together each HPGe detector with its BGO shield. In the SPIDER case only one sub-domain for each domain is used, the one that can provide the trigger. The energy computation is also performed in the preprocessing stage, using another FPGA integrated circuit. Two different energy estimations are performed: the "long-trace energy" is extracted from the signal that is processed using a trapezoidal filter implemented in the FPGA, while the "short-trace energy" is calculated as the difference between the amplitude of the acquired signal (not processed) and the

[2]JUNKOSHA mini-coaxial cables, with a 0.5 mm diameter and a capacitance of 96 pF/m [97].

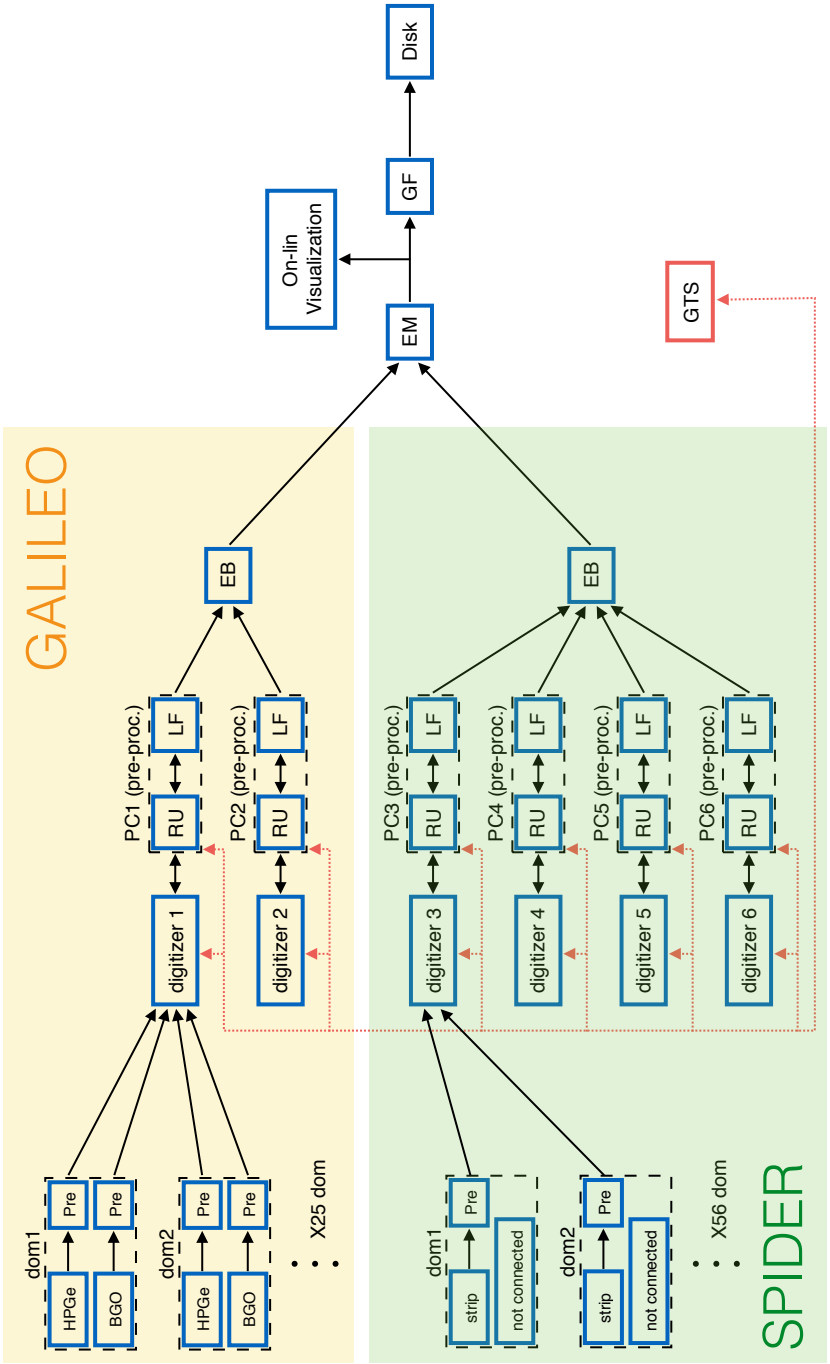

Figure 3.14: Scheme of the acquisition system of GALILEO and SPIDER at LNL. Pre is the preamplifier, RU is the Readout Unit, LF is the Local Filter, EB is the Event Builder, EM is the Event Merger, GF is the Global Filter and GTS is the Global Trigger and Synchronization system.

baseline, considering only a short sampling close to the trigger threshold. This short signal is also acquired and stored with a frequency of 1 signal over 1000. The trapezoidal shaping can be tuned by a set of programmable parameters controlled by the slow control system. The time information, which is necessary to correlate the GALILEO and SPIDER arrays, is obtained first from the timestamp distributed by the Global Trigger and Synchronization (GTS) system; then a finer estimation is made using two algorithms implemented in the preprocessing stage. Depending on the energy of the acquired signals a CFD or a leading-edge algorithm is used. The trigger request is sent to the GTS, while the computed energy and the other extracted information are stored in a Random Access Memory (RAM), waiting for the GTS validation. In case of an accepted event, the data are packed and sent to the next stage, while a rejection or time out frees the RAM area for another incoming event. The GTS is thus in charge of the trigger coordination and of the distribution of the phase-aligned, 100 MHz common clock used to synchronize the digitizers and the pre-processing modules. Also long-traces may be captured in triggered or non-triggered mode, with a length of up to a few hundreds of thousands of samples.

The acquired signals are grouped in events in two stages. In the first stage a global GALILEO event is built in the event builder (EB). In each event are stored the relevant information for all the signals included in a certain time window (1 μs for the ^{66}Zn experiment). The same is done for SPIDER using an independent event builder. In the second stage the GALILEO and SPIDER events are grouped together by the event merger (EM), if the first timestamps of the two events are included in another time window (1 μs in the ^{66}Zn experiment). The flux of data coming from the event merger is sent to the on-line visualization. Before sending the data to a PC for the final storage it is possible to set further trigger conditions using the global filter (GF), in order to save only the events relevant for the running experiment.

It has to be noted that the event builder and merger time windows, as well as the local and global filter conditions, are set only for practical reasons (such as to build coincidence events or to reduce the dimensions of the final acquired data). The system can work without any coincidence trigger, therefore it can be considered a full triggerless acquisition system.

3.4 Event Structure

In the ^{66}Zn experiment events with only γ–rays, only particles, and with γ-particle coincidences were acquired. Since the maximum expected rate in this experiment was about 0.5 kHz, well below the acquisition limit of 50 kHz for one detector, no multiplicity selection was applied in the acquisition system (a dead time lower then $\sim 1‰$ for each

channel is achieved for both GALILEO and SPIDER). When a trigger is validated by the GTS, a time window of 1 μs is opened in both the local and global filters. All the next validated signals are packed in the same event. For each γ–ray and particle the following informations are stored:

- domain: the detector ID
- timestamp: the time relative to the GTS clock
- time: the finer time information obtained from a CFD or a leading edge algorithm
- long-trace energy: the energy computed from the input pulse using the trapezoidal shaping
- short-trace energy: the energy computed from the pulse-height information of the short-traces (a less accurate estimation but useful for pile-up rejection)
- every 1000 signals also the short-trace is stored

The single γ–ray events are useful in order to monitor possible target contaminations. From γ–ray events, in which at least 2 photons are registered, it is also possible to produce γ-γ correlation matrices, useful for the identification of the reaction products. The single particle events can be used to measure the Rutherford cross-section and to obtain the beam energy and intensity, as well as the target thickness. Events with 2 or more particles (with or without γ–rays) can be related to real double-hit events or to cross-talk and charge-splitting events. These kind of events are neglected in the Coulomb excitation analysis but could be useful to monitor the SPIDER behaviour during the experiment. The single γ–ray and single particle coincidence events are the relevant data used for the final analysis. From the 2 or more γ–rays and one particle events is it possible to produce γ-γ-particle correlation matrices, useful in angular correlation measurements.

CHAPTER 4

CALIBRATIONS AND DATA REDUCTION

During the ^{66}Zn experiment, 560 GB of data were acquired with the GALILEO and SPIDER setup, over 4 days of measurement. In this chapter, the methods used for the calibrations of GALILEO (section 4.1) and SPIDER (section 4.2) will be described. In section 4.3 the conditions necessary to select γ-particle coincidences will be discussed, while in the last section (4.4) the possibility to exploit the Doppler effect, which affects the detected γ–ray energy, in order to extract further information about the experiment, will be described.

At the end of the data reduction, the acquired data have been reduced to: calibrated γ–ray spectra acquired in coincidence with back-scattered ^{66}Zn ions (with and without Doppler correction), calibrated singles γ–ray and singles particle spectra, calibrated γ-γ, particle-particle and γ-γ-particle correlation matrices. These data structures have been used in the analysis described in the next two chapters.

4.1 GALILEO

In the following text the GALILEO HPGe detectors will be labelled with SC for the 15 backward detectors (from SC0 to SC14) and with TC for the 10 detectors positioned at 90° (from TC0 to TC9) with respect to the beam direction (see figure 3.3). The HPGe SC0 ($\theta = 152°$, $\phi = 0°$) was powered off before the experiment, due to a malfunction related to the automatic cooling system.

4.1.1 Energy calibration

The HPGe detectors composing the GALILEO array have been individually energy calibrated using the following γ-sources: ^{22}Na, ^{54}Mn, ^{60}Co, ^{88}Y, ^{137}Ba, ^{137}Cs and ^{152}Eu.

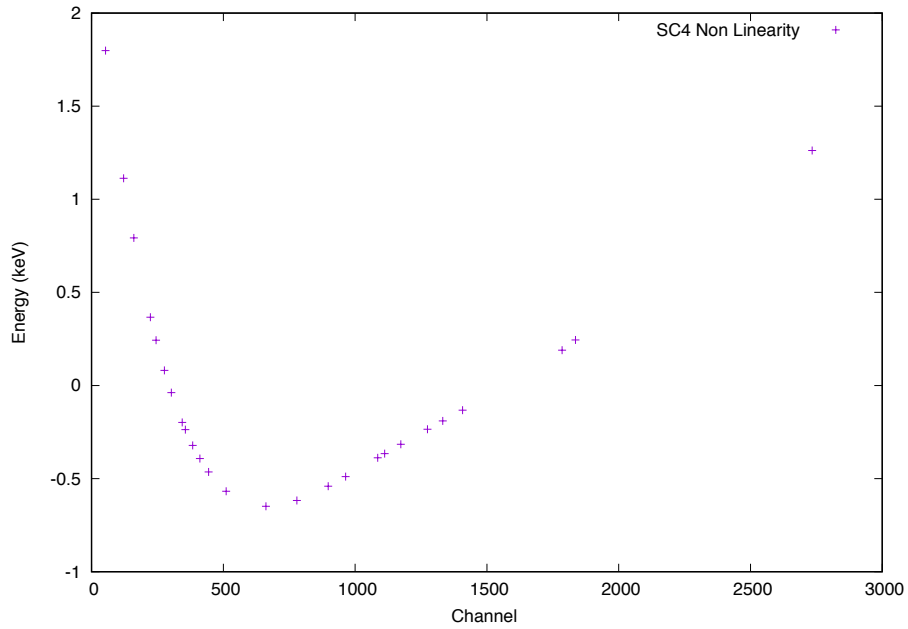

Figure 4.1: Non-linearity effect in one of the HPGe GALILEO detectors (SC4, $\theta = 152°$, $\phi = 288°$). See the text for details.

Since non-linearity effects are induced by the digitizers, a high number of sources, spanning a wide range of energies, is required to obtain a high-precision energy calibration. The deviation from linearity is shown in figure 4.1 for one of the GALILEO detectors: in the plot, the difference between the energy deduced from a linear fit to calibration points and the nominal energy of the different γ–rays emitted by the sources is reported, as a function of the channel number. In order to properly take into account and correct this non-linearity, a 6th-order polynomial has been fitted to the data, for each GALILEO detector. The obtained resolution, considering the entire GALILEO array and the 1332.5 keV transition of the ^{60}Co source, is 2.66 keV. The energy calibration with all the seven sources was performed before the experiment. Two γ–ray spectra of a ^{152}Eu source have been acquired in the middle and at the end of the experiment, to check the stability of the calibration over time.

4.1.2 Pileup Rejection

The pileup rejection can be performed by plotting the short-trace energy as a function of the acquired long-trace one (see figure 4.2, left panel). The short-trace energy estimation is assumed to be not affected by pileup, due to the short sampling time. Thus, a pileup rejection can be obtained, rejecting all the events that lie outside the diagonal presented in the figure (the actual accepted width was set to $\pm$200 ch). Figure 4.2 (right

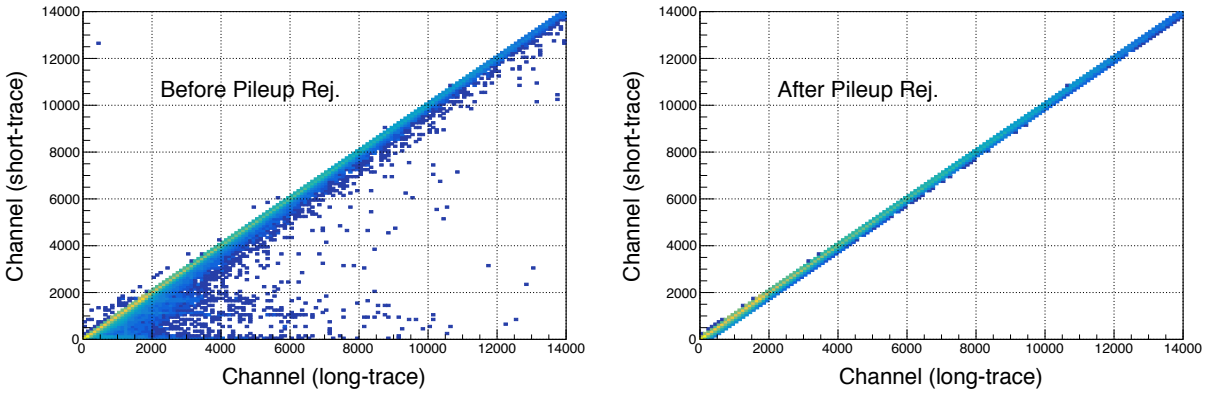

Figure 4.2: Left: matrix used for the pileup rejection, in which the short-trace energy is reported as a function of the long-trace one. Right: same picture after applying the pileup rejection procedure.

panel) shows the events remaining after the rejection, those that will be considered in the following analysis. The procedure has been performed using a ^{60}Co source. In this case, considering the entire GALILEO array, 1.3% of the total events were rejected. Since the rate of detected γ–rays during the Coulomb excitation experiment is lower than the one obtained with the ^{60}Co source, the rejected events during the measurement are even less, and are in practice negligible in the case of γ-particle coincidences. The counting rate in a Coulomb excitation with the detection of the scattered ions at backward angles is usually low, therefore this correction is not crucial. Nevertheless, it has been applied.

4.1.3 Compton Suppression

The suppression of the Compton background is performed in three different stages. The first one is implemented in the on-line acquisition and therefore it cannot be modified once the data are stored. The algorithm is based on the timing properties of each HPGe and its corresponding BGO shield. If the HPGe signal is in time coincidence with a signal coming from the BGO, the event is supposed to be a Compton scattering and thus is rejected. This is the main contribution to the improvement of the final peak-to-total ratio, but other two refinement algorithms have been implemented in the off-line analysis. The first off-line suppression is also based on the BGO and HPGe time information. While the on-line algorithm is based only on the timestamp information, and thus has a limited precision, in the off-line analysis also the time information coming from the CFD or leading edge algorithms can be taken into account. Again, if the HPGe and BGO signals are in time coincidence, the event is associated to a Compton scattering and is rejected. A second off-line algorithm can be also used, based on the energy information registered in

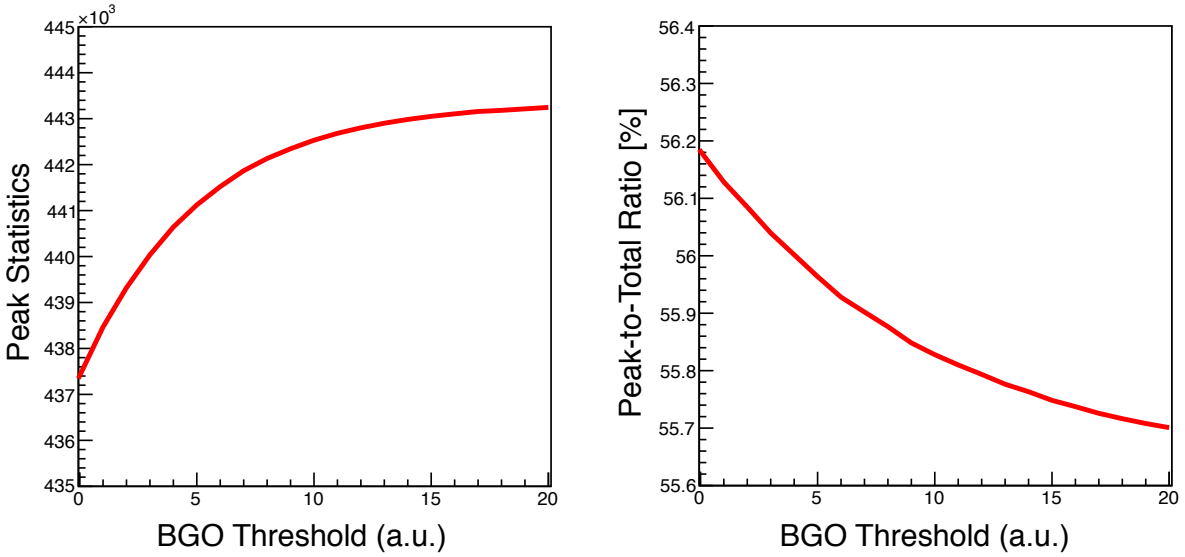

Figure 4.3: Total peak statistics (left) and peak-to-total ratio (right) reported as a function of the BGO energy threshold (given in arbitrary units). The plots refer to one GALILEO detector (SC2, $\theta = 152°$, $\phi = 144°$) and to a ^{60}Co source (the sum of the peaks corresponding to the 1173.2 keV and 1332.5 keV transition have been considered).

the BGO shields. When the HPGe detector fires a trigger, also the signal coming from its BGO shield is acquired. This signal can originate from noise or from a real physics event, such as a γ–ray that Compton scatters in the HPGe (random coincidences with the natural background can be considered negligible). If the amplitude of the signal coming from the BGO shield is higher than a certain threshold, the event can be associated to a Compton scattering and thus it is rejected. Since the BGO shields are not energy calibrated, an individual selection of the BGO energy thresholds has to be performed, looking to the peak-to-total ratio and to the rejected statistics as a function of the selected threshold.

When applying the three Compton suppression algorithms (1 on-line and 2 off-line) a compromise has to be kept between the improving of the peak-to-total ratio and the statistics loss. The parameters characterizing the procedures (the two time windows and the BGO energy thresholds) have been chosen using a ^{60}Co source, looking at the peak-to-total ratio and at the sum of the area of the 1173.2 keV and 1332.5 keV peaks, as a function of each parameter. An example is shown in figure 4.3, where the peak-to-total ratio and the total peak statistics are reported as a function of the BGO energy threshold (the plots refer to a single HPGe detector). Since the expected Compton background is not large in the ^{66}Zn experiment, a final value of 15 a.u. for the energy threshold was chosen, giving priority to avoid the statistics reduction.

Considering the ^{60}Co source a peak-to-total ratio of 55.7% was achieved after the first

on-line Compton suppression. This value increases to 59.1% after the off-line stages, with a total loss of statistics of 3.6%. In the in-beam experiment, considering the $2_1^+ \longrightarrow 0_{g.s.}$ transition in ^{66}Zn, a 1.5% statistics reduction is obtained when the two on-line procedures are applied.

4.1.4 Efficiency Measurement

The absolute photopeak efficiency[1] ϵ_{abs} of GALILEO was measured before the experiment (see figure 4.4), with the same γ-sources used for its energy calibration. Only the peaks whose relative intensities are known with high precision were considered. The data have been fitted using the empirical function [99]

$$\epsilon\left(E_\gamma\right) = \exp\left\{\left[\left(A + Bx + Cx^2\right)^{-G} + \left(D + Ey + Fy^2\right)^{-G}\right]^{-1/G}\right\} \tag{4.1}$$

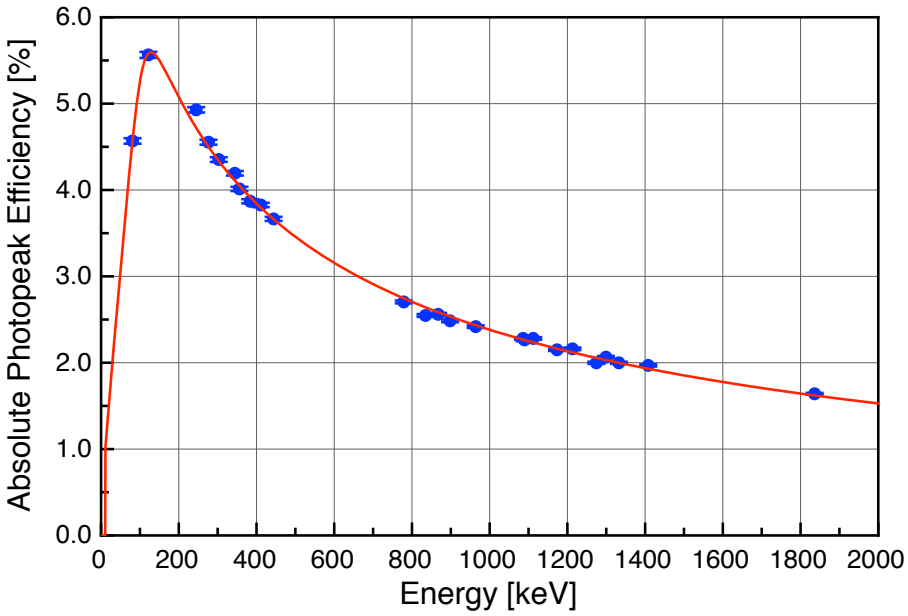

Figure 4.4: Absolute photopeak efficiency for the entire GALILEO array as a function of the γ–ray energy. The measured efficiencies are reported in blue, while the fitted function is shown in red. The picture refers to 24 HPGe detectors, since SC0 was not used in the ^{66}Zn experiment.

[1] Absolute photopeak efficiency here means the number of detected γ–rays with respect to the ones that are emitted by the source. These are obtained considering the source activity at the moment of the measurement, the duration of the measurement, the acquisition dead time and the relative intensities of each γ–ray transition. Relative photopeak efficiency (used in the following) here means the number of detected γ–rays with respect to only the relative intensities of each γ–ray transition. In both the definitions only the photopeak events are considered.

where $x = \ln(E_\gamma/100)$, $y = \ln(E_\gamma/1000)$ (E_γ is the γ–ray energy in keV) and $A - G$ are the fitted parameters. The obtained value of the GALILEO absolute photopeak efficiency at 1332.5 keV is $\epsilon = 2.0\%$. This value has been obtained without considering the pileup rejection and only the first on-line Compton suppression stage. When both corrections are applied, the value of $\epsilon\,(E_\gamma = 1332.5$ keV) is reduced by 4.6 %. This measurement was performed in order to evaluate the effect of the presence of SPIDER inside the GALILEO vacuum chamber on the γ-detection efficiency. Since materials composing SPIDER and its holder have been kept as thin as possible, the efficiency is about the same of the one without SPIDER. The efficiency calibrations were also repeated, using only the ^{152}Eu source, in the middle and at the end of the experiment, in order to check the stability of the GALILEO electronics.

The relative photopeak efficiency for each GALILEO HPGe detector was also measured. In this case, the experimental values were fitted using the GREMLIN code [85]. The function used in the code takes into account the efficiency dependence on E_γ in two separate energy ranges (high and low γ–ray energy regions), and can be easily imported into GOSIA for the final Coulomb excitation analysis.

4.2 SPIDER

The SPIDER strips are identified by a code that indicates the detector (from D0 to D6) and the strip (from S0 to S7 as shown in figure 3.4). An entire detector (D3, positioned at $\phi \sim 98°$) was powered off during the experiment, and also one strip (D1S6, $\theta = 134.6°$, $\phi = 355°$) was not used. This was due to a malfunction related to the electronic connections between SPIDER and the preamplifiers.

4.2.1 Energy calibration

Using a ^{66}Zn beam with an energy of 240 MeV and a ^{208}Pb target, the back-scattered projectiles can reach energies up to 80 MeV. Since no standard sources can provide reference particles at such energies, the calibration was performed using an α-source, which emits three α-particles at an energy of ~ 5 MeV, and an extrapolation to higher energies with a pulse generator. In principle, also the elastic scattering of ^{66}Zn can be used for the energy calibration. However, as will be explained in the next chapter, unknown amount of ^{12}C and ^{16}O contaminants deposited in the target, prevents the achievement of the requested accuracy in the calculation of the elastic peak energy. For this reason, as a first approximation, only the α-source and the pulser data have been used. A further refinement will be obtained by exploiting the Doppler effect as explained in section 4.4.2.

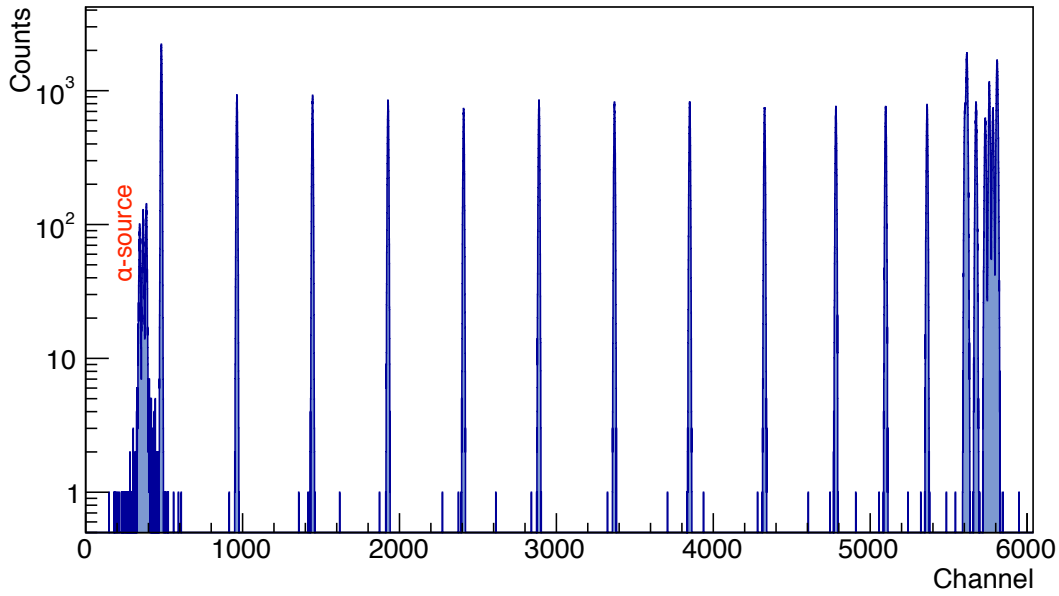

Figure 4.5: Energy calibration spectrum acquired by one SPIDER strip. The α-particles emitted by a triple alpha source ^{239}Pu+^{241}Am+^{244}Cm have been detected together with a set of signals, equally spaced in amplitude, provided by a pulser. Non-linearity effects are visible starting from channel ~ 5000.

A set of pulser signals, equally spaced in amplitude, was fed to the SPIDER preamplifier, individually for each channel. The minimum amplitude V of the signal was set to 0.5 V, while the amplitude spacing between consecutive signals was 0.5 V. At the same time, the α-source was placed at the target position. In order to use the pulser signals for energy calibration, the energy corresponding to each peak has to be found ($E_p = E_p\,(ch_p)$). For both the alpha and pulser peaks the channel number was obtained by a fit to the corresponding peaks in non-calibrated spectra. A calibration spectrum is shown in figure 4.5, where it is also visible how, above a certain signal amplitude (channel ~ 5000), non-linearity effects induced by the pre-amplifiers are present. Considering the first 6 pulser peaks, which show a linear trend as a function of the channel number (see figure 4.6), it is possible to obtain the conversion between the signal amplitude and the channels number from a linear fit:

$$V = V\,(ch) = m \cdot ch + q \tag{4.2}$$

where ch is the channel number and m, q are the parameters fitted individually for each strip. The same equation can be applied to the alpha peaks in order to get the signal amplitude from the channel number. The next step in the calibration procedure is to convert the signal amplitude in energy. This can be achieved using an alpha peak as a normalization value ($E_\alpha = 5.486$ MeV was used). By defining $X \equiv E_\alpha / ch_\alpha$ and assuming

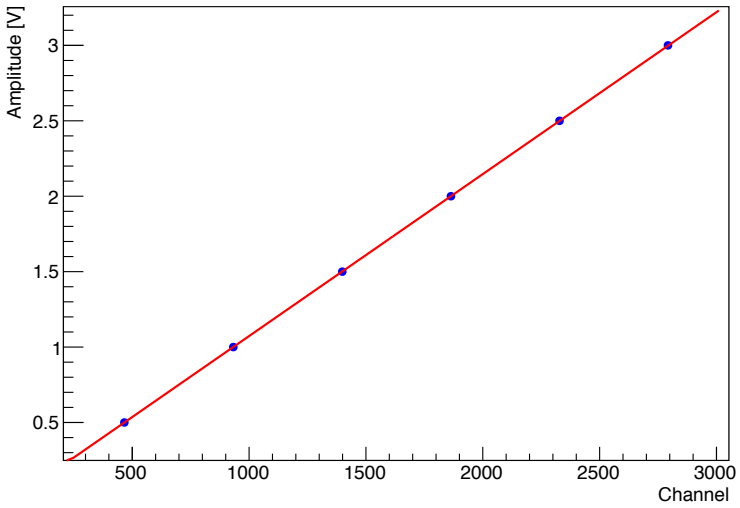

Figure 4.6: Signal amplitude as a function of the channel number for the first 6 pulser peaks, measured by one SPIDER strip (D5S3, $\theta = 144.2°$). The data are shown in blue (the error bars are smaller than the marker size), while the linear fit is shown in red.

that $V \propto E$, it is possible to obtain:

$$\frac{V_\alpha}{V_p} = \frac{E_\alpha}{E_p} \longrightarrow E_p = E_\alpha \frac{V_p}{V_\alpha} = E_\alpha \frac{m \cdot ch_p + q}{m \cdot ch_\alpha + q} = X \frac{m \cdot ch_p + q}{m + \frac{q}{ch_\alpha}} \tag{4.3}$$

that provides the conversion between the pulser channel number and the pulser energy $E_p = E_p\,(ch_p)$, for each SPIDER strip. The energy of each pulser peak calculated from equation 4.3 was used to calibrate in energy the SPIDER strips. The assumption $V \propto E$ is clearly valid only in the linear region, thus this procedure has been applied only to the first 6 pulser peaks ($E_{pi} = E_{pi}\,(ch_{pi})$ with $i = 1, ..., 6$). For the following pulser peaks, the expected energy has been deduced adding the energy difference between the previous peaks ($\Delta E \equiv E_{p2} - E_{p1} = E_{p3} - E_{p2} = E_{p4} - E_{p3}$):

$$E_{pi} = E_{p(i-1)} + \Delta E \qquad\qquad i = 7, ... \tag{4.4}$$

The calculated energy of the pulser and α-source signals is reported in figure 4.7, as a function of the channel number, for one SPIDER strip. The data were fitted using a 6th-order polynomial, reproducing the non-linearity effects.

4.2.2 Pileup Rejection

The procedure for pileup rejection described in section 4.1.2 has been also applied to the particle spectra acquired during the experiment (the rate for particles emitted from the α-source is too low to observe pileup). The total rejected statistics, considering

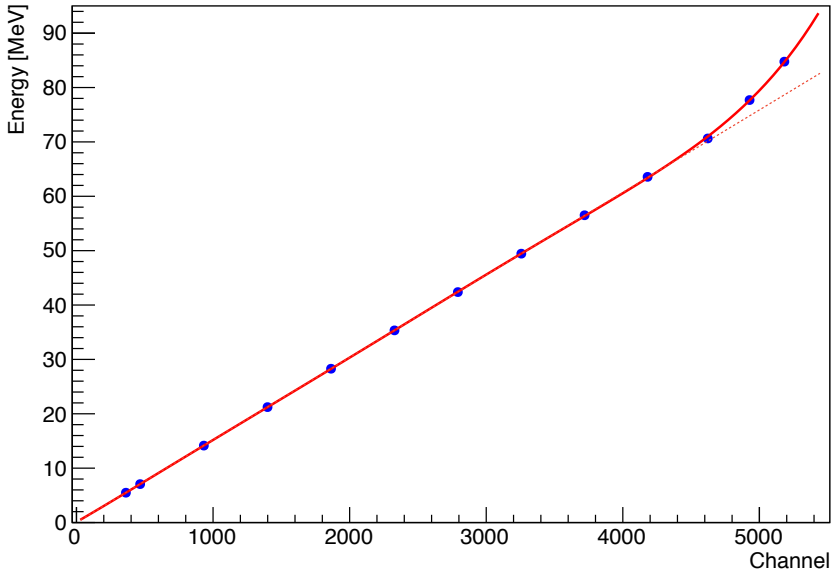

Figure 4.7: Calculated energy as a function of the channel number for a single SPIDER strip (the same of figure 4.6). The data are shown in blue (the error bars are smaller than the marker size), while the 6th-order polynomial fit is shown in red (continuous). The first data point (channel ~ 350) is the considered peak of to the α-source. The effect of non-linearity of the SPIDER preamplifiers is visible above an energy of ~ 70 MeV (dashed line).

both elastic scattering and Coulomb excitation events, is less than 4‰. It is clear that for Coulomb excitation measurements where the scattered ions are detected at backward angles this correction is irrelevant.

4.3 Selection of Coincidences

In this section, the criteria used to select γ-particle, γ-γ, γ-γ-particle and particle-particle coincidences will be presented. These include a time condition, a multiplicity selection and a particle energy selection.

4.3.1 Time Coincidences

As described in section 3.3 the time window of the acquired events is 1 μs. In each of them one or more γ–ray and one or more particles can be registered. In order to select γ-particle coincidences, the time properties of GALILEO and SPIDER have to be considered.

The choice between the two algorithms used for the time estimation, the CFD and the leading edge, depends on the signal amplitude. For small amplitudes the CFD algorithm

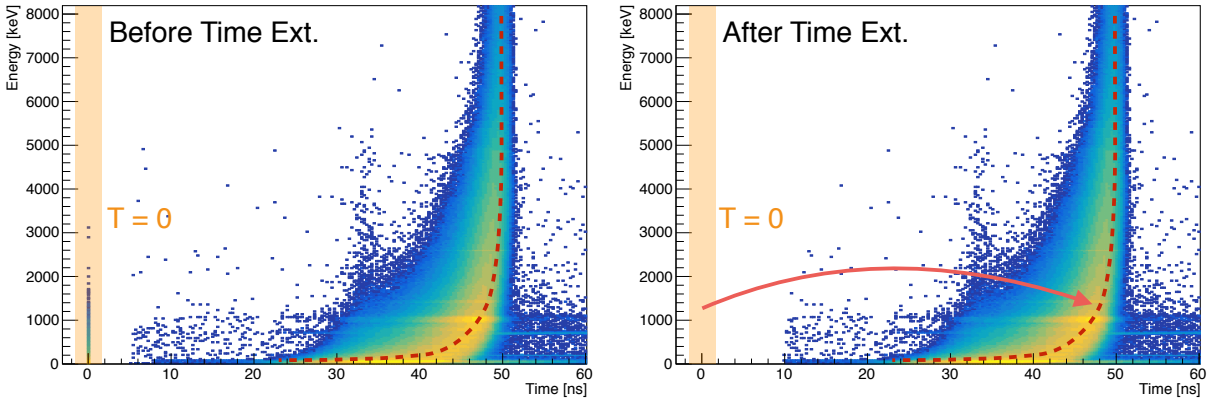

Figure 4.8: Left: GALILEO energy as a function of the time. The events with time equal to zero are highlighted in orange. The dashed line is plotted to guide the eyes, and it is not the fit result. Right: the same figure after the time extrapolation. The red arrow represents the shift of the events with time zero in the extrapolated position.

is used, in order to correct for the time walk effect. For large amplitude signals this effect is negligible and therefore the simpler and faster leading edge algorithm is preferable. When the CFD algorithm fails (for instance when two signals are too close in time), the time information T is set to zero and only the timestamp information is retained. In order to correctly reproduce the event time structure, an extrapolation procedure for the signals having time information $T = 0$ was implemented. The procedure is exemplified in figure 4.8 for one of the GALILEO HPGe detectors. First, the dashed line on the left panel (representing the locus of maximum intensity in the time-energy plane) was fitted by the empirical function

$$t\,(E) = const + \sum_{i=1,\ldots,4} c_i\,(\ln E)^i \tag{4.5}$$

where *const* and c_i are the fitted parameters. Then a new value of T was assigned to the events having $T = 0$, which brought them onto the dashed line (4.8 right panel).

The on-line synchronization performed by the GTS (described in section 3.3) has a finite precision and a time misalignment of the acquisition channels is observed in the final data. This effect is visible for the GALILEO part considering γ-γ coincidences. In figure 4.9 (left panel) the time differences between the γ–rays detected by a reference HPGe (SC1) and the γ–rays detected by all the others (identified by the domain) are shown. The time alignment of the different channels has been obtained by adding an empirical offset to shift the coincidence peaks to zero, as shown in 4.9 (right panel). The SPIDER strips have been aligned using the same method, considering again the SC1 HPGe detector as a reference and the Coulomb excitation γ-particle coincidences.

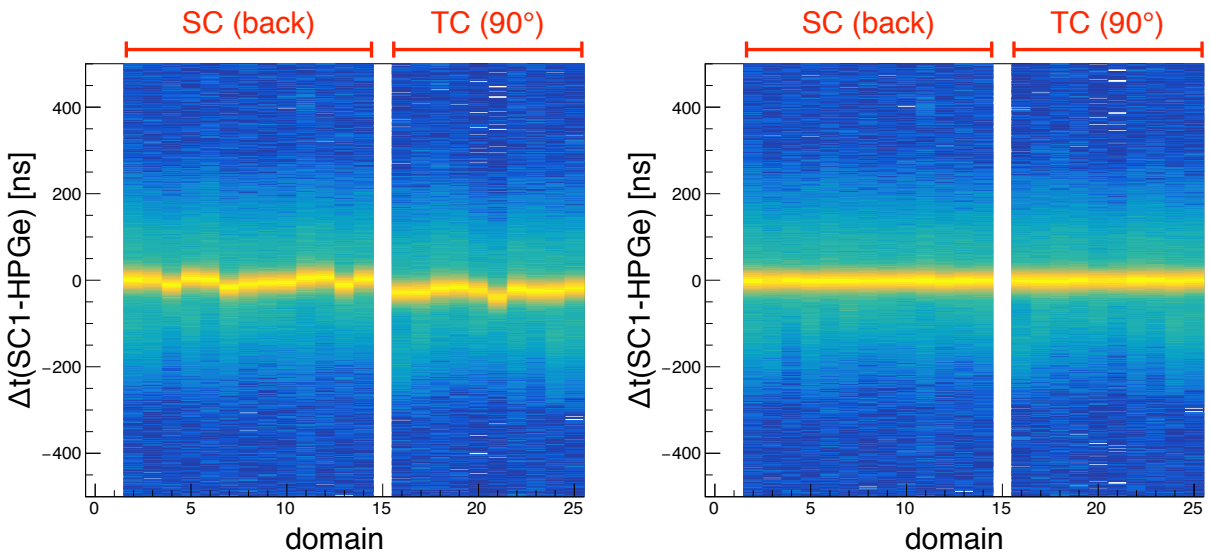

Figure 4.9: Left: time difference between the reference HPGe detector (SC1) and the other detectors (identified by their domain), γ-γ coincidences have been considered in this matrix. Right: the same plot after the time alignment procedure.

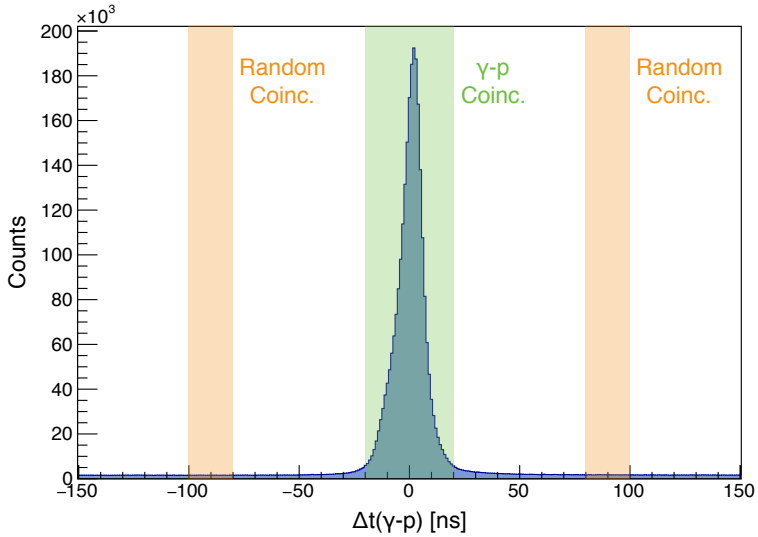

Figure 4.10: Time difference spectrum of γ-particle coincidences. The time window used for the Coulomb excitation coincidences is highlighted in green, the two time windows used for the random coincidences subtraction in orange.

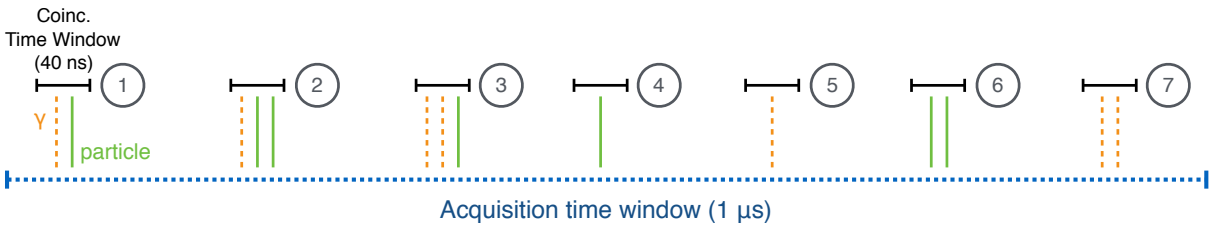

Figure 4.11: Possible acquired events (see section 3.4 for the physical meaning): 1) γ-particle, 2) γ-particle-particle, 3) γ-γ-particle, 4) particle singles, 5) γ singles, 6) particle-particle, 7) γ-γ. Higher multiplicity events, which have negligible statistics, are not considered.

After the time extrapolation and the time alignment procedures have been applied, the time windows for the γ-particle, γ-γ, particle-particle and γ-γ-particle coincidences have been selected. In figure 4.10 the number of γ-particle coincidences is reported as a function of the time difference between particles and γ–rays related to the Coulomb excitation of ^{66}Zn. In this case, a time window of 40 ns has been chosen. Also the two time windows used for the evaluation of random coincidences (each of 20 ns width) are shown in the figure.

4.3.2 Multiplicity Selection

Several coincidence events can be included in an acquisition time window, as summarized in figure 4.11. Only one γ–ray and one particle coincidences (type 1) can be analysed using the GOSIA code[2]. Requiring only the time coincidence, also the events labelled as 2 and 3 in figure 4.11 can be included in the data since they have one γ–ray and one particle. In order to reject these events, a multiplicity filter has been implemented, and only events having multiplicity equal to one for both the γ–rays and for the particles (labelled as 1 in figure 4.11) are selected for the final Coulomb excitation analysis.

4.3.3 Particle Energy Selection

In Coulomb excitation experiments where the particle detection is performed at forward angles, particle energy selection has to be used in order to distinguish between the projectile and the recoiling target nuclei, in order to reconstruct the kinematics. If instead, the particle detector is positioned at backward angles, only the back-scattered projectiles can be detected. However, to reject signals associated to noise, particle energy selection

[2]It is possible also to analyse 2 γ–rays and 1 particle coincidences, but this requires a different approach not used in this thesis.

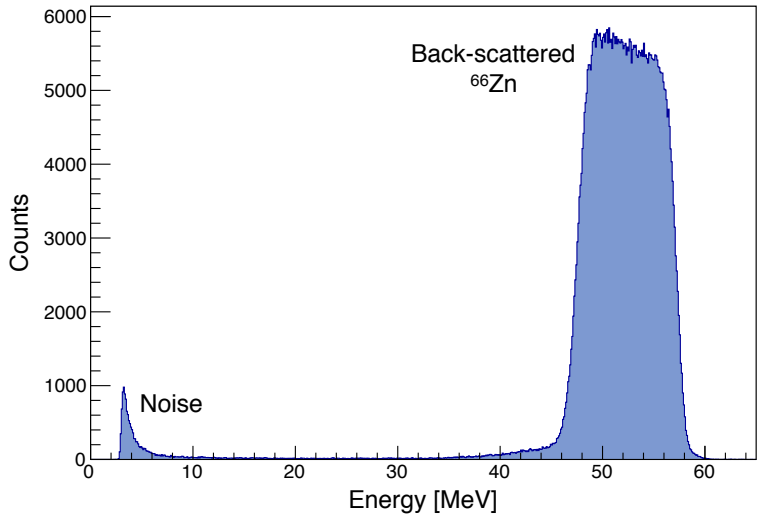

Figure 4.12: Example of energy spectrum relative to a SPIDER strip ($\theta = 158.5°$). The back-scattered projectiles and the noise contribution are visible.

is necessary. A SPIDER strip energy spectrum is shown in figure 4.12, where the contribution of noise is indicated. In order to avoid this contribution, an energy selection has been applied individually for each strip, based on a low and in a high energy threshold, outside which the events are excluded.

4.4 Further Applications of the Doppler Correction

The scattering process between the projectile and the target nuclei may occur at any depth inside the target. Four limiting cases shown in figure 4.13, characterized by the scattering angles θ^1_{min}, θ^1_{max}, θ^2_{min} and θ^2_{max}, can be considered. Assuming the target thickness ($\sim 1\ \mu$m) to be negligible with respect to the target-detector distance (~ 10 cm) and the SPIDER polar angular coverage values shown in table 3.1: $\theta^1_{max} = \theta^2_{max} = 161°$ and $\theta^1_{min} = \theta^2_{min} = 123°$. If the excitation occurs just in the front surface of the target (θ^1_{min}, θ^1_{max}) the de-excitation happens always outside it. In the other two cases (θ^2_{min}, θ^2_{max}) the de-excitation can occur, in principle, also inside the target, depending on the stopping powers, the beam energy, the lifetimes of the excited states and the scattering angles. Using the equations reported in section 2.3 and the stopping powers taken from SRIM [84], the energy after the scattering on the back surface of the target has been obtained: $E'(\theta^2_{max}) \sim 60$ MeV and $E'(\theta^2_{min}) \sim 80$ MeV. Considering also the energy loss in the target, the energies at the target exit are reduced to $E'(\theta^2_{max}) \sim 50$ MeV and $E'(\theta^2_{min}) \sim 60$ MeV. Therefore the minimum energy after the scattering, once the ions exit from the target, is $E'_{min}(\theta^2_{max}) \sim 50$ MeV, corresponding to $\beta_{min} = v/c = 4\%$. The

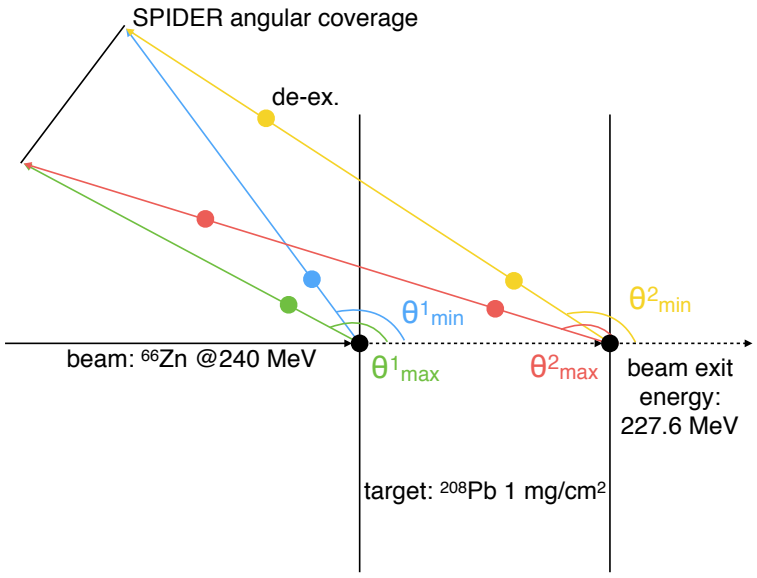

Figure 4.13: Scheme of the 4 limit cases of ^{66}Zn Coulomb excitation inside the target. The black dots represent the scattering process (the excitation), the coloured dots represent the de-excitation. The target thickness is intentionally exaggerated in order to better identify the different scattering positions.

lifetime of the 2_1^+ state in ^{66}Zn is 2.4 ps and can be assumed as the (mean) minimum time interval between an excitation and the corresponding de-excitation. The mean distance that the scattered projectiles cover in this interval, between the interaction point and the de-excitation, can be calculated as

$$d_{min} = \beta_{min} \cdot c \cdot \tau \left(2_1^+ \longrightarrow 0_1^+\right) \sim 30\ \mu\text{m} \tag{4.6}$$

more than one order of magnitude larger than the target thickness (1 mg/cm^2 of ^{208}Pb corresponds to 0.88 μm). This represents a mean lower limit, thus we can assume that the de-excitation occurs almost always outside the target. In this condition, the energy registered in SPIDER corresponds to the energy after the de-excitation process, and can be used in the Doppler correction procedure.

By using equation 2.45 it is possible to reconstruct the energy of the emitted γ–ray E_0 (the one observed in the reference frame fixed to the de-exciting nucleus) from the Doppler shifted one (the one observed in the laboratory reference frame) that is detected E_{det}:

$$E_0 = \gamma E_{det} \left(1 - \beta \cos\vartheta\right) \tag{4.7}$$

where ϑ is the angle between the directions of the scattered particle and the emitted γ–ray, defined by equation 2.46, γ is the Lorentz factor and

$$\beta = \sqrt{\frac{2E_{lab}}{A}} \tag{4.8}$$

where $A\,[u]$ is the mass in atomic units of the scattered projectile and $E_{lab}\,[MeV]$ is its energy. The latter corresponds to the energy detected by SPIDER, since de-excitation occurs outside the target. It is also possible to obtain β using the equation 2.43, if the beam energy and the scattering angle are known. Both these approaches have been used in the analysis and, in the following, will be referred to as the "Doppler correction using the SPIDER energy" and the "Doppler correction using the kinematics" respectively.

The Doppler correction procedure can also be used in order to obtain the relative positions of the GALILEO HPGe and SPIDER strips, to verify the SPIDER energy calibration and to evaluate, without using the energy registered in SPIDER, a mean energy of the de-exciting ^{66}Zn nuclei. The basic idea is that the width of the Doppler corrected γ–rays peaks is minimized once the best combination of β and ϑ is found.

4.4.1 SPIDER Angles Optimization

The aluminium frame shown in figure 3.7 (right panel) was unfortunately not ready for the ^{66}Zn experiment. A 3D-printed plastic prototype was used instead, thus a perfect positioning was not possible. The angles identifying the SPIDER strips are therefore different from the ones reported in table 3.1, which were calculated assuming the perfect centering. The actual angles have been calculated exploiting the Doppler shift of the γ–ray energies.

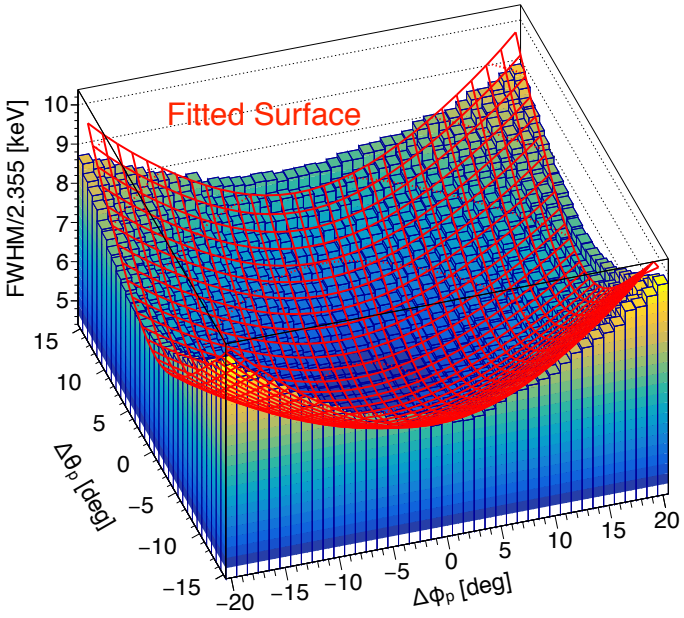

Figure 4.14: Example of 3D plot used to determine the SPIDER angles, referred to one strip. The standard deviation of the fitted peak in the γ–ray spectra is reported as a function of the two offset $\Delta\theta_p$, $\Delta\phi_p$ (see the text for the details).

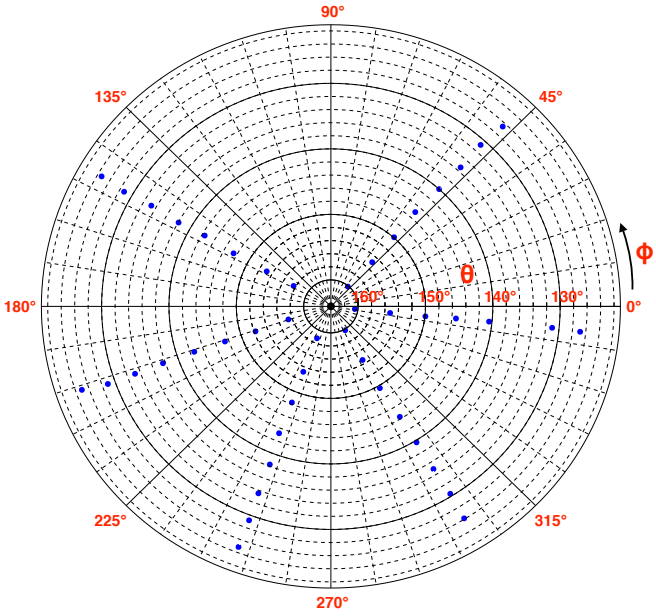

Figure 4.15: The center-of-mass angles of each SPIDER strip are reported using blue dots. The misalignment with respect to the beam axis is visible.

Two offsets ($\Delta\theta_p$, $\Delta\phi_p$) have been added to the angles that identify the SPIDER strips (θ_p, ϕ_p). The quantity $\cos\vartheta$, defined in equation 2.46, is then written as

$$\cos\vartheta = \sin(\theta_p + \Delta\theta_p)\sin(\theta_\gamma)\cos[(\phi_p + \Delta\phi_p) - \phi_\gamma] + \cos(\theta_p + \Delta\theta_p)\cos(\theta_\gamma) \qquad (4.9)$$

Once the value of β, obtained from the energy registered in SPIDER, is fixed, the Doppler correction procedure can be applied producing γ–ray spectra for the different combinations of $\Delta\theta_p$ and $\Delta\phi_p$. The γ-peak corresponding to the most intense transition ($2_1^+ \longrightarrow 0_1^+$) has been fitted and the FWHM has been extracted for each γ–ray energy spectrum. The results are reported in 4.14 for one SPIDER strip, as a function of $\Delta\theta_p$ and $\Delta\phi_p$. A polynomial surface (the product of two 6th-order polynomials with 14 free parameters) has been fitted to the data (1200 values of FWHM). The minimum of this surface represents the best combination of $\Delta\theta_p$ and $\Delta\phi_p$ that minimize the Doppler broadening. The same procedure can be applied by minimizing the absolute value of the difference between the known $2_1^+ \longrightarrow 0_1^+$ transition energy (1039 keV) and the corresponding energy obtained fitting the γ–ray energy spectra. Also in this case, the difference is minimum when the Doppler shift is minimized. The final adopted angles (θ'_p, ϕ'_p), for each SPIDER strip, can be written as:

$$\theta'_p = \theta_p + \Delta\theta_p \qquad \phi'_p = \phi_p + \Delta\phi_p \qquad (4.10)$$

where θ_p, ϕ_p are the starting values reported in table 3.1 (calculated in the hypothesis of a perfect centering) and $\Delta\theta_p$, $\Delta\phi_p$ are the offset obtained minimizing the Doppler effect.

The two procedures (minimization of the FWHM and minimization of the centroid shift) produce similar values of $\Delta\theta_p$, $\Delta\phi_p$. In figure 4.15 the adopted SPIDER strips angles θ'_p, ϕ'_p are shown: the de-centering is evident. The SPIDER strips angles can be also calculated starting from the geometry of figure 3.8. Considering also the bad centering, the agreement between the two set of values is verified within an error of about 1 degree.

4.4.2 SPIDER Energy Optimization

The procedure applied to determine the SPIDER mean angles has been also implemented to check the SPIDER energy calibration. In this case the SPIDER angles have been fixed to the values obtained after the Doppler correction optimization. An additional offset ΔE^{cal}_{lab} has been added to the registered energy in SPIDER E_{lab} in equation 4.8:

$$\beta = \sqrt{\frac{2\left(E_{lab} + \Delta E^{cal}_{lab}\right)}{A}} \tag{4.11}$$

A polynomial fit (4th order) has been performed in order to obtain the value of ΔE^{cal}_{lab} corresponding to the minimum FHWM of the peak associated to the $2^+_1 \longrightarrow 0^+_1$ transitions (see figure 4.16). The result of this procedure is reported in figure 4.17 (left), for

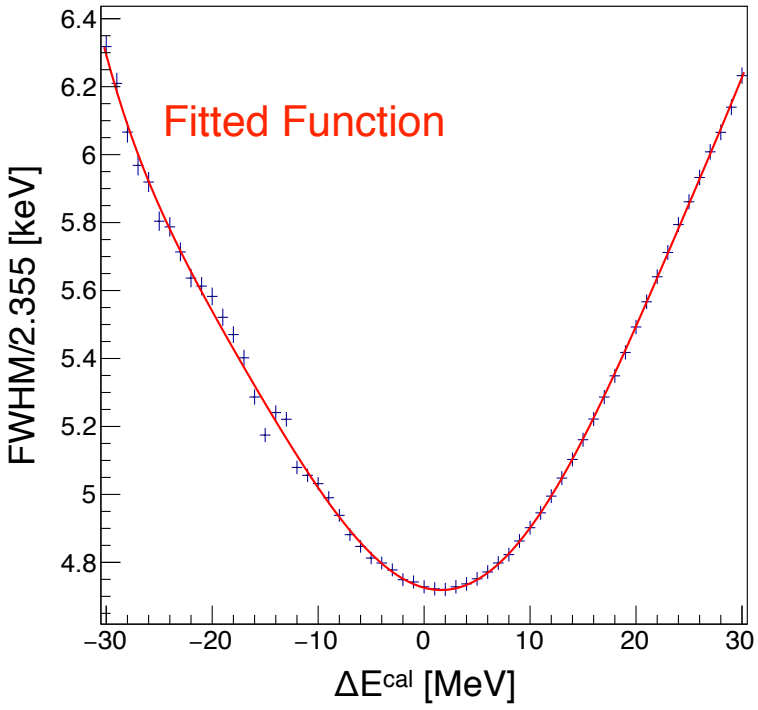

Figure 4.16: Standard deviation of the fitted peak as a function of the energy calibration offset ΔE^{cal}_{lab} for one SPIDER strip. The fit results are shown, together with error bars, in blue. The polynomial fit, from which the minimum FWHM is obtained, is shown in red.

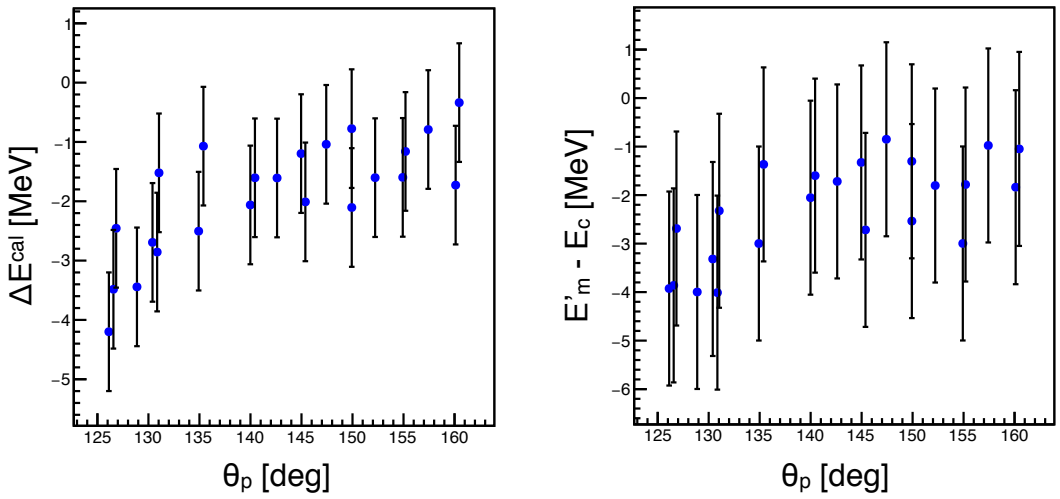

Figure 4.17: Left: calibration offset ΔE_{lab}^{cal} for the different SPIDER strips, as a function of their center-of-mass polar angle obtained from the Doppler correction minimization. An error of $\sim$ 1 MeV has been estimated considering different sets of data. Right: energy difference between the mean energy values obtained from the Doppler correction procedure E'_m and the energy registered in the SPIDER strips.

all the SPIDER strips, as a function of their center-of-mass θ angle. A systematic offset of $\Delta E_{lab}^{cal} \sim -1$ MeV is visible, which increases in absolute value for smaller angles up to -4 MeV. This trend can be interpreted considering that for smaller scattering angles the energy registered in the SPIDER strips is closer to the non-linear region of the preamplifiers (4.7). It is interesting to notice how the improper centering of SPIDER inside the vacuum chamber is also visible using the SPIDER energies (figure 4.18), after applying the offset ΔE_{lab}^{cal} to the calibration (for larger scattering angles smaller energies are registered considering the same SPIDER ring).

4.4.3 Particle Energy Without SPIDER

The procedure used in the previous section has been also applied to obtain a mean energy of the scattered particles for each SPIDER strip. This value does not depend on the energy information registered in SPIDER and therefore represents a useful check of the internal consistency of the SPIDER energy calibrations. The resulting mean energy will be also used in the Doppler correction procedure using the kinematics. As a starting value, the mean energy E_m for each SPIDER strip has been obtained from kinematics calculations, using the equation 2.43. The beam energy and the SPIDER angles obtained from the Doppler correction minimization have been used in these calculations.

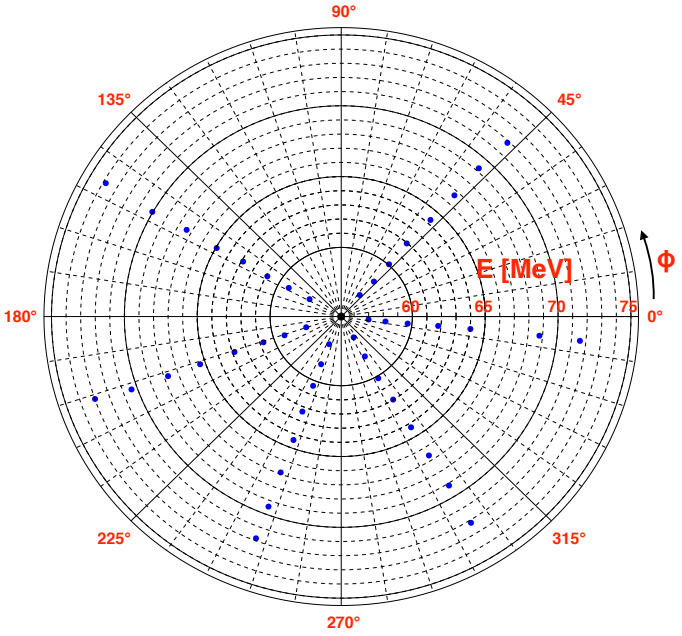

Figure 4.18: The detected energies, related to the front surface scattering of ^{66}Zn on ^{208}Pb, are reported using blue dots for each SPIDER strips. The misalignment with respect to the beam axis is visible, as in the case of figure 4.15.

An additional offset ΔE_m has been added in the equation 4.8:

$$\beta = \sqrt{\frac{2\,(E_m + \Delta E_m)}{A}} \tag{4.12}$$

and the same minimization procedure, previously described, was repeated in order to obtain the value of ΔE_m that minimize the Doppler effect. The mean energy

$$E'_m = E_m + \Delta E_m \tag{4.13}$$

corresponds to the centroid of the particle energy distribution E_c, which can be deduced from the calibrated SPIDER energy spectra. In figure 4.17 (right) is shown the difference $E'_m - E_c$ as a function of the scattering angle. Again it is seen how, for smaller scattering angle, this value is higher. This may suggest a systematic error on the SPIDER energy calibrations, possibly due to an imperfect estimation of the preamplifiers non-linearity.

4.5 Final γ-particle Coincidence Spectra

The procedures described in the sections 4.4.1, 4.4.2, 4.4.3 have been applied to obtain the better combination of SPIDER angles, SPIDER energy calibration offsets and mean energies of the particles, to be used in the final Doppler correction.

Figure 4.19 shows three comparisons between two portions of the total γ–ray spectrum acquired in coincidence with the back-scattered ^{66}Zn ions. The spectra in the middle panels (labelled as DC Proj.) correspond to the ones reported in the upper panels (No DC) after applying the Doppler correction procedure using the SPIDER energy for the projectile nuclei (^{66}Zn). The final FWHM of the Doppler corrected peak associated to the $2_1^+ \longrightarrow 0_1^+$ transition at 1039 keV is 10.9 keV. After the Doppler correction procedure using the kinematics, which does not take into account the energy loss into the target associated to the different interaction points, a FWHM of 11.3 keV is obtained. The latter procedure is implemented in the GEANT4 simulations reported in figure 3.9, which gives a FWHM = 11.8 keV. A good agreement between experiment and simulation is obtained. By a comparison of the Doppler corrected spectrum (DC Proj., left) with the simulated one (figure 3.9), it is visible that the intensity of the $0_2^+ \longrightarrow 2_1^+$ transition was overestimated. This is due to the fact that the $B\,(E2)$ upper limit reported in the literature [100] (the only available experimental information) was employed in the GOSIA calculations, used as an input for the GEANT4 simulations. In the lower panels (DC Target) the Doppler correction has been applied for the target nuclei. The direction and the energy of the recoiling target nuclei were deduced from the impact position and energy of the detected ^{66}Zn ions (both obtained from SPIDER). These informations allow to apply a Doppler correction procedure also to the target ions, even though they are not directly observed. From the spectra, it is clearly visible how only ^{208}Pb and isotopic contaminants are present in the target. The FWHM of the peak at 570 keV ($5/2_1^- \longrightarrow 1/2_{g.s.}^-$ transition of ^{207}Pb) is 4.4 keV, the one at 803 keV ($2_1^+ \longrightarrow 0_{g.s.}^+$ transition of ^{206}Pb) is 4.7 keV and the one at 2614 keV ($3_1^- \longrightarrow 0_{g.s.}^+$ transition of ^{208}Pb) is 18.8 keV. These values can be used as a reference to plan future experiments in which the target is excited.

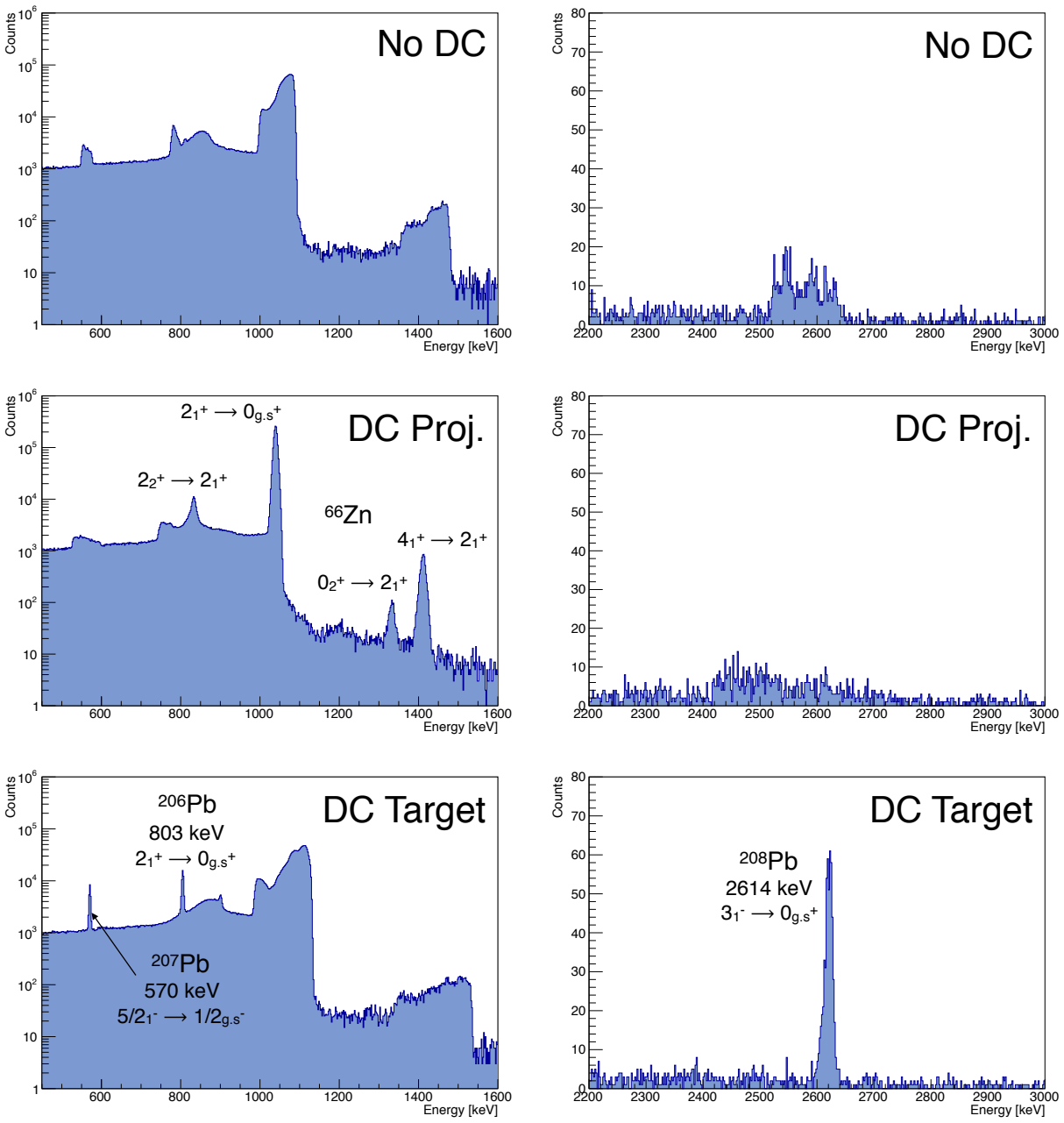

Figure 4.19: γ–ray energy spectra around 1 MeV and 2.5 MeV acquired in coincidence with the back-scattered ^{66}Zn ions. In the upper panels (No DC) no Doppler correction has been applied, in the middle panels (DC Proj.) the Doppler correction has been applied for the projectile nuclei while in the lower panels (DC Target) for the target nuclei. The spectra are not random background subtracted.

CHAPTER 5

SPIDER ANALYSIS

In this chapter the analysis of the SPIDER performances after its first use in the ^{66}Zn experiment is presented, in particular regarding radiation damage effects (section 5.1) and signal correlations (section 5.2). In the last section (5.3) the use of the acquired particle energy spectra to obtain information about the target composition will be described.

5.1 Radiation Damage

The effects of radiation damage in silicon detectors have been widely studied for high energy physics applications (see for instance [101], [102] and [103]). In these studies, the detectors were irradiated with protons, low-Z ions at relativistic energies or neutrons, with strong fluxes. The radiation damage induced by heavy ions has been studied for low-energy implantation during the detectors fabrication process (see for instance [104]). Only a few works are focused on typical low-energy nuclear physics conditions, i.e. the radiation damage effects induced by heavy ions with energies of $\sim 5 - 100$ MeV/A. The damage factor α is often considered as a probe of radiation damage, and it is defined as

$$\alpha = \frac{dJ}{d\Phi} \tag{5.1}$$

where J is the leakage current density (the leakage current divided by the damaged volume of the detector) and Φ is the irradiated flux impinging on the detector (the number of detected particles divided by the surface of the detector). Measurements of α for low-energy nuclear physics applications have been reported by S. Barlini *et al.* [105] and M. Kurokawa *et al.* [106].

The damage effects induced by heavy ions are due to their collisions with the silicon nuclei of the detector. The main contribution comes from the nuclear energy loss, while

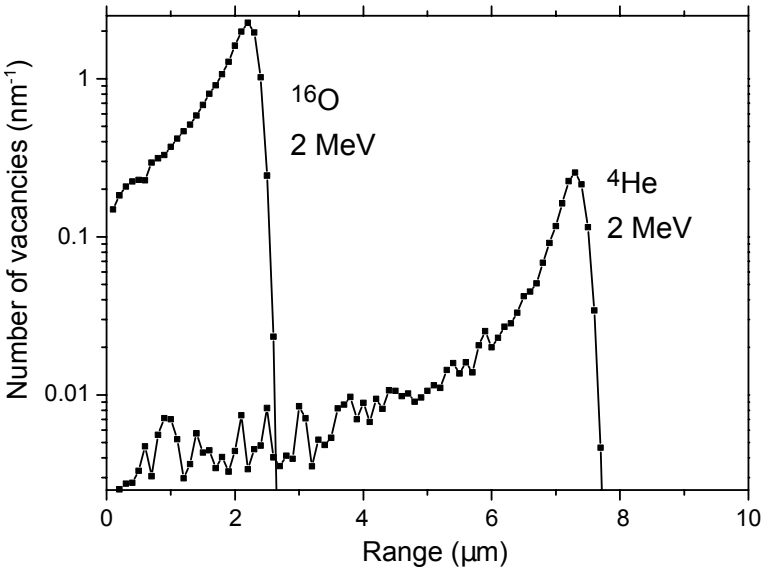

Figure 5.1: Depth distribution of the number of vacancies created by 2 MeV ^{4}He and ^{16}O ions in silicon according to SRIM calculations [84]. The figure is taken from [104]. It is visible how the vacancies are mainly produced at the end of the range.

effects due to the electronic energy loss are typically negligible. If the recoil energy of a silicon atom is sufficient to displace it from a normal site in the lattice, a vacancy is created in the crystal, which can also be permanent. The defects introduce energy levels within the forbidden energy gap and behave as recombination or generation centers of electron-hole pairs. Consequences of radiation damage are the increase of the leakage current and modification of the charge collection efficiency, which induces a decrease of the signal amplitude (corresponding to an energy shift in the acquired spectra), an increase of the signal risetime and a worsening of the energy resolution. In low-energy nuclear physics experiments, these effects can be already observed at fluxes less intense than the ones typical of high-energy physics experiments, due to the larger contribution of the nuclear stopping powers. When the ions are stopped inside the detector, they release all their energy and the damage is mainly localized in the last part of the range [106]. This is visible in figure 5.1, where it is shown how most of the vacancies are produced close to the Bragg peak [107]. A damaged layer is thus created over a width of few μm, located at a depth corresponding to the range of the impinging ions. These defects influence the signals produced by particles stopped in the damaged layer or in the region between this layer and the surface where the particles enter the detector [108].

In Coulomb excitation measurements the most important information obtained from the particle detector is the impact position. However, particle-energy spectra of high quality (i.e. stability and resolution), offer the possibility to get information about the

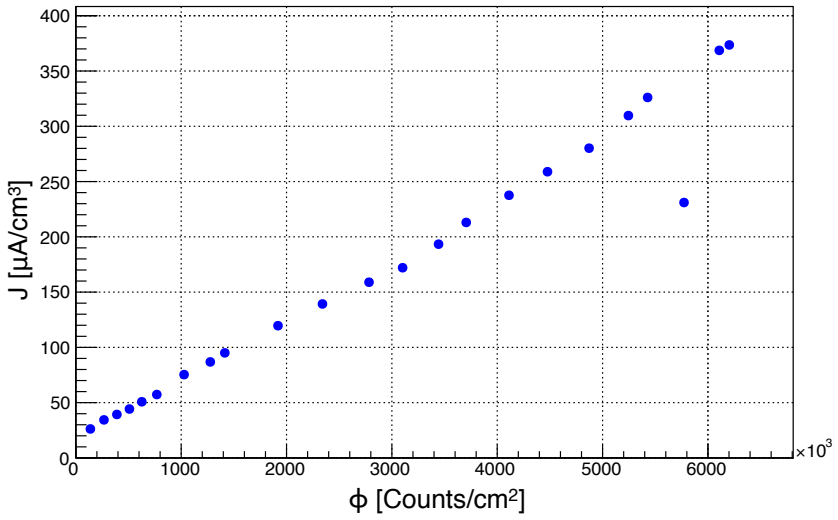

Figure 5.2: Leakage current density J as a function of the backscattered ^{66}Zn flux. The figure refers to the SPIDER strip D4S7 ($\theta = 125.5°$). The data points refer to the start of each partial run (the file in which data are stored changed every $2 - 4$ h).

target and beam properties, as will be shown in section 5.3. Moreover, when the particle detector is positioned at forward angles, the energy information can be used to distinguish the projectile and target recoils, on the basis of the scattering kinematics. Before every experiment, it is therefore necessary to estimate the radiation damage effects to properly choose the beam current. A compromise between the acquired statistics and the damage of the particle detector has to be found.

In figure 5.2 the leakage current density J is shown as a function of the flux Φ during the ^{66}Zn experiment, for one of the most irradiated SPIDER strips[1]. The approximate linear dependence of J on Φ is apparent. The value at $\Phi \sim 5.8 \cdot 10^6$ counts/cm^2 is lower, probably due to an error in the automatic procedure that reads the leakage current. From this plot, it is possible to extract the damage factor α, defined in equation 5.1. This value has been obtained for each SPIDER strip and is reported as a function of their center-of-mass polar angle in figure 5.3. The main error associated with the estimation of α comes from the uncertainty in the definition of the damage volume, which is obtained as the product of the SPIDER strips surfaces times the "last part" of the range. In the case of the present experiment the definition of the "last part" is not straightforward, first, because this value is different for different scattering angles, second, because, due to the energy loss of the beam inside the target, the detected ions have a large distribution (see figure 4.12). Moreover, the way in which this "last part" is defined in the literature is still

[1]The SPIDER strips were individually biased using Caen SY527 rack, A519 modules, ([109]) which provide an individual read-out of the leakage current of each strip.

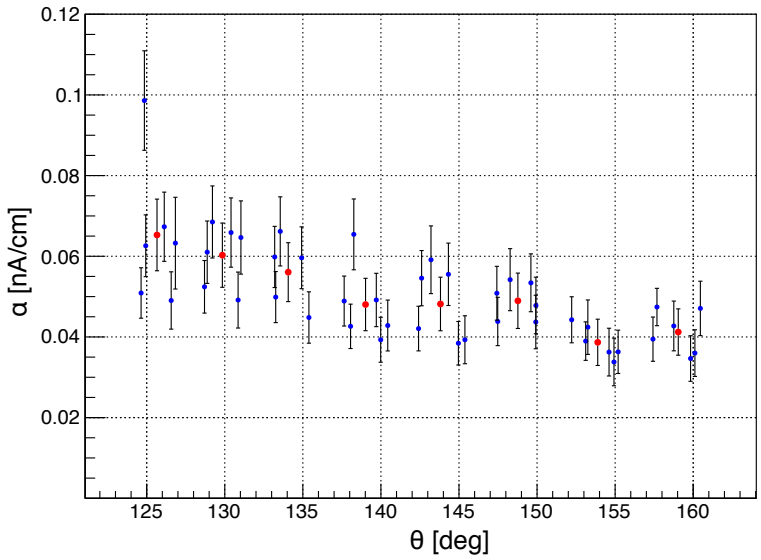

Figure 5.3: The damage factor α as a function of the center-of-mass polar angle of the SPIDER strips is reported in blue for each strip, a mean value for the strips of the same ring is shown in red. The theta angle is slightly different for strips in the same ring due to the imperfect centering of SPIDER inside the GALILEO vacuum chamber.

debated also for simpler cases [105]. From figure 5.3 it is visible how the damage factor decreases from a value of $6.5\,(9) \cdot 10^{-2}$ nA/cm down to a value of $4.1\,(6) \cdot 10^{-2}$ nA/cm (the rate at $\sim 125.5°$ is ~ 3 times larger than that at $\sim 158.5°$). The dependence of α on the impinging rate was suggested in [105] and seems to be here confirmed.

The present values of α is one order of magnitude larger than that found in [106]. In this work it was pointed out how the damage factor depends linearly on the Non-Ionizing Energy Loss (NIEL), which is essentially the nuclear stopping power. The authors provide an empirical expression to compare the damage factor for different ion species and impinging energies, and to predict its value on the basis of the nonionizing energy loss. In the same work the damage factor for ^{40}Ar nuclei impinging on a silicon detector with an energy of 20 MeV was measured, and the NIEL was calculated (NIEL $= 1.78 \cdot 10^2$ MeVcm^2/g) using the Lindhard-Scharff-Schiott (LSS) theory [111]. This value is very close to the one obtained for the ^{66}Zn ions scattered at $\sim 125.5°$ (NIEL $= 1.77 \cdot 10^2$ MeVcm^2/g), hence the damage factor should be comparable to the ones obtained in the present work, according to the conclusions of [106]. Actually, the value obtained for the ^{40}Ar nuclei is $\alpha = 4.9 \cdot 10^{-3}$ nA/cm, an order of magnitude smaller than the present value. The reason of the discrepancy can be due to the different experimental conditions: while in the work of [106] the energy of all the ions impinging on the detector was exactly 20 MeV, in the present work the ions have a large energy distribution due to the back-scattering and the energy loss in the target. As a consequence the damaged volume is

different: in the experiments described in [106] a single layer with a width of few μm was damaged, while several layers have been damaged during the ^{66}Zn experiment. For this reason a comparison with the results of ref. [106] may be misleading and the large value of α obtained in the present work may not correspond to a large radiation damage of SPIDER. To draw a conclusion it is therefore necessary to analyse if there are visible effects in the acquired energy spectra and signals.

5.1.1 Effects on Energy Spectra and Signal Shapes

Figure 5.4 shows a simulated energy spectrum of one SPIDER strip in the ^{66}Zn experimental conditions (red distribution). The SIMNRA code [110] has been used in the simulation. The shape of the energy distribution depends on several parameters, such as the center-of-mass polar angle of the considered strip, the solid angle subtended by it, the beam energy and intensity, the target composition and thickness and also the detector resolution and the target roughness. The width of the distribution ($E_s - E_r$ in the figure) is related to the target thickness. The ions that are scattered on the surface of the target (case s in the figure) do not lose energy into the target, thus their energy can be simply obtained using the kinematics equations described in section 2.3. Once the ions enter into the target (cases m and f in the figure), they lose energy, giving rise to the continuous distribution. By comparing the simulated spectrum with the one obtained in the same conditions for a thin target (shown in green in figure 5.4), it is possible to see that E_s

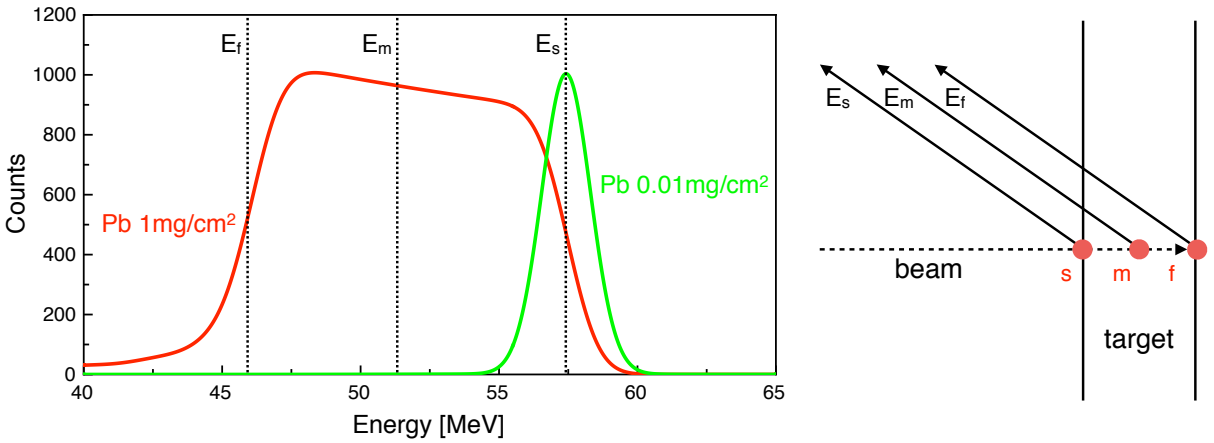

Figure 5.4: Left: a simulated energy spectrum for a SPIDER strip positioned at $\theta = 158.5°$ is shown in red, considering the real conditions of the ^{66}Zn experiment except for the target thickness, 1 mg/cm^2. The same spectrum, simulated for a thin target, is reported in green. Right: schematic view of three different impact position of the beam on the target.

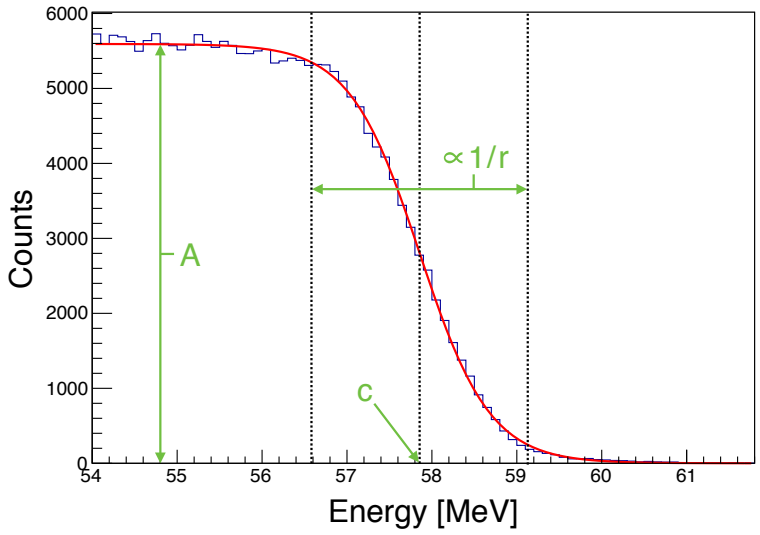

Figure 5.5: Example of fit procedure on an experimental particle spectra acquired by SPIDER, shown in blue. The fitted function (which is reported in equation 5.2) is shown in red, while its free parameters are reported in green.

roughly corresponds to the energy in which the height of the descendent part of the red spectrum is half of the maximum. This value can be obtained by a fit procedure using the empirical step function

$$f(E) = \frac{Ae^{cr}}{e^{cr} + e^{rE}} \tag{5.2}$$

where A is the height of the distribution, c is the half-height energy and $1/r$ is related to the step width (an example of fit is shown in figure 5.5). The width of the distribution associated with the thin target (green spectrum) is due to the finite SPIDER energy resolution, which can be estimated also from the thick target spectrum (the red one): as a first approximation, this corresponds to the ratio between the difference of the two energies at which the red spectrum height drops is 10% and 90% of the maximum (which can be obtained from the fitted r parameter) and E_s.

In figure 5.6, the comparison between the particle energy spectra acquired at the beginning and at the end of the experiment is shown, for one of the least (left) and one of the most (right) irradiated strip. In the case of the most irradiated strip, a shift of the energy distribution of ~ 1.3 MeV has been estimated. The width of the descending part of the spectrum increases up to 100 keV at the end of the experiment. For the least irradiated strip, the energy shift is 0.8 MeV and the width increases of 100 keV. The energy resolution is always well below 5%, also for the other strips, and the energy shift is about $\sim 1.8\%$ of the detected energy. These effects are negligible for the analysis of Coulomb excitation experiments and, in any case, can be corrected using the Doppler correction minimization procedure discussed in section 4.4.2.

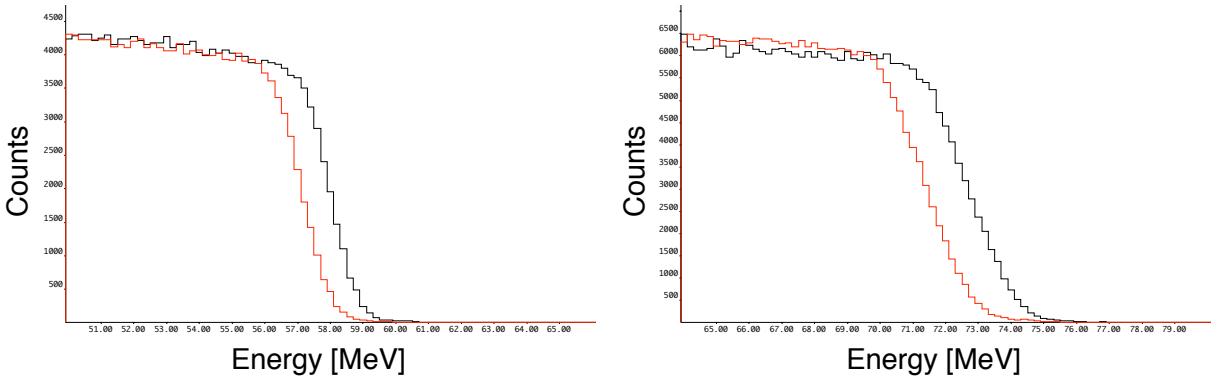

Figure 5.6: Left: particle energy spectra acquired by one of the less-irradiated SPIDER strip (D6S0 $\theta = 158.5°$). Right: the same for one of the most-irradiated SPIDER strip (D4S7, $\theta = 125.5°$). Spectra recorded at the beginning and at the end of the experiment are reported in black and red respectively.

Similar spectra have been acquired by positioning an α-source at the target location, before and immediately after the experiment. For one of the most irradiated strip, the energy resolution was 1.1% before the irradiation and 1.6% at the end (see figure 5.7). For one of the least irradiated strip the resolution was 1.0% before and 1.1% after. It should be noted, however, that the α-particles emitted by the source are stopped beyond the silicon layer that was damaged by ^{66}Zn ions. As already pointed out in [108], the damage effects are clearly visible only if the particles are stopped in the damaged layer or between the damaged layer and the front side of the detector surface. An attempt to add a degrader between the α-source and SPIDER was made, but the large energy straggling prevented a quantitative comparison.

The signal risetime is one of the most sensitive quantities to the radiation damage [105] and it has been checked before and after the measurement considering different strips. No appreciable changes have been observed, as shown in figure 5.8.

5.1.2 Conclusions

A spontaneous decrease of the reverse currents was observed two months after the experiment. For one of the most irradiated strips, the current decreased from ~ 2 μA to ~ 1 μA, confirming the self-annealing already pointed out in [105]. The large damage factor observed during the ^{66}Zn experiment seems not to correspond to a permanent radiation damage, since no relevant effects were observed during and after the experiment. The value of α can reflect the fact that in the present work a large damaged layer is produced inside SPIDER, while the damage factor reported in [106] was obtained considering a thinner layer.

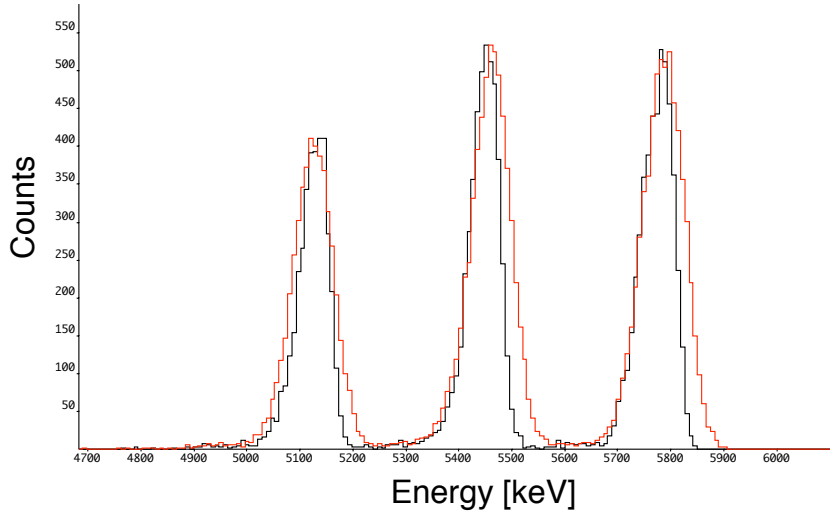

Figure 5.7: Comparison between the α-particle energy spectra acquired with an α-source in the target position. In black the energy spectrum before the ^{66}Zn experiment is shown, in red the same after the experiment. The same calibration has been used for the two spectra. One of the most irradiated SPIDER strip is considered (D4S7, $\theta = 125.5°$).

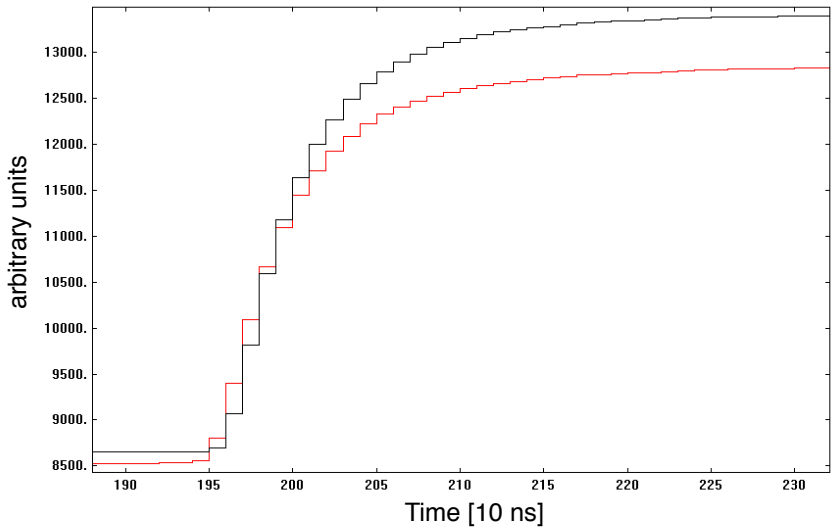

Figure 5.8: Comparison between the acquired signals at the beginning (black) and at the end (red) of the ^{66}Zn experiment. One of the most irradiated SPIDER strip is considered (D4S7, $\theta = 125.5°$).

The analysis has been also performed for the SPIDER commissioning at LABEC, where a beam of ^{7}Li was used. A value of $\alpha = 9 \cdot 10^{-7}$ nA/cm has been obtained, which is of the same order of magnitude of the values reported in [106] for protons. Also in that case no evidence of high radiation damage was found.

The hardness factor k has been calculated for the ^{66}Zn experiment. This is defined as

$$k = \frac{\int D(E)\,\phi(E)\,dE}{D(E_n = 1\text{ MeV}) \cdot \int \phi(E)\,dE} \tag{5.3}$$

where $\phi(E)$ is the energy spectrum and $D(E)$ is the displacement damage cross-section, which takes into account the cross-section of all possible energy loss modes not involving ionization and also effects due to recoiling target atoms [112]. The value $D(E_n = 1\text{ MeV})$ is the displacement damage cross-section for 1 MeV neutrons, equal to $D(E_n = 1\text{ MeV}) = 95\text{ MeV} \cdot \text{mb}$ [113]. In the ^{66}Zn experiment the k factor varies from $5 \cdot 10^4$ up to $6 \cdot 10^4$, depending on the scattering angle. This value allows the conversion from the particle flux Φ to the 1 MeV neutron equivalent flux Φ_{eq} (often used in the literature also for other radiation damage applications) through $\Phi_{eq} = k\Phi$. The obtained, final value of Φ_{eq} for one of the most irradiated strips is $\Phi_{eq} = 3 \cdot 10^{11}$, well below the inversion type limit of $\Phi_{eq} = 10^{13}$ [114].

The results obtained in this section can be used in order to optimize the beam current in future experiments using SPIDER. The ion flux Φ can be estimated from the calculated cross-section, the SPIDER geometry and the duration of the experiment. Assuming the value of α here obtained, and scaling the results, it will be possible to estimate the increase of leakage current, the particle energy shift and the worsening of the energy resolution.

5.2 Pulse-Height Correlation Matrices

Cross-talk and charge-sharing effects induced by α particles and light ions in DSSSD (Double-Sided Silicon Strip Detectors) were extensively analysed by L. Kaya *et al.* [115] and D. Torresi *et al.* [116]. In these works was pointed out how these effects are well visible already using low-Z and low energy particles. Each SPIDER detector is segmented in 8 independent strips; however, the segmentation process differs from the one used in DSSSDs, and the presence of the guard ring should in principle reduce cross-talk and charge-sharing effects.

Single SPIDER strips were irradiated by α particles emitted by an ^{241}Am α-source, while the others were screened by a thick aluminium foil. No evidence of cross-talk and charge-sharing was observed [117]. The same conclusions were drawn during the ^{7}Li commissioning experiment described in section 3.2.2. In that case, the acquisition system

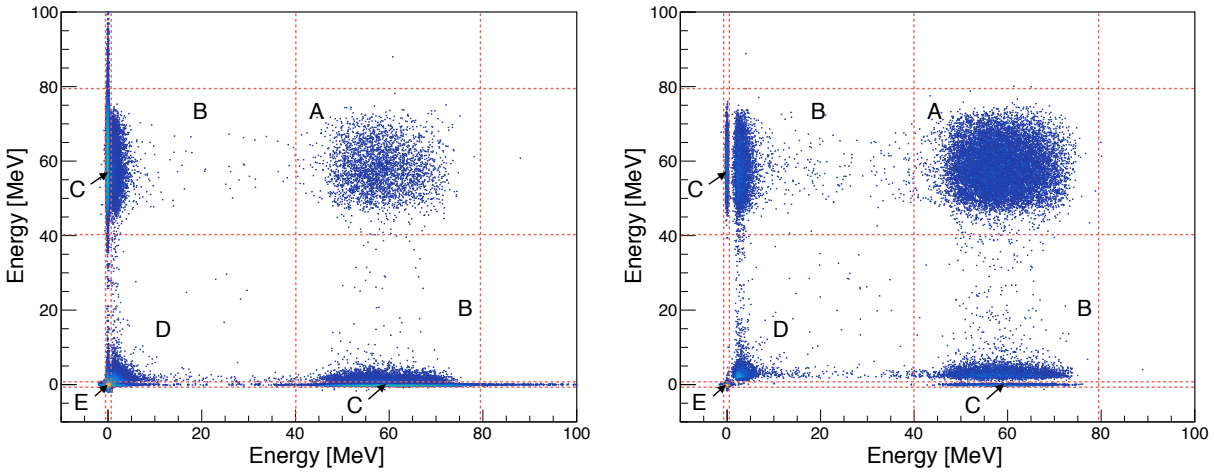

Figure 5.9: Pulse-height correlation matrices, relative to particle-particle coincidences considering the entire SPIDER array. Left: matrix obtained with low energy thresholds. Right: corresponding matrix with increased energy thresholds. The regions with the larger number of counts are labelled from A to E. The matrices refer to different acquisition times and mean beam currents, in particular, the matrix on the right shows twice the statistics of the one on the left.

allowed the on-line counting of double-hit events, which resulted to be negligible with respect to the total statistics.

Obviously, when heavy ions are detected, the SPIDER behaviour may be rather different: in that case much more energy is released inside each strip, corresponding to signals of higher amplitude that can induce cross-talk or charge-sharing not observed in the α-source or ^{7}Li measurements. During the first hours of the ^{66}Zn experiment, the energy thresholds of SPIDER were kept as low as possible (few keV) in order to study these effects.

Two pulse-height correlation matrices, relative to the entire SPIDER, are shown in figure 5.9. The energy extracted from the acquired signals is reported in the matrices, only if two or more signals are in time coincidence. The left panel of the figure corresponds to the first part of the ^{66}Zn experiment, in which the energy thresholds of the SPIDER strips were kept low. The right panel corresponds to the same matrix with increased energy thresholds ($2-3$ MeV). The regions with the larger number of counts are labelled from A to E. All the events in the matrices correspond to multiplicity 2 (or higher) events (excluded in the final coincidence selection using the multiplicity filter described in section 4.3.2). The left matrix corresponds to $\sim$ 12 hours of measurement, while the right one to $\sim$ 2 days. To facilitate the comparison, the number of counts of each region is normalized to the total acquired statistics (which includes also events with multiplicity

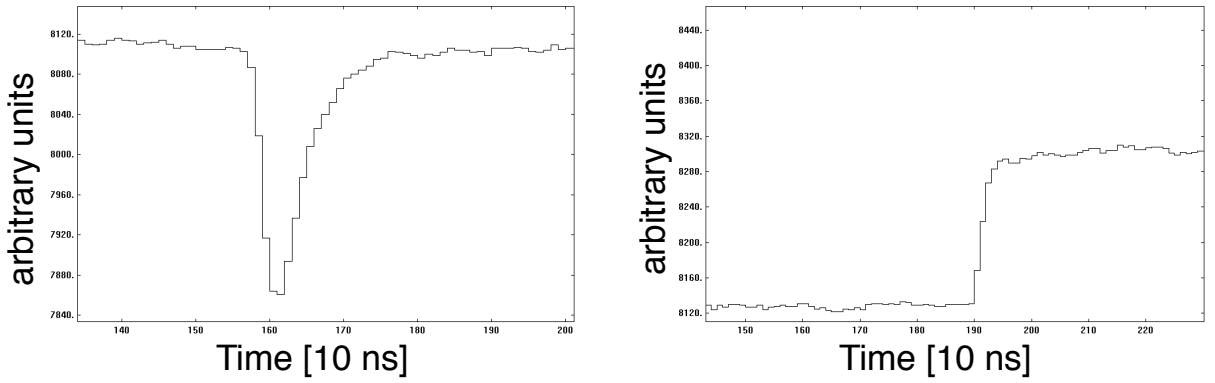

Figure 5.10: Examples of negative polarity (left) and noise or cross-talk signals (right) acquired during the ^{66}Zn experiment. A comparison with signals corresponding to backscattered ^{66}Zn ions can be made considering figure 5.8.

one, i.e. ions diffused through Coulomb excitation and elastic scattering) in the following. Region A corresponds to double hits events, in which 2 different particles are detected by two different SPIDER strips. These events are extremely rare, and correspond to $\sim 0.2‰$ of the total statistics (the same value is obtained with both low and high energy thresholds). Regions B and C correspond to events in which a particle is detected in one strip in time coincidence with a low-energy signal of a different strip. Region C (energy ~ 0 MeV) shows a higher number of counts than region B. In DSSSD detectors it was observed that signals of reverse polarity can be induced by the impinging particle in adjacent strips/rings of the detector ([115, 116, 118, 119]). A similar effect may occur also in SPIDER, where negative polarity signals were clearly observed (see figure 5.10 left). The employed digitizers are only able to read out positive polarity signals; however negative polarity signals can still be acquired (due to baseline fluctuations as described in [115]) as very-low-amplitude signals (region C). Low amplitude signals can also be produced by cross-talk (see figure 5.10 right). In this case, a positive polarity is expected, with an amplitude that increases when the ion impinges close to the boundaries of the strip. Cross-talk and negative signals can be, in principle, included in the regions B and C. However, an analysis of the single traces that have been acquired proved that the main contribution to the region C comes from the negative polarity signals. Region D and E can be related to events in which noise, cross-talk and negative polarity signals are in coincidence, these being the main contribution from coincidences between negative polarity signals. These events are rather common because when an ion is detected in one strip all the others register a negative polarity signal.

The matrices shown in 5.9 have been produced also for single combinations of two SPIDER strips, considering a time coincidence with a single strip in which only scattered

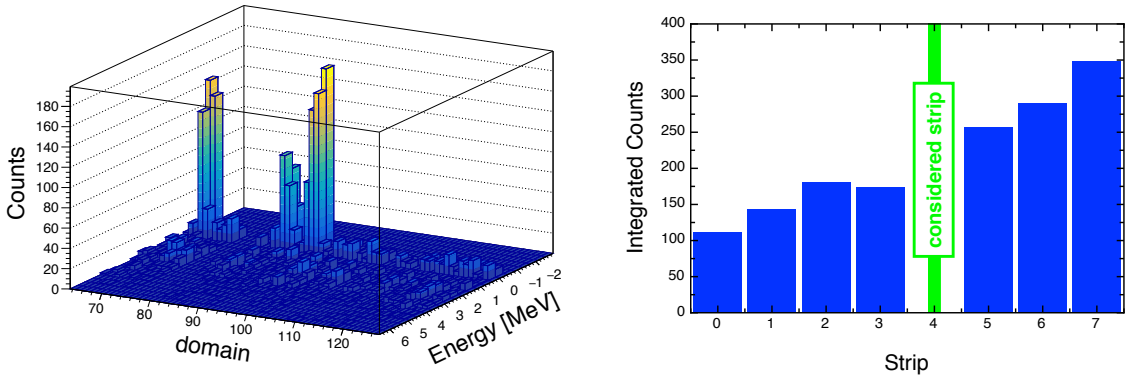

Figure 5.11: Left: number of counts registered in the SPIDER strips as a function of the energy and of the domain number. The events are obtained requiring a time coincidence with a given strip (D2S4), in which only scattered ^{66}Zn ions have been selected. Right: the integrals over the low-energy region ($0 - 2$ MeV) of the left figure are reported for the detector D2.

^{66}Zn ions have been selected. In figure 5.11 (left) is reported the number of counts registered in the SPIDER strips as a function of the energy (in the region close to 0 MeV) and of the domain number (which identify the SPIDER strips). The results show how the detected ions in a given strip are in coincidence mostly with signals with very low energy, coming from the same detector. In figure 5.11 (right) is also shown how the number of counts increases from strip 0 to strip 7. This fact suggests a correlation with the dimensions of the strips or with the scattering angle. This analysis has been repeated for the other SPIDER strips, obtaining similar results.

The total number of counts of the matrix reported in the left panel of figure 5.9 corresponds to 23% of the total statistics. Most of these events are located in the regions C and E (21.5%). The events in the region E have no physical meaning and are rejected by the multiplicity filter. The events in region C, corresponding to an ion detected in a SPIDER strip and a negative polarity signal in a different strip, are also rejected. In order to recover these events, and thus not loose statistics, the multiplicity filter has been modified to take into account the energy of the signals. In figure 5.12, the three possible types of events under discussion are shown. As already discussed in section 4.3.2, the multiplicity filter requires 1 γ–ray and 1 particle in order to select the real Coulomb excitation coincidence (type 1 in figure 5.12). Adding a condition on the energy detected in SPIDER for the second signal, type 2 events can be retained while type 3, for which it is impossible to obtain the impact position, are rejected.

The energy condition in the multiplicity filter has been necessary only for the data acquired with low-energy thresholds for SPIDER. The total number of counts for the

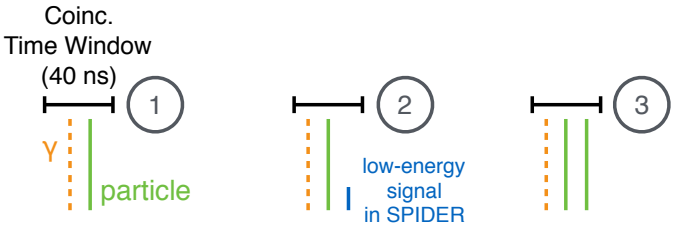

Figure 5.12: Possible acquired events considering the energy registered in the SPIDER strips: 1) real coincidence, 2) real coincidence with a low-amplitude signal, 3) true double hit event.

events in the right matrix shown in figure 5.11 (corresponding to the case in which the thresholds were increased), is only $\sim 0.7‰$ of the total statistics. The importance of the guard ring is here confirmed, showing how cross-talk events are less than 1% of the total statistics, while charge splitting events (which should lie on a diagonal connecting the two regions B) are completely absent. The origin of the negative polarity signals will be further investigated; however, thanks to the energy-dependent multiplicity filter, all the effects discussed in this section are under control without any loss of statistics.

5.3 Particle Energy Spectra

The energy calibration of the particle spectra acquired using SPIDER has been described in section 4.2.1. During the experiment an in-beam calibration was performed using the elastic scattering of the ^{66}Zn beam on two different targets, ^{208}Pb and ^{124}Sn. The channel number corresponding to the energy of the ions that had been elastically scattered on the target surface was obtained by a fit procedure to the experimental, non-calibrated, spectra, using the function 5.2. The corresponding energy was calculated using equation 2.43. Figure 5.13 reproduces figure 4.7 with the addition of these two new calibration points. A disagreement with the previous calibration is visible: the energy of the ^{66}Zn ions is clearly overestimated by ~ 10 MeV in the case of ^{208}Pb, while the difference for the ^{124}Sn target is ~ 5 MeV. The discrepancy holds for all the SPIDER strips.

As explained in sections 4.4.2 and 4.4.3, particular attention has been given to the energy calibration of SPIDER, performing several checks based on the minimization of the Doppler effect. The offsets needed to correct the energy calibration have negative signs and absolute values do not exceed the 4 MeV. To check the possibility of an error in the determination of the polar angles of the SPIDER strips, the Doppler effect minimization procedure of section 4.4.1 has been also applied to the GALILEO HPGe polar angles, which are known with high precision. The angles were reproduced with an error of about

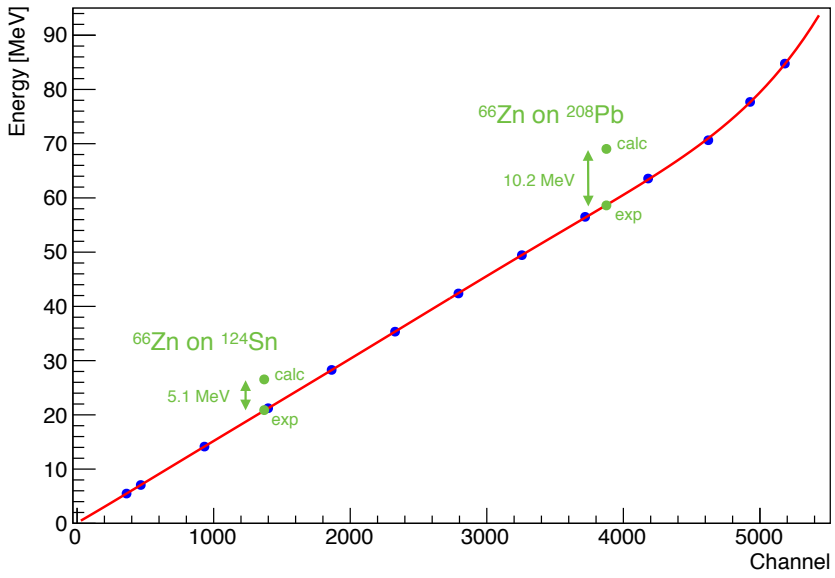

Figure 5.13: The same plot as reported in figure 4.7, with the addition of two points associated to the scattering of the ^{66}Zn beam on the ^{124}Sn and ^{208}Pb target front surfaces. The discrepancy between the calculated energies, obtained thorough the equation 2.43, and the detected ones, obtained from the calibration described in 4.2.1, is also shown.

one degree[2].

Other effects such as pulse-height defect ([120], [121]), or second-order corrections to the Rutherford orbits [77] are estimated to produce an energy decrease much smaller than 10 MeV (less than $1-2$ MeV). The fact that the two independent energy measurements that have been made, one using the Doppler correction minimization (section 4.4.3) and one using the energy registered in SPIDER, are comparable within an error of about ~ 1 MeV, indicates that the discrepancy could not be due to the detection system.

It follows that the discrepancy can only be ascribed to the target or beam characteristics. A beam energy lower than the requested one could in principle explain the discrepancy. Considering the elastic scattering, it is possible to express the beam energy from 2.43 as

$$E_{beam} = \frac{E'_P}{\left(\frac{m_T}{m_P+m_T}\right)^2 \left(1+\frac{m_P^2}{m_T^2}+2\frac{m_P}{m_T}\cos\theta^P_{CM}\right)} \tag{5.4}$$

where

$$\theta^P_{CM} = 2\arctan\frac{\cos\theta^P_{lab} - \sqrt{1-\frac{m_P^2}{m_T^2}\sin^2\theta^P_{lab}}}{\left(\frac{m_P}{m_T}-1\right)\sin\theta^P_{lab}} \tag{5.5}$$

[2]It should be noted that the minimum possible scattered energy, calculated from the kinematics of the present experiment in head-on collisions at 180°, is 64.5 MeV.

A procedure to obtain a precise estimation of E_{beam} using the different combinations of E'_P and θ^P_{lab} given by the SPIDER strips has been implemented in the sorting codes considering the case $E'_P = E_s$ (with reference to figure 5.4). Including also the calibration offsets obtained from the Doppler effect minimization, the value of $E_{beam} = 213.8\,(5)$ MeV is obtained at the beginning of the experiment. This value decreases to $E_{beam} = 210.2\,(5)$ MeV at the end of the experiment. When considering scattering on ^{124}Sn (used at the end of the measurement) the calculated value is $E_{beam} = 228.2\,(8)$ MeV. The beams provided by the LNL Tandem-XTU accelerator have very precise energy and high stability. All the parameters of the magnetic optics used for the beam transportation are saved by an automatic system and confirm the requested energy $E_{beam} = 240$ MeV. The discrepancy, thus, should be ascribed to another effect.

5.3.1 Target Contaminants

In γ–ray energy spectra acquired without particle coincidences, transitions related to ^{76}Kr have been clearly identified. In figure 5.14 its ground state band is shown on the right, while on the left the spectrum obtained by projecting the sorted γ-γ matrix, with a gate on the $2^+_1 \longrightarrow 0^+_{g.s}$ transition, is reported. The ^{76}Kr nuclei can be produced by the fusion-evaporation reaction ^{12}C(^{66}Zn,2n)^{76}Kr with a cross-section $\sigma \sim 200$ mb (calculated using the PACE4 code [122]). γ–rays from ^{76}Br (evaporation channel 1n1p) are also

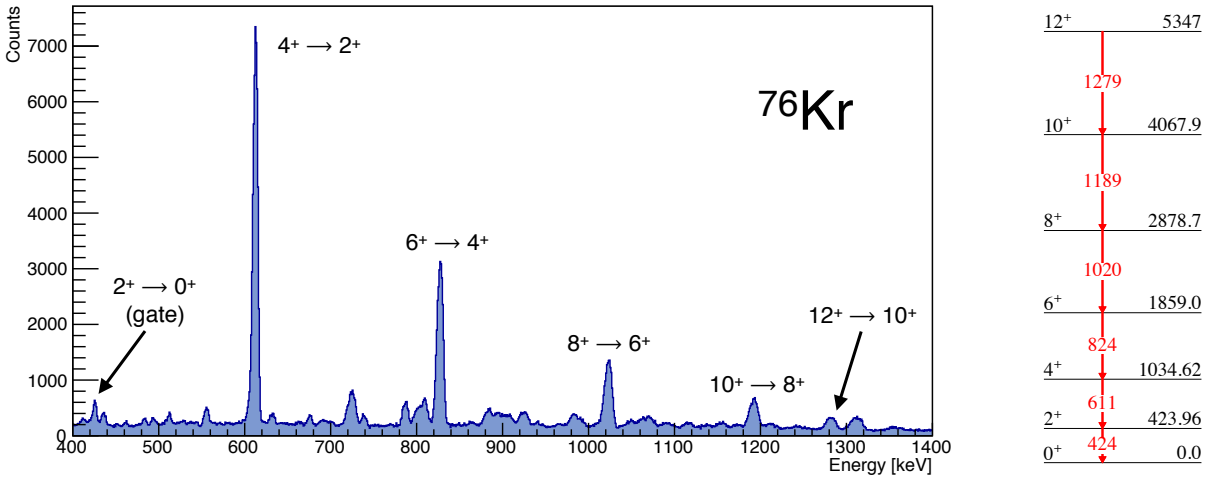

Figure 5.14: The γ–ray spectrum obtained by projecting the γ-γ matrix with a gate on the $2^+_1 \longrightarrow 0^+_{g.s}$ in ^{76}Kr. A rough Doppler correction, assuming that all the produced ^{76}Kr are emitted in the forward direction, is applied. The coincidence transition up to spin 12^+ are visible. Other transitions, not associated from ^{76}Kr, are present due to the fact that the spectrum is not background-subtracted. The decay scheme on the right has been taken from [100].

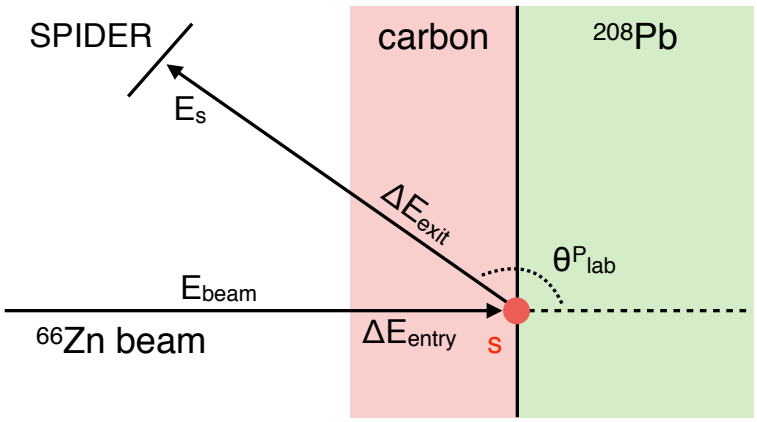

Figure 5.15: Schematic picture of the build-up carbon layer effect on the particle energy detected by the SPIDER strips. The carbon layer is indicated in red, while the lead target is indicated in green. The two energy losses, the one before (ΔE_{entry}) and the one after the scattering (ΔE_{exit}) in the lead surface are indicated.

present in the acquired data. The presence of transitions associated to the reaction of ^{66}Zn on ^{12}C suggests a target contamination.

Oxygen and carbon contaminants are commonly found in targets used for nuclear physics experiments. While the former is typically diffused inside the target, with a depth that depends on the duration of its exposure to air, carbon is deposited on its surfaces. The plastic 3D printed prototype of the frame, which was used during the ^{66}Zn experiment, is mainly composed of hydrocarbons. Moreover, these molecules are present in cables, PCB connectors and vacuum pumps oils. The so-called carbon build-up process, which induces the deposition of carbon on the target, has been widely investigated in the literature [123, 124]. In this process, carbon is deposited on the two surfaces of the target, the one which is irradiated and the opposite, with a thickness that increases during the irradiation. If a carbon layer is present on the target surface, the beam ions have to cross it before reaching the target surface, and, after the collision with a target nucleus, they have to cross the same layer before reaching SPIDER (see figure 5.15).

Carbon cannot be directly observed in the SPIDER energy spectra at backward angles. However, knowing the direction θ^P_{lab} and the energy E'_P of the back-scattered beam ions, and the beam energy E_{beam}, it is possible to obtain a precise estimate of the carbon layer thickness t, which can be expressed as

$$t = \frac{xE_{beam} - E'_P}{x\left(\frac{\Delta E}{\Delta t}\right)_{entry} + \frac{1}{\cos\left(\pi - \theta^P_{lab}\right)}\left(\frac{\Delta E}{\Delta t}\right)_{exit}} \tag{5.6}$$

where $\Delta E/\Delta t$ are the stopping powers of the beam at the entry and at the exit of the

investigated layer (figure 5.15) and

$$x = \left(\frac{m_T}{m_P + m_T}\right)^2 \left(1 + \frac{m_P^2}{m_T^2} + 2\frac{m_P}{m_T}\cos\theta_{CM}^P\right) \tag{5.7}$$

with θ_{CM}^P given by 5.5. It is possible to obtain a precise measurement of t using different combinations of $E'_P = E_s$ and θ_{lab}^P given by the several SPIDER strips. Also in this case, the offsets from the Doppler effect minimization procedure have been added to E'_P. The stopping powers are initially considered relative to the energy at the entry of the layer and at the exit. After a first estimation of the thickness a second iteration is made considering the values at half thickness of the layer, and again this procedure is repeated up to a convergence (another iteration is sufficient). It is also possible to integrate the stopping powers along the target thickness, but in the ^{66}Zn case this is not crucial since the values are almost constant. The obtained carbon thickness is $t\,(^{12}\mathrm{C}) = 0.120(7)$ mg/cm^2 at the beginning of the experiment and increase up to $t\,(^{12}\mathrm{C}) = 0.138(8)$ mg/cm^2 at the end[3]. This increase is in agreement with what was observed for instance in [123].

The carbon layer produces a decrease of the beam energy that has to be taken into account in the final Coulomb excitation analysis. Assuming a mean thickness of the carbon layer of $\bar{t}\,(^{12}\mathrm{C}) = 0.129(10)$ mg/cm^2, the beam energy at the entrance of the ^{208}Pb target can be calculated as $\bar{E}_{beam} \sim 235$ MeV.

5.3.2 Target Thickness

In the previous discussion, only the scattering on the target surface has been considered, to simplify the calculations that must be performed when all the SPIDER strips are considered. However, an analysis of the full energy spectra can provide more informations, such as a precise measurement of the target thickness using the RBS technique. The acquired particle spectra can be fitted by means of RBS analysis software, such as the SIMNRA code [110], as shown in figure 5.16 for one of the SPIDER strips (the data correspond to ~ 1 h of measurement). In the fit procedure the energy calibration and offsets obtained from the Doppler effect minimization have been included as fixed parameters. The carbon layer thickness has been also included. The height of the spectrum depends on the product of the beam current, the acquisition time, the cross-section and the solid angles subtended by each strip. All these quantities are known with high accuracy, with the exception of the beam current. The solid angles covered by the SPIDER strips can be calculated using the geometry described in figure 3.8, which includes the misalign-

[3] A built-up carbon layer on the target was observed also in a Coulomb excitation measurement performed at the Heavy Ion Laboratory (HIL) in Warsaw. In an independent Rutherford BackScattering (RBS) measurement, a carbon thickness $t\,(^{12}\mathrm{C}) = 0.12$ mg/cm^2 was assessed [125, 126]

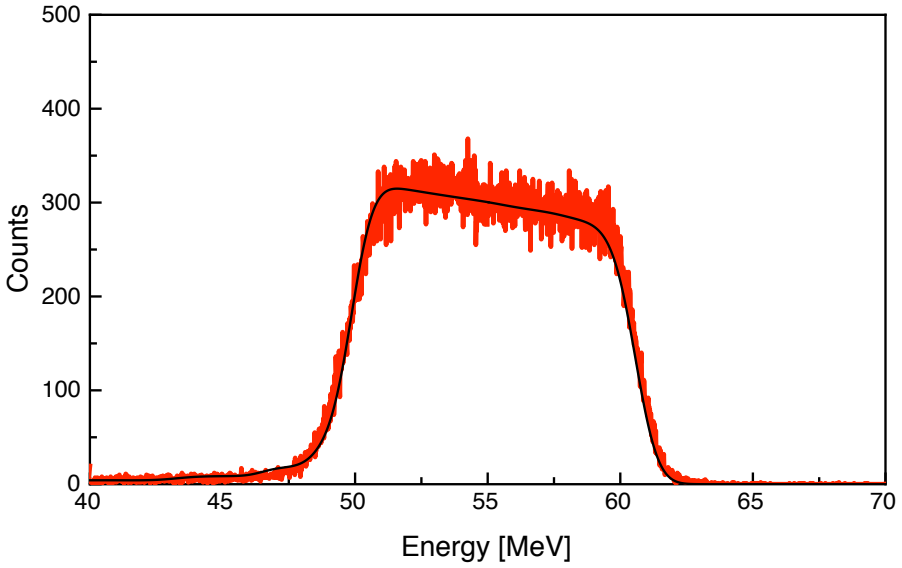

Figure 5.16: Experimental particle spectrum acquired by one of the SPIDER strips (red) analysed with the SIMNRA code [110] (the result is shown in black). The tail at low-energy is due to the target roughness.

ment with the beam axis, and the cross-section can be calculated assuming pure elastic scattering. The acquisition time is known with the precision of the timestamp ($\sim$ 10 ns) and the dead time is negligible due to the low counting rate. However, for the target thickness estimation, the height of the spectra can be treated as a free parameter. The thickness of the ^{208}Pb target, over different measurement periods, has been obtained and it is remarkably similar when different strips are considered: $t\,(^{208}\mathrm{Pb}) = 0.67(3)$ mg/cm^2. This value remains constant during all the experiment, proving no target deterioration.

5.3.3 RBS Measurement at LABEC

An independent measurement of the target was performed at the LABEC laboratory, in order to confirm the presence of the carbon layer and the ^{208}Pb target thickness. In figure 5.17 is shown a picture of the target taken at the end of the experiment. Three different regions are clearly visible: the one that was irradiated with the ^{66}Zn beam (black beam spot, numbered as 1), the region with no irradiation signs (numbered as 3) and a brown, annular region in between them (numbered as 2).

An RBS measurement was performed at the LABEC laboratory using a proton beam at an energy of 2 MeV. Three silicon detectors were used in order to detect the backscattered protons that impinged on the target. This was mounted on a rotating wheel that gives the opportunity of changing and positioning the target without breaking the vacuum (see figure 5.18). Using a fluorescent SiO target it was possible to focus the beam spot with

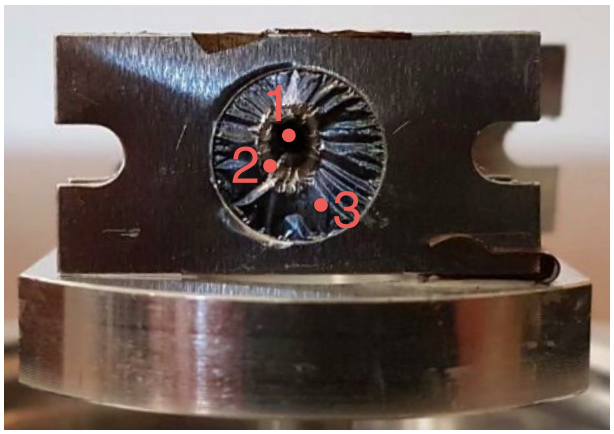

Figure 5.17: Picture of the ^{208}Pb target taken at the end of the experiment (the diameter of the hole in the aluminium frame is 1 cm). Three different regions are clearly visible.

a precision of 1 mm, appropriate to study the three different regions. For comparison, a spare ^{208}Pb target, never irradiated, was also measured. In figure 5.19 the different spectra obtained with one of the used silicon detectors are shown. The energy spectrum relative to the region 3 of the irradiated target is very similar to the one relative to the non-irradiated target, dominated by the ^{208}Pb contribution. The measured thickness is $\bar{t}\,(^{208}\mathrm{Pb}) = 0.65(5)$ mg/cm^2. Other 4 small peaks are visible in the spectra, associated to carbon and oxygen contaminations on both the two target surfaces. Moving the beam on region 2, the amount of oxygen increases. The corresponding peak has a width comparable to that of the lead peak, indicating that the two elements have a similar thickness. Therefore, the oxygen is diffused in the whole lead target. The spectrum relative to region 1 shows, besides the oxygen peak, two carbon peaks clearly enhanced with respect to region 2 and 3. The lead thickness is the same in all the three regions, while the measured carbon thickness in region 1 is $\bar{t}\,(^{12}\mathrm{C}) = 0.020(16)$ mg/cm^2 and negligible elsewhere.

The results of the RBS measurement support the hypothesis of a Carbon built-up layer on the surfaces of the beam spot, in agreement with what was already observed in other experiments [124]. Oxidation seems to be present in both the beam spot region (1) and in the region immediately close to this (region 2). The thickness of the carbon layer results in a factor of 6 less with respect to the one measured using SPIDER. This discrepancy could be explained taking into account that temperature effects are crucial in the build-up process [124]. The carbon is deposited in an equilibrium phase between the increase, due to the irradiation, and the decrease, due to the evaporation induced by the target heat increasing. The measurement at LABEC was performed about one year after the ^{66}Zn experiment. During that time the target was stored in a close box not in vacuum, and exposed to different temperature regimes. Thus, the decrease of the amount

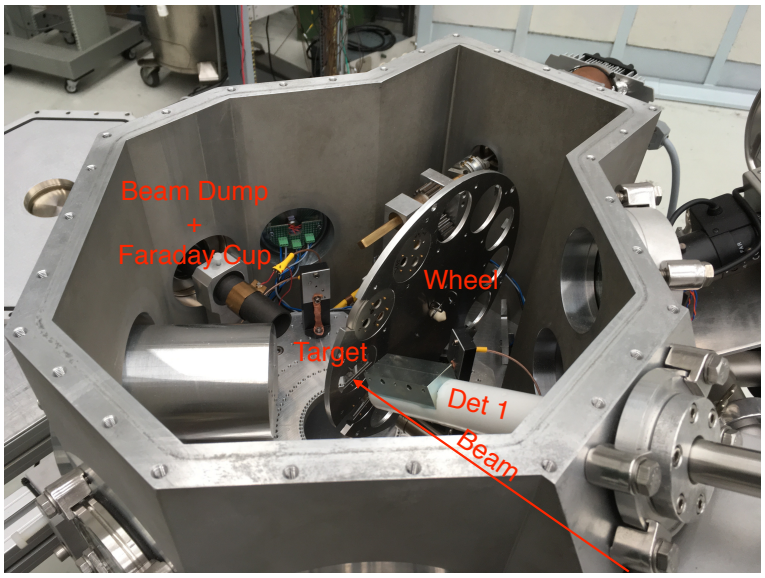

Figure 5.18: Picture of the setup used for the RBS measurement of the ^{208}Pb target. One of the used silicon detectors is visible.

of carbon can be due to the different conditions between the two measurements.

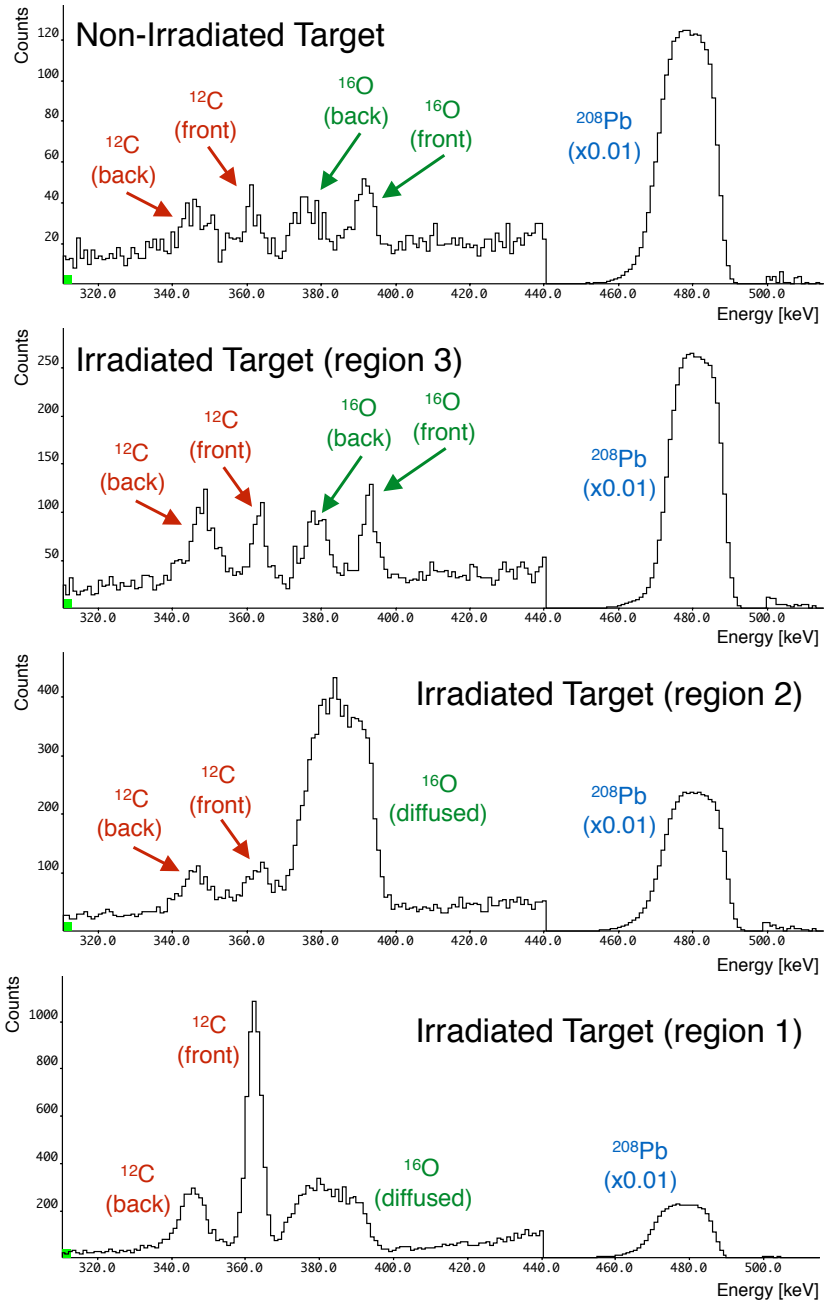

Figure 5.19: Energy spectra acquired by one of the used silicon detectors in the target RBS measurement at LABEC. The irradiated region and the different components are indicated. A portion of the spectra close to the ^{208}Pb region has been reduced by a factor of 10^2, in order to make an easier comparison. Region 1), 2), 3) of the irradiated target are relative to figure 5.17. The measurements of the irradiated target show twice the statistics of the ones relative to the non-irradiated one.

CHAPTER 6

COULOMB EXCITATION ANALYSIS

In this chapter, the Coulomb excitation analysis performed using the GOSIA code is presented, describing how $B(E2)$ and Q_s values have been extracted from the acquired data (section 6.1). The quadrupole sum rule method has been also applied, to study the deformation of the ^{66}Zn 0_1^+ and 0_2^+ states. The obtained values are then compared with previously results available in the literature (section 6.2) and state-of-the-art shell model and "beyond mean field" calculations (section 6.3).

6.1 The GOSIA Code Analysis

The total γ–ray energy spectrum acquired by GALILEO, in coincidence with the backscattered ^{66}Zn ions detected by SPIDER, is shown in figure 6.1. The observed transitions associated to ^{66}Zn are indicated, together with peaks related to the target and its contaminants. Direct and two-step excitation of the 2_1^+, 4_1^+, 0_2^+, 2_2^+, 2_3^+ and 3_1^- states of ^{66}Zn have been achieved (cfr. the level scheme in figure 1.10). The number of counts observed for the $2_1^+ \longrightarrow 0_1^+$, $4_1^+ \longrightarrow 2_1^+$, $2_2^+ \longrightarrow 2_1^+$ and $0_2^+ \longrightarrow 2_1^+$ transitions is sufficient to divide the statistics into eight different scattering angle ranges, using the full segmentation of SPIDER. For the $2_3^+ \longrightarrow 2_1^+$, $2_2^+ \longrightarrow 0_1^+$, $3_1^- \longrightarrow 2_1^+$ transitions it is still possible to divide the statistics into two scattering angle ranges. Considering all the subdivisions, 38 experimental yields have been obtained, to be used in the GOSIA analysis.

The energy of the $2_3^+ \longrightarrow 2_1^+$ transition is equal to 1741 keV, and it is very close to the ones of the $\left(6_1^+\right) \longrightarrow 4_1^+$ (1733 keV) and $4_2^+ \longrightarrow 2_1^+$ (1726 keV) transitions. Due to the resolution achievable with the GALILEO and SPIDER setup, and the low statistics, it is not possible to discriminate these transitions, therefore, a simulation has been performed with the GOSIA code in order to disentangle their contribution to the peak at $\sim$ 1735 keV.

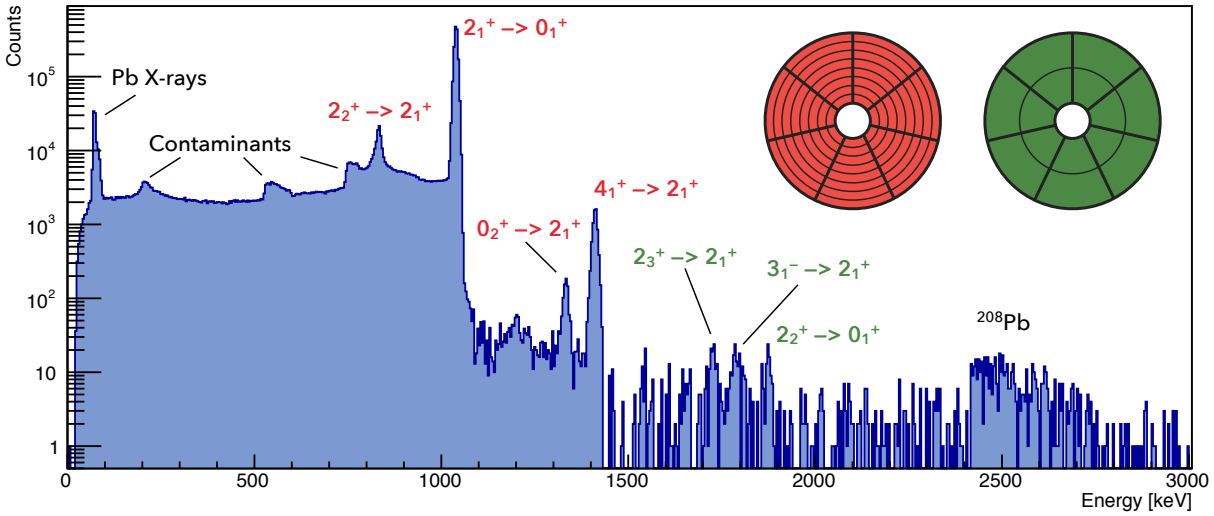

Figure 6.1: Total γ–ray energy spectrum acquired by GALILEO, in coincidence with the back-scattered ^{66}Zn ions detected by SPIDER. The spectrum is random-background subtracted and the Doppler correction has been applied for ^{66}Zn nuclei. The peaks corresponding to the observed transitions are indicated (cfr. figure 1.10). The total number of counts of the red transitions has been divided into eight different angular ranges, exploiting the full segmentation of SPIDER. Since the number of counts of the transitions indicated in green is relatively low, only two different scattering ranges have been considered (see the schematic picture of SPIDER on top right).

In the simulation, the transition probabilities of the NNDC database [100] have been used, referring to the level scheme reported in figure 1.10. When more than one value of transition probability is reported for the same transition ($4_1^+ \longrightarrow 2_1^+$ and $2_2^+ \longrightarrow 2_1^+$, see figure 1.9), different combinations have been considered. When only upper limits were available (transitions de-exciting the 4_2^+ and 0_2^+ states), both the limit and half of its value have been considered in the calculations, different combinations have been evaluated also in this case. The results of these simulations show how the number of detected γ–rays for the $2_3^+ \longrightarrow 2_1^+$ transition is, at least, two orders of magnitude larger than the number detected for the $4_2^+ \longrightarrow 2_1^+$ transition, and four orders of magnitude larger than that detected for the $\left(6_1^+\right) \longrightarrow 4_1^+$ transition. The same calculation has been repeated also with the matrix elements obtained in the final analysis, achieving the same result. This conclusion can be qualitatively explained by the fact that the 2_3^+ state can be reached by a single step $E2$ transition from the ground state, while the 4_2^+ and $\left(6_1^+\right)$ states can be populated only by two step and three step $E2$ excitation, respectively (as already discussed $E4$ excitations can be considered negligible in the present case). The number of γ–rays observed in the peak at ~ 1735 keV has been thus associated only to the $2_3^+ \longrightarrow 2_1^+$

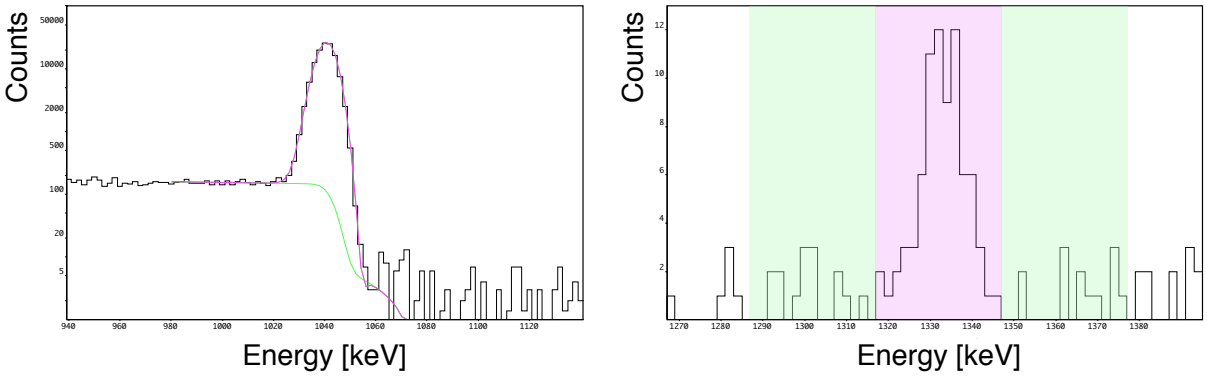

Figure 6.2: Two examples of number of counts estimation for the $2_1^+ \longrightarrow 0_1^+$ (left) and $0_2^+ \longrightarrow 2_1^+$ (right) transitions (the spectra refers to a single SPIDER scattering angle range). Left: a Gaussian function convoluted with an exponential function on the left side of the peak has been used (shown in purple). The background has been estimated with a step function (shown in green). Right: only an integral has been performed, in purple is shown the region of integration and in green the background regions (each of them has been divided by two in order to normalize to the same energy range).

transition.

The number of counts relative to each transition has been extracted from the experimental spectra using three different procedures. In the high statistics cases (see for instance the $2_1^+ \longrightarrow 0_1^+$ transition in figure 6.2, left panel) the number of counts was obtained by a fit procedure performed using the ProecmX [127] and TKT [128] software. The peaks in the spectra were fitted by Gaussian functions, with the possibility to include several options, such as a left tail (typical for neutron-damaged HPGe detectors) and different shapes for the background (linear, parabolic and step). A bare integral (i.e. the sum of the counts in each channel of the peak) has been also performed. In this case, a linear background estimated considering two regions, on the left and on the right of the peak, is subtracted from the integral. The three estimations (ProecmX, TKT and integral) gave very similar results, well within their errors. When the number of counts in the peak was low (for instance for the $0_2^+ \longrightarrow 2_1^+$ transition shown in figure 6.2, right panel) only the integral estimation (with background subtraction) was performed.

The level scheme considered in the GOSIA analysis is shown in figure 6.3. In order to correctly reproduce the excitation and de-excitation processes using the GOSIA code, it is necessary to consider also at least one state above the ones populated in the Coulomb excitation process [85], to ensure that virtual excitation of unobserved states and coupled-channel truncation effects are correctly taken into account in the analysis. These “buffer

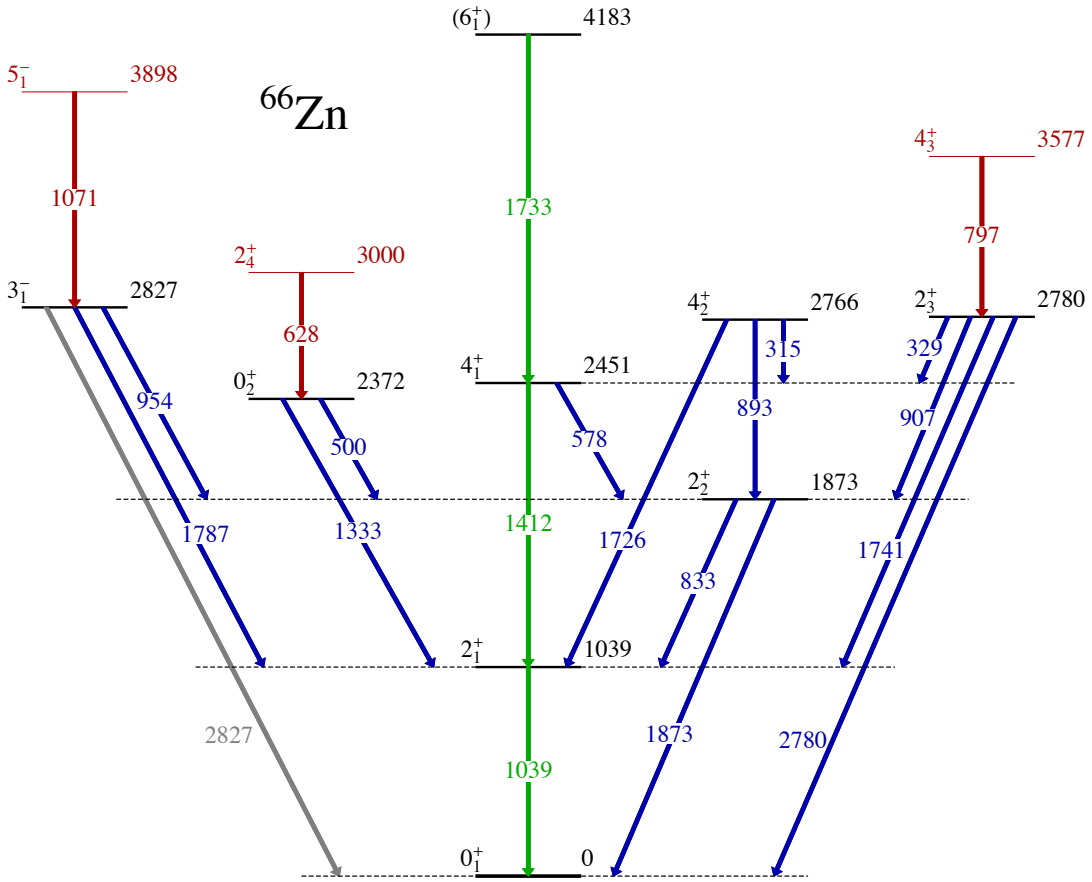

Figure 6.3: Level scheme of ^{66}Zn used in the GOSIA calculations. This is the same as the one reported in figure 1.10, with the addition of the "buffer states" states 5_1^-, 2_4^+ and 4_3^+ and their de-exciting transitions (marked in red). Also the $4_1^+ \longrightarrow 2_2^+$ has been added (see the text for the details). The transitions considered for the preliminary analysis described in the text, aimed at discriminating between different values of $\tau\left(4_1^+\right)$, are shown in green.

states" are needed to correctly determine the matrix elements related to populated states (the $B(E2)$ value of a transition from a buffer state to a populated state cannot be determined). Three buffer states were added to the considered level scheme: 5_1^-, 2_4^+ and 4_3^+, as shown in red in figure 6.3. Since in this experiment the contribution of the transitions de-exciting the 4_2^+ and $\left(6_1^+\right)$ states is negligible, also these two have been included as buffer states. All the states shown in figure 6.3 have been observed in previous measurements [100], except the 2_4^+ state. No 2^+ state decaying to the 0_2^+ state is reported in the literature; thus its energy has been estimated using the rotational model and looking at the systematics of the nuclei in the same mass region. The transition $4_1^+ \longrightarrow 2_2^+$ is not reported in the literature; however, since it is predicted in the quasi-rotational bands interpretation of ^{66}Zn, it has been included in the GOSIA calculations.

Typically, only the γ-decay is observed in low-energy Coulomb excitation experiments; however, a nuclear state can also de-excite through the emission of an internal conversion electron. In order to take into account this unobserved contribution, and thus to correctly reproduce the decay process, the internal conversion coefficients must be provided in the GOSIA input file. In the present analysis $E1$, $E2$, $E3$ and $M1$ multipolarities have been considered, in the energy range of $200 - 3000$ keV. The values have been taken from the BRICC database [129].

Spectroscopic data obtained in previous experiments (such as lifetimes, branching and mixing ratios) were included in the analysis, together with their uncertainties. The values, which are reported in table 6.1, are used as additional data points, entering the χ^2 function on an equal basis with the γ–ray yields observed in the Coulomb excitation experiment. The lifetimes of the 4_1^+ and 2_2^+ states were not included since conflicting results are present in the literature (see figure 1.9).

The finite size of the GALILEO HPGe detectors have to be considered in the GOSIA calculations to reproduce the γ-energy dependence on the solid angle attenuation factors. To this end one has to specify the length of the germanium crystals (6 cm), the distance between their front surface and the target (22 cm) and the diameter of the active surface (4.7 cm), which corresponds to the surface that is determined by the inner part of the lead collimators positioned in front of the detectors. The positions (polar and azimuthal angles with respect to the beam direction, reported in figure 3.3) of all the 24 HPGe are also included. GALILEO is treated as a single detector in the following analysis; however, the relative efficiencies of each HPGe are explicitly declared in the GOSIA input file using the GREMLIN parametrization, as described in section 4.1.4. This allows a correct description of the angular distribution of the emitted γ–rays in the de-excitation process.

During the GOSIA analysis, the Coulomb excitation cross section is integrated over

Lifetimes		
State	τ [ps]	$\Delta\tau$ [ps]
2_1^+	2.42	0.04
$\left(6_1^+\right)$	0.22	0.09
2_3^+	0.38	0.10
3_1^-	0.260	0.010
Mixing Ratios		
Transition	δ	$\Delta\delta$
$2_2^+ \longrightarrow 2_1^+$	-2.0	0.7
$2_3^+ \longrightarrow 2_1^+$	0.33	0.28
Branching Ratios		
Transition	BR	ΔBR
$2_2^+ \longrightarrow 0_1^+ / 2_2^+ \longrightarrow 2_1^+$	0.0039	0.0003
$0_2^+ \longrightarrow 2_2^+ / 0_2^+ \longrightarrow 2_1^+$	0.0041	0.0010
$4_2^+ \longrightarrow 2_1^+ / 4_2^+ \longrightarrow 2_2^+$	0.87	0.03
$4_2^+ \longrightarrow 4_1^+ / 4_2^+ \longrightarrow 2_2^+$	0.36	0.02
$2_3^+ \longrightarrow 2_1^+ / 2_3^+ \longrightarrow 0_1^+$	0.231	0.003
$2_3^+ \longrightarrow 2_2^+ / 2_3^+ \longrightarrow 0_1^+$	0.177	0.012
$3_1^- \longrightarrow 2_2^+ / 3_1^- \longrightarrow 2_1^+$	0.113	0.013

Table 6.1: Spectroscopic values assumed in the present analysis. Values taken from [100].

the angular range covered by the particle detector. For this reason, a description of the SPIDER geometry has to be provided. One detector (D3) was not used during the experiment and one strip (D1S6) was powered off, so that the particle detector geometry is asymmetric with respect to the beam axis. Moreover, also the de-centering discussed in section 4.4.1 has to be considered. A correct description of the actual geometry of SPIDER has been achieved using the so-called "meshpoints" inside GOSIA. Indeed, the code provides a method to describe complicated shapes of the particle detector, defining its boundaries in the (θ, ϕ) plane. Using the center-of-mass angles of each strip shown in figure 4.15, it has been possible to provide the ϕ boundaries for a selected number of θ meshpoints, for each SPIDER ring. This has been done in steps of one degree from the minimum to the maximum θ angle covered by SPIDER. The final SPIDER shape over the (θ, ϕ) plane, corresponding to the range in which the cross-section is integrated, is then calculated by GOSIA by interpolating upper and lower limits of each meshpoint.

For the beam energy and the target thickness, the values obtained in section 5.3 have been given as input data. The stopping powers obtained from SRIM calculations [84]

have been included in the GOSIA input file, for several energy meshpoints between the minimum and the maximum energy of the ^{66}Zn ions inside the target.

The lifetime of the ^{66}Zn 2_1^+ state is known with a high precision (see figure 1.9), for this reason the experimental data are normalized to $\tau\left(2_1^+\right)$ in the present analysis.

6.1.1 Preliminary Analysis

The sensitivity of the Coulomb excitation cross-section on the scattering angle and on the $Q_s\left(2_1^+\right)$ value in the present experiment is shown in figure 6.4, where the relative population of the 2_2^+ state of ^{66}Zn is reported as a function of the projectile scattering angle. The calculations have been performed using the transition probabilities taken from the NNDC database [100]. The population clearly depends on the scattering angle. This is due to the fact that the 2_2^+ state can be also populated by a two-step process ($0_1^+ \longrightarrow 2_1^+ \longrightarrow 2_2^+$), which, as already discussed in section 2.1.2, is enhanced for large scattering angles. The sensitivity to $Q_s\left(2_1^+\right)$ is remarkable. In particular, the difference in the relative population of the 2_2^+ state considering the value reported in [35] ($Q_s\left(2_1^+\right) = 0.24$ eb) and its opposite is about a factor of two.

As it was already pointed out in the previous Coulomb excitation measurement of ^{66}Zn [35], the ratio between the yields of the $4_1^+ \longrightarrow 2_1^+$ and $2_1^+ \longrightarrow 0_1^+$ transitions

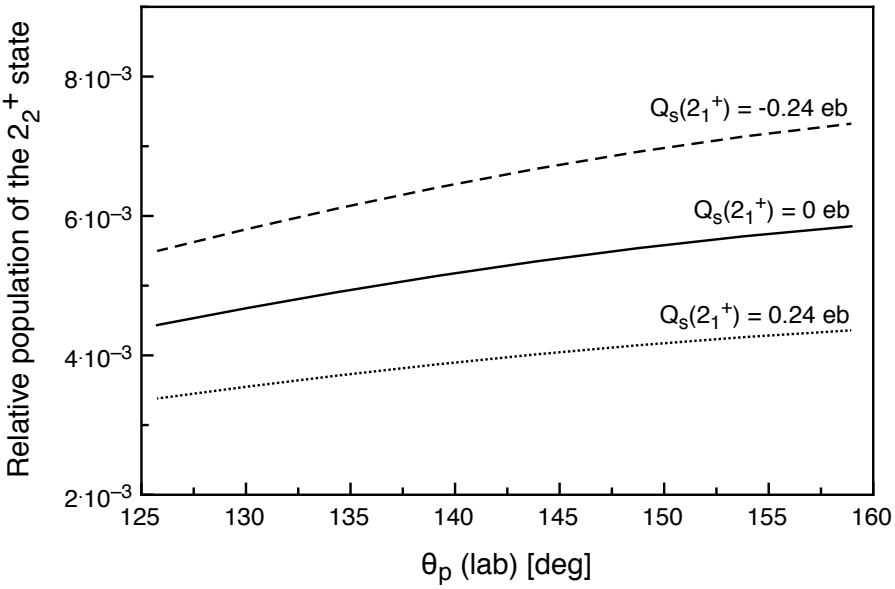

Figure 6.4: Relative population of the 2_2^+ state as a function of the projectile scattering angle (the sum of the relative populations of all the states considered in the level scheme reported in figure 1.10 is 1). The calculations have been performed for three different values of $Q_s\left(2_1^+\right)$.

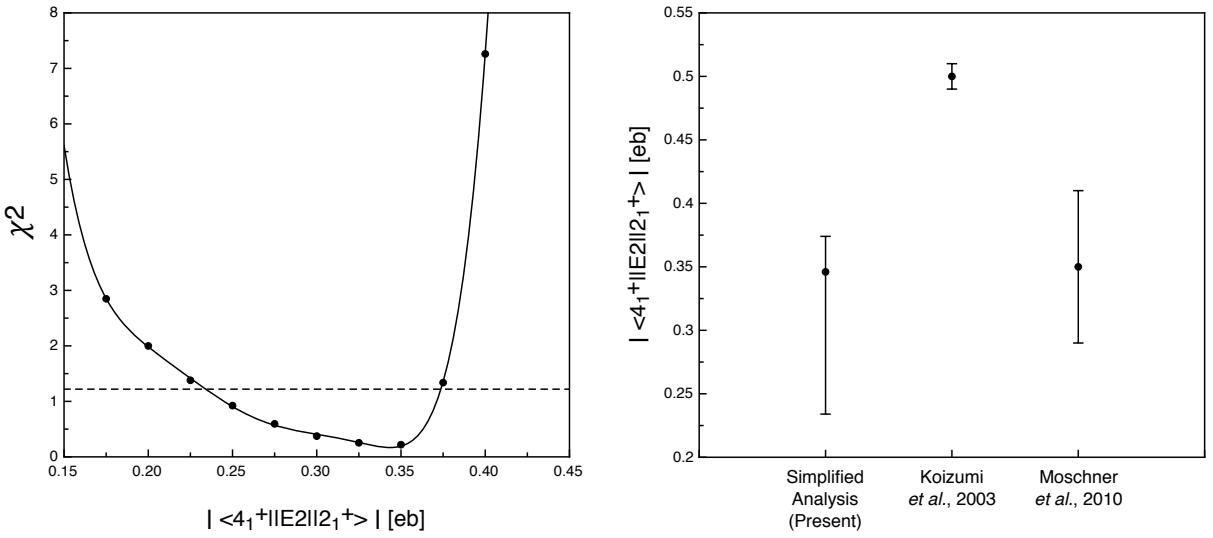

Figure 6.5: Results of the simplified analysis considering only the 0_1^+, 2_1^+, 4_1^+ and 6_1^+ states. Left panel: χ^2 value as a function of the absolute value of the $\langle 4_1^+||E2||2_1^+\rangle$ reduced matrix element (black dots); the solid line is a polynomial fit. The dashed, horizontal line marks the $\chi^2 = \chi^2_{min} + 1$ level, corresponding to 1σ error bar. Right: comparison of the $|\langle 4_1^+||E2||2_1^+\rangle|$ reduced matrix element obtained in the present simplified analysis with the values previously obtained by M. Koizumi *et al.* [35] and K. Moschner *et al.* [51].

depends only slightly on $Q_s\left(2_1^+\right)$. It is therefore possible to obtain information about the lifetime of the 4_1^+ state in a simplified analysis, in which only the 0_1^+, 2_1^+, 4_1^+ states and the $\left(6_1^+\right)$ buffer state are considered (as shown in figure 6.3, transitions marked in green). The only experimental yields included in the calculations are therefore the ones relative to the $4_1^+ \longrightarrow 2_1^+$ and $2_1^+ \longrightarrow 0_1^+$ transitions, given for 8 different scattering angle ranges (16 experimental data points). In this analysis the signs of the matrix elements connecting the states were chosen to be positive, and the diagonal reduced matrix element $\langle 4_1^+||E2||4_1^+\rangle$ was coupled to the $\langle 2_1^+||E2||2_1^+\rangle$ by the rule $Q_s\left(4_1^+\right) = 1.266 \cdot Q_s\left(2_1^+\right)$, from a simple rotation-vibration model [35]. In figure 6.5, the χ^2 value obtained from the GOSIA minimization procedure is reported as a function of the absolute value of the $\langle 4_1^+||E2||2_1^+\rangle$ reduced matrix element. In spite of the large error, it is already possible to see how the value obtained by this simplified analysis for $|\langle 4_1^+||E2||2_1^+\rangle|$ agrees with the value reported in [51] and rules out the one reported in [35]. For this reason, the lifetime of the 4_1^+ state reported in [51] has been included among the additional spectroscopic data used in the final analysis. The fact that the ratio between the yields of the $4_1^+ \longrightarrow 2_1^+$ and $2_1^+ \longrightarrow 0_1^+$ transitions depends only slightly on $Q_s\left(2_1^+\right)$ is also confirmed. Indeed, the value of the $\langle 2_1^+||E2||2_1^+\rangle$ matrix element can be varied in the range from -0.6 eb up to $+1.6$ eb,

without exceeding the $\chi^2_{min}+1$ condition. The dependence of the same ratio on $Q\left(4^+_1\right)$ is even more negligible.

6.1.2 Final Analysis

The results of the global GOSIA analysis, performed including the entire level scheme shown in figure 6.3, are summarized in table 6.2. The reduced χ^2 value obtained at the end of the minimization process is $\chi^2_{min}/DOF = 0.68$.

As discussed in section 2.1.2, multi-step Coulomb excitation is sensitive to the signs of the matrix elements. However, the wave function of each state has an arbitrary phase, which is selected by fixing the sign of one matrix element for each state. In this way a consistent phase convention is ensured, which allows a comparison with model predictions. The signs that have been fixed during the analysis are reported in table 6.2 within brackets. The signs of the remaining matrix elements are determined according to the fixed ones.

ME		$B\left(\Omega L\right)$ / Q_s	
$\langle 2^+_1 \|\| E2 \|\| 0^+_1 \rangle$	$(+)\,0.373\,(14)$ eb	$B\left(E2; 2^+_1 \longrightarrow 0^+_1\right)$	$280\,(20)$ e^2fm^4
$\langle 4^+_1 \|\| E2 \|\| 2^+_1 \rangle$	$(+)\,0.345\,(16)$ eb	$B\left(E2; 4^+_1 \longrightarrow 2^+_1\right)$	$132\,(12)$ e^2fm^4
$\langle 0^+_2 \|\| E2 \|\| 2^+_1 \rangle$	$(+)\,0.074\,(5)$ eb	$B\left(E2; 0^+_2 \longrightarrow 2^+_1\right)$	55^{+7}_{-8} e^2fm^4
$\langle 0^+_2 \|\| E2 \|\| 2^+_2 \rangle$	$+0.056^{+0.008}_{-0.010}$ eb	$B\left(E2; 0^+_2 \longrightarrow 2^+_2\right)$	31^{+9}_{-11} e^2fm^4
$\langle 2^+_2 \|\| E2 \|\| 2^+_1 \rangle$	$(+)\,0.50\,(6)$ eb	$B\left(E2; 2^+_2 \longrightarrow 2^+_1\right)$	$500\,(120)$ e^2fm^4
$\langle 2^+_2 \|\| E2 \|\| 0^+_1 \rangle$	$\pm 0.0047\,(6)$ eb	$B\left(E2; 2^+_2 \longrightarrow 0^+_1\right)$	$0.043\,(12)$ e^2fm^4
$\langle 2^+_3 \|\| E2 \|\| 0^+_1 \rangle$	$-0.064\,(7)$ eb	$B\left(E2; 2^+_3 \longrightarrow 0^+_1\right)$	$8.2\,(18)$ e^2fm^4
$\langle 2^+_3 \|\| E2 \|\| 2^+_1 \rangle$	$(+)\,0.029^{+0.005}_{-0.013}$ eb	$B\left(E2; 2^+_3 \longrightarrow 2^+_1\right)$	$1.7^{+0.6}_{-1.6}$ e^2fm^4
$\langle 2^+_3 \|\| E2 \|\| 2^+_2 \rangle$	$+0.43^{+0.06}_{-0.05}$ eb	$B\left(E2; 2^+_3 \longrightarrow 2^+_2\right)$	360^{+100}_{-90} e^2fm^4
$\langle 3^-_1 \|\| E1 \|\| 2^+_1 \rangle$	$(+)\,0.0052\,(6)$ eb$^{1/2}$	$B\left(E1; 3^-_1 \longrightarrow 2^+_1\right)$	$3.8\,(9)\cdot 10^{-4}$ e^2fm^2
$\langle 3^-_1 \|\| E1 \|\| 2^+_2 \rangle$	$(+)\,0.0044\,(7)$ eb$^{1/2}$	$B\left(E1; 3^-_1 \longrightarrow 2^+_2\right)$	$2.8\,(9)\cdot 10^{-4}$ e^2fm^2
$\langle 3^-_1 \|\| E3 \|\| 0^+_1 \rangle$	$(+)\,0.092^{+0.014}_{-0.019}$ eb$^{3/2}$	$B\left(E3; 3^-_1 \longrightarrow 0^+_1\right)$	$1.2^{+0.4}_{-0.5}\cdot 10^3$ e^2fm^6
$\langle 2^+_2 \|\| M1 \|\| 2^+_1 \rangle$	$-0.18^{+0.05}_{-0.09}$ μ_N	$B\left(M1; 2^+_2 \longrightarrow 2^+_1\right)$	$0.006^{+0.003}_{-0.006}$ μ_N^2
$\langle 2^+_3 \|\| M1 \|\| 2^+_1 \rangle$	$+0.138^{+0.016}_{-0.017}$ μ_N	$B\left(M1; 2^+_3 \longrightarrow 2^+_1\right)$	$0.0038\,(9)$ μ_N^2
$\langle 2^+_1 \|\| E2 \|\| 2^+_1 \rangle$	$+0.30\,(7)$ eb	$Q_s\left(2^+_1\right)$	$+23^{+6}_{-5}$ $e$fm^2
$\langle 2^+_2 \|\| E2 \|\| 2^+_2 \rangle$	$-0.32^{+0.12}_{-0.16}$ eb	$Q_s\left(2^+_2\right)$	-25^{+9}_{-12} $e$fm^2

Table 6.2: Left: matrix elements obtained in this work. A positive sign has been assigned to the ones reported in brackets, while sensitivity was not sufficient to determine the one reported as $\pm$. Right: $B\left(E2\right)$ and Q_s values deduced from the matrix elements reported on left.

Opposite signs with respect to the ones shown in table 6.2, chosen one at a time for each matrix element, result in a larger χ^2. For the small matrix elements $\langle 2_2^+||E2||0_1^+\rangle$, the sensitivity to the interference term is not sufficient to determine the relative sign.

The error estimation of the GOSIA code is performed in two steps: at first the non-correlated errors are estimated by computing the χ^2 values for various values of a given matrix element, close to the calculated minimum. Then, correlations are taken into account, allowing to estimate the dependence of a given matrix elements on the others. The final statistical error corresponds to a 68.3% confidence limit on each matrix element [85].

As to the possibility of determining the sign of $Q_s\left(2_1^+\right)$, the interference term of the excitation probability $P\left(2_2^+ \longrightarrow 0_1^+\right)$ (which was described by equation 2.21)

$$P_3 = \left\langle 0_1^+ \,||E2||\, 2_2^+ \right\rangle \left\langle 2_2^+ \,||E2||\, 2_1^+ \right\rangle \left\langle 2_1^+ \,||E2||\, 0_1^+ \right\rangle \tag{6.1}$$

plays an important role. It is often discussed in the literature how the signs of P_3 and $Q_s\left(2_1^+\right)$ influence each other, producing a constructive or a destructive interference. In the present analysis it is not possible to determine the sign of P_3, due to the insensitivity to the sign of the $\left\langle 2_2^+ \,||E2||\, 0_1^+ \right\rangle$ matrix element. However, this value as been varied over the full range of positive and negative values allowed by the estimated error on its absolute value, observing that the sign of $Q\left(2_1^+\right)$ is not affected by the sign of P_3, as already pointed out in the previous Coulomb excitation measurement of ^{66}Zn [35].

Using the known spectroscopic data reported in table 6.1 it has been possible to obtain reduced matrix elements (or absolute values) also for those unobserved transitions whose branching and mixing ratios are known. For instance, the $B\left(E3; 3_1^- \longrightarrow 0_1^+\right)$ has been deduced since the $E1$ transition $3_1^- \longrightarrow 2_1^+$ has been observed, moreover the lifetime of the 3_1^- state and the branching ratio $3_1^- \longrightarrow 2_2^+/3_1^- \longrightarrow 2_1^+$ are known. The contribution of the allowed $E3$, $E5$, $M2$, $M4$ multipolarities to the $3_1^- \longrightarrow 2_1^+$ and $3_1^- \longrightarrow 2_2^+$ transitions has been neglected.

A comparison between the experimental γ–ray yields and those calculated from the final minimization output is shown in figure 6.6, for the three most intense observed transitions. The agreement is satisfactory. The newly calculated values for lifetimes, mixing and branching ratios (shown in table 6.3) are also in agreement with the ones used as input (shown in table 6.1).

The set of matrix elements obtained in this work allows the determination of the quadrupole deformation of the 0_1^+ ground state using the method described in section 2.2. The two parameters Q and δ have been obtained, which are related to the Hill-Wheeler β and γ parameters by the relations $\langle Q^2\rangle = q_0^2\,\langle\beta^2\rangle$, $\langle Q^3\cos 3\delta\rangle = q_0^3\,\langle\beta^3\cos 3\gamma\rangle$, $q_0 = \frac{3}{4\pi}ZR_0^2$, $R_0 = 1.2A^{1/3}$ [fm]. Referring to the figure 2.5, it is evident how all the

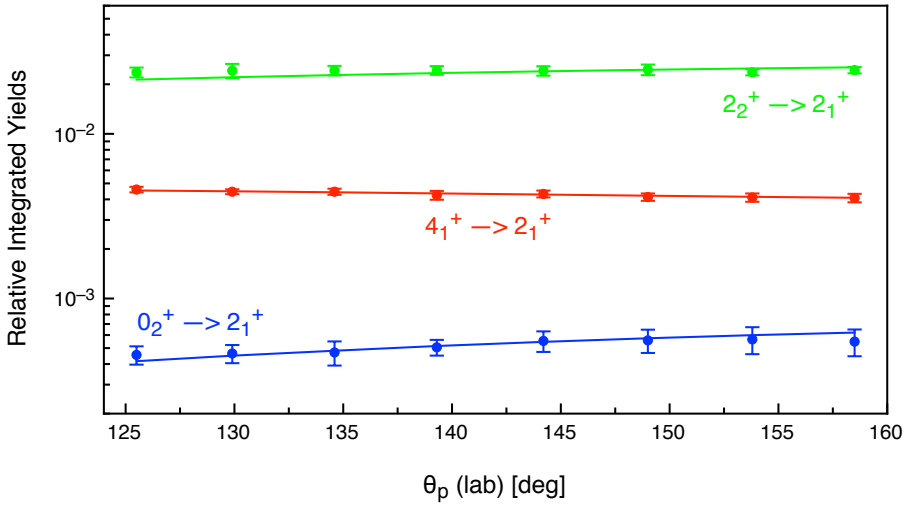

Figure 6.6: Comparison between experimental (dots) and calculated (continuous lines) γ–ray yields for the three most intense transitions observed in the ^{66}Zn experiment. These yields are integrated over the target thickness and the SPIDER rings angular coverage and normalized to the $2_1^+ \longrightarrow 0_1^+$ transition.

matrix elements necessary to determine the first parameter, Q, have been measured (the influence of higher-lying unobserved 2^+ states can be neglected). For the determination of the triaxiality parameter δ, the matrix element $\langle 2_3^+||E2||2_3^+\rangle$ is missing, and the sign of the $\langle 2_2^+||E2||0_1^+\rangle$ has not been determined. These matrix elements appear in the following terms of equation 2.31:

$$\langle 0_1^+||E2||2_3^+\rangle\langle 2_3^+||E2||2_3^+\rangle\langle 2_3^+||E2||0_1^+\rangle \tag{6.2}$$

$$\langle 0_1^+||E2||2_1^+\rangle\langle 2_1^+||E2||2_2^+\rangle\langle 2_2^+||E2||0_1^+\rangle \tag{6.3}$$

$$\langle 0_1^+||E2||2_2^+\rangle\langle 2_2^+||E2||2_2^+\rangle\langle 2_2^+||E2||0_1^+\rangle \tag{6.4}$$

$$\langle 0_1^+||E2||2_2^+\rangle\langle 2_2^+||E2||2_3^+\rangle\langle 2_3^+||E2||0_1^+\rangle \tag{6.5}$$

The contributions of these terms, as well as the effect of higher-lying 2^+ states, are negligible when compared to those of the other terms. Due to the fact that the matrix elements $\langle 0_1^+||E2||2_2^+\rangle$ and $\langle 0_1^+||E2||2_3^+\rangle$ are particularly small in ^{66}Zn, the triaxiality parameter δ is practically determined only by the term

$$\langle 0_1^+||E2||2_1^+\rangle\langle 2_1^+||E2||2_1^+\rangle\langle 2_1^+||E2||0_1^+\rangle \tag{6.6}$$

The Q and δ parameters have been calculated using equations 2.30 and 2.31 as follows:

$$\langle Q^2\rangle = 0.143\,(10)\ \ e^2\mathrm{b}^2 \tag{6.7}$$

$$\langle Q^3\cos 3\delta\rangle = -0.035\,(8)\ \ e^3\mathrm{b}^3 \tag{6.8}$$

Lifetimes		
State	τ [ps]	$\Delta\tau$ [ps]
2_1^+	2.40	0.18
4_1^+	1.09	0.10
2_2^+	3.2	0.9
0_2^+	3.5	0.5
2_3^+	0.43	0.07
Mixing Ratios		
Transition	δ	$\Delta\delta$
$2_2^+ \longrightarrow 2_1^+$	-2.0	1.0
$2_3^+ \longrightarrow 2_1^+$	0.31	0.14
Branching Ratios		
Transition	BR	ΔBR
$2_2^+ \longrightarrow 0_1^+/2_2^+ \longrightarrow 2_1^+$	0.0039	0.0003
$0_2^+ \longrightarrow 2_2^+/0_2^+ \longrightarrow 2_1^+$	0.0041	0.0014
$2_3^+ \longrightarrow 2_1^+/2_3^+ \longrightarrow 0_1^+$	0.23	0.10
$2_3^+ \longrightarrow 4_1^+/2_3^+ \longrightarrow 0_1^+$	0.00016	0.00007
$2_3^+ \longrightarrow 2_2^+/2_3^+ \longrightarrow 0_1^+$	0.17	0.05
$3_1^- \longrightarrow 2_2^+/3_1^- \longrightarrow 2_1^+$	0.11	0.04

Table 6.3: Spectroscopic data deduced in the present analysis.

From these two values it is possible to derive the mean Hill-Wheeler parameters, defined by equation 1.13, for the ground state 0_1^+:

$$\langle\beta\rangle = 0.225\,(8) \qquad \langle\gamma\rangle = 43^\circ\,(3^\circ) \tag{6.9}$$

The same procedure has been repeated for the 0_2^+ state. Only the transitions to the 2_1^+, 2_2^+ states have been observed in this work; however, no transitions to other 2^+ states are reported in the literature. For this reason, assuming negligible the contribution of other $\langle 0_2^+||E2||2_i^+\rangle$ matrix elements with respect to the $\langle 0_2^+||E2||2_1^+\rangle$ and $\langle 0_2^+||E2||2_2^+\rangle$ ones, the Q parameter has been obtained

$$\left\langle Q^2\right\rangle = 0.0086^{+0.0012}_{-0.0013}\ e^2\mathrm{b}^2 \tag{6.10}$$

which leads to $\beta = 0.055^{+0.004}_{-0.005}$. In summary, a triaxial shape is associated to ^{66}Zn in its ground state, while the nucleus is almost spherical in the 0_2^+ state.

6.2 Comparison with Previous Measurements

The $B(E2)$ values for the $0_2^+ \longrightarrow 2_1^+$, $0_2^+ \longrightarrow 2_2^+$, $2_3^+ \longrightarrow 2_2^+$, $3_1^- \longrightarrow 2_2^+$ transitions and $Q_s\left(2_2^+\right)$ have been measured for the first time in this work. The other quantities, for which previous measurements are reported in the literature, are presented in table 6.4. The present values, in the second column, are compared to those of the NNDC database [100], to the results of a previous Coulomb excitation measurements (M. Koizumi *et al.* 2003 [35]) and to the ones determined by a previous lifetime measurement (K. Moschner *et al.* 2010 [51]). The precision achieved in the present measurement permits to discriminate between conflicting values, except for the $B\left(M1; 2_2^+ \longrightarrow 2_1^+\right)$. The present results are in agreement with the ones reported by M. Koizumi *et al.* [35], except for the $B\left(E2; 4_1^+ \longrightarrow 2_1^+\right)$ value, which is instead in agreement with the more recent value reported by K. Moschner *et al.* [51]. The sign and the magnitude of $Q_s\left(2_1^+\right)$ confirms the result of [35], also the triaxiality parameter γ there reported ($\gamma = 36^{\circ}{}^{+8^{\circ}}_{-3^{\circ}}$) agrees with the present value ($\gamma = 43^{\circ}\,(3^{\circ})$). For the first time, the reduced matrix element for the octupole transition from the 3_1^- level of ^{66}Zn has been obtained using Coulomb excitation. The calculated value for the corresponding reduced transition probability, $B\left(E3; 3_1^- \longrightarrow 0_1^+\right) = 4.5(15)$ W.u., is about a factor of 4 lower than the value $B\left(E3; 3_1^- \longrightarrow 0_1^+\right) = 20(3)$ W.u. obtained by a previous electron scattering measurement [64].

	$B(\Omega L)\downarrow$ [W.u.]			
Transition (ΩL)	Present	NDS [100]	Koizumi [35]	Moschner [51]
$2_1^+ \longrightarrow 0_1^+$ ($E2$)	17.5 (14)	17.5(4)	18.2(11)	17.4(3)
$4_1^+ \longrightarrow 2_1^+$ ($E2$)	8.3 (8)	18(3)	17.5(7)	8.4(15)
$2_2^+ \longrightarrow 2_1^+$ ($E2$)	32 (7)	330(130)	41(14)	
$2_2^+ \longrightarrow 0_1^+$ ($E2$)	0.0027 (7)	0.032(12)	0.004(18)	
$2_3^+ \longrightarrow 0_1^+$ ($E2$)	$0.52^{+0.13}_{-0.11}$	0.54(15)		
$2_3^+ \longrightarrow 2_1^+$ ($E2$)	$0.10^{+0.03}_{-0.09}$	0.13(20)		
$3_1^- \longrightarrow 2_1^+$ ($E1$)	$3.6\,(9)\cdot 10^{-4}$	$3.6(5)\cdot 10^{-4}$		
$2_2^+ \longrightarrow 2_1^+$ ($M1$)	$4^{+2}_{-4}\cdot 10^{-3}$	0.06(2)	$4(3)\cdot 10^{-3}$	
$2_3^+ \longrightarrow 2_1^+$ ($M1$)	$2.1\,(5)\cdot 10^{-3}$	$2.2(7)\cdot 10^{-3}$		
$Q_s\left(2_1^+\right)$ [$e$fm^2]	$+23^{+6}_{-5}$		+24(8)	

Table 6.4: Some of the reduced transition probabilities measured in this work are compared with those already reported in previous measurements.

6.3 Comparison with Model Predictions

The ratio B_{42} ($B\left(E2; 4_1^+ \longrightarrow 2_1^+\right)/B\left(E2; 2_1^+ \longrightarrow 0_1^+\right)$) obtained in this work is equal to $B_{42} = 0.47(6)$. This value excludes the possibility that the low-lying structure of ^{66}Zn can be simply interpreted within a vibration-rotation picture. A more complex structure is suggested, involving microscopic degrees of freedom, consistently with the proximity to the nickel isotopes, which are semi-magic nuclei ($Z = 28$). In the present work the experimental results are compared both with "beyond mean field" (BMF) and shell model (SM) calculations[1].

BMF calculations, introduced in section 1.1.3, have been performed using the Gogny D1S interaction [12] to define the corresponding Energy Density Functional (EDF). The Symmetry Conserving Configuration Mixing (SCCM) method [130], in which the nuclear states are described as a linear combinations of mean-field states projected on particle number and angular momentum, has been used. The coefficients of the linear combination are calculated self-consistently following the GCM method [131]. Also the Potential Energy Surface (PES) can be calculated as a function of the Hill-Wheeler parameters, as shown in figure 6.7 left panel. A rather shallow minimum at $\beta \sim 0.2$ is observed, characterized by a γ-unstable character. The same conclusion can be reached using the

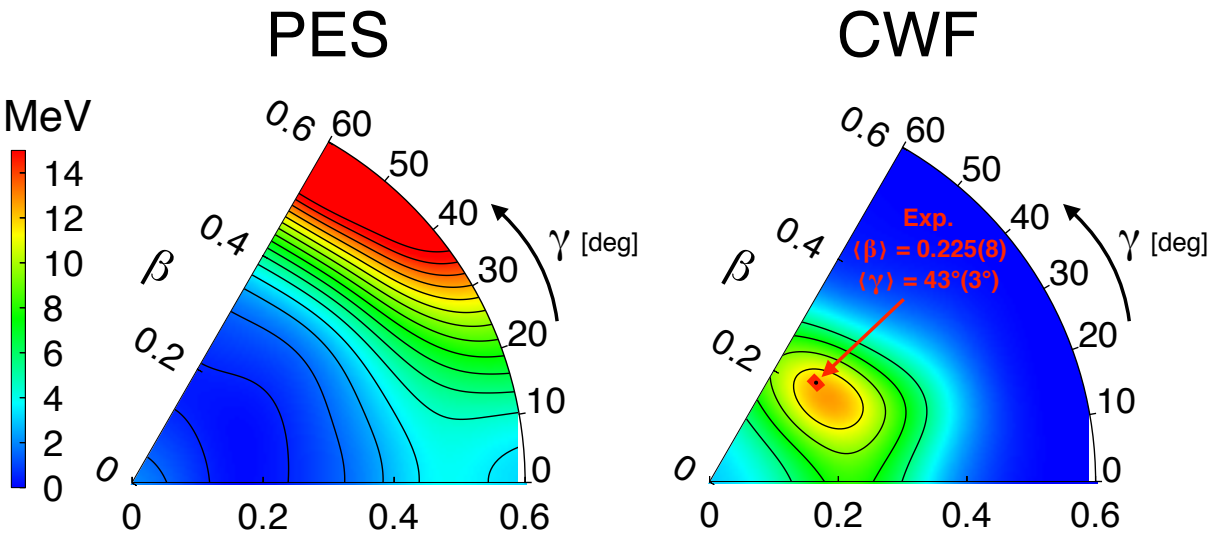

Figure 6.7: Left: Potential Energy Surface (PES) resulting from BMF calculations. Right: Collective Wave Function (CWT) of the ^{66}Zn ground state. The orange/yellow region represents the largest contribution to the wave function, while blue the smallest one. The deformation parameters of the ground state obtained in this work are also shown in red.

[1]Both BMF and SM calculations are still preliminary and will be further refined.

cranked Nilsson-Strutinsky model [132], as reported in [35]. The ground state Collective Wave Function (CWF) represents the weights of each (β, γ) deformation parameters for a considered nuclear state. This has been obtained within the SCCM framework for the ^{66}Zn ground state, as shown in figure 6.7 (right panel). The deformation parameters of the 0_1^+ state obtained in this work, $\langle\beta\rangle$ and $\langle\gamma\rangle$ in red in the same figure, are close to the region where the maximum of the contour plot is located.

SM calculations have been performed using different interactions and model spaces:

- SM-I: calculations performed using the JUN45 effective interaction [52], considering a model space composed by the $2p_{3/2}$, $1f_{5/2}$, $2p_{1/2}$ and $1g_{9/2}$ orbitals for both protons and neutrons (^{56}Ni inert core).

- SM-II: calculations performed using the LNPS effective interaction [133], including the $1f_{7/2}$, $2p_{3/2}$, $1f_{5/2}$, $2p_{1/2}$ orbitals for protons (the so-called *pf* shell) and $2p_{3/2}$, $1f_{5/2}$, $2p_{1/2}$, $1g_{9/2}$, and $2d_{5/2}$ orbitals for neutrons (^{48}Ca inert core).

- SM-III: calculations performed using a two-body interaction calculated within the many-body perturbation theory from the N-N potential CD-Bonn, renormalized by way of the so-called V_{low-k} approach (method introduced in section 1.1.2). Model spaces composed by the $2p_{3/2}$, $1f_{5/2}$, $2p_{1/2}$ and $1g_{9/2}$ orbitals for both protons and neutrons (^{56}Ni inert core). Microscopic effective charges have been used.

- SM-IV: same as SM-III but using empirical effective charges, as in the case of SM-I and SM-II.

In table 6.5 a comparison between the experimental $B(E2)$ and Q_s values with the ones predicted by calculations is presented. Some comments are detailed in the following. The experimental $B\left(E2; 2_1^+ \longrightarrow 0_1^+\right)$ value is in reasonable agreement with all the predicted values, with the exception of SM-II and BMF calculations, which underestimate and overestimate, respectively, the value. The $B\left(E2; 4_1^+ \longrightarrow 2_1^+\right)$ is generally underestimated by all the shell model calculations. It is interesting to notice how the experimental $B\left(E2; 4_1^+ \longrightarrow 2_1^+\right)$ value seems to be closer to the calculated $B\left(E2; 4_2^+ \longrightarrow 2_1^+\right)$ value. It has been observed that a decrease of the energy of the neutron $1g_{9/2}$ orbital in SM calculations leads to an inversion of the first two 4^+ model states. The upper limit of the experimental $B\left(E2; 4_2^+ \longrightarrow 2_1^+\right)$ value reported in [100] (< 0.13 W.u.), seems also to confirm this interpretation. Transitions from the 0_2^+ state are better reproduced by SM-III and SM-IV, while SM-I and SM-II underestimate the $B(E2)$ value of the $0_2^+ \longrightarrow 2_2^+$ and $0_2^+ \longrightarrow 2_1^+$ transitions. Probably, the most intriguing fact is that all the calculations predict a negative sign for $Q_s\left(2_1^+\right)$, at variance with the experimental result. A positive

	$B(\Omega L)\downarrow$ [W.u.]					
Transition (ΩL)	Experimental	SM-I	SM-II	SM-III	SM-IV	BMF
$2_1^+ \longrightarrow 0_1^+$ $(E2)$	$17.5\,(14)$	20	9.9	16	16	30
$4_1^+ \longrightarrow 2_1^+$ $(E2)$	$8.3\,(8)$	1.2	0.012	1.1	0.69	44
$4_2^+ \longrightarrow 2_1^+$ $(E2)$		24	7.6	19	16	3
$0_2^+ \longrightarrow 2_1^+$ $(E2)$	$3.5^{+0.4}_{-0.5}$	1.6	0.44	1.7	1.4	18
$0_2^+ \longrightarrow 2_2^+$ $(E2)$	$2.0^{+0.6}_{-0.7}$	0.20	2.5	3	1.4	15
$2_2^+ \longrightarrow 2_1^+$ $(E2)$	$32\,(7)$	18	3.3	11	8.1	45
$2_2^+ \longrightarrow 0_1^+$ $(E2)$	$0.0027\,(7)$	0.32	1.5	0.63	0.06	0.018
$2_3^+ \longrightarrow 0_1^+$ $(E2)$	$0.52^{+0.13}_{-0.11}$	0.35	0.13		0.063	0.071
$2_3^+ \longrightarrow 2_1^+$ $(E2)$	$0.10^{+0.03}_{-0.09}$	0.21	5.5		3	1.2
$2_2^+ \longrightarrow 2_1^+$ $(M1)$	$4^{+2}_{-4} \cdot 10^{-3}$	$1 \cdot 10^{-3}$	0.18		0.028	$5.9 \cdot 10^{-3}$
$2_3^+ \longrightarrow 2_1^+$ $(M1)$	$2.1\,(5) \cdot 10^{-3}$	0.13	0.05		0.18	$2.7 \cdot 10^{-3}$
$3_1^- \longrightarrow 0_1^+$ $(E3)$	$4.6^{+1.4}_{-1.9}$				10.7	
$Q_s\left(2_1^+\right)$ [$e$fm^2]	$+23^{+6}_{-5}$	-22	-13	-22	-24	-9.2
$Q_s\left(2_2^+\right)$ [$e$fm^2]	-24^{+9}_{-12}	22	4.3		20	13

Table 6.5: Comparison between the experimental results obtained in this work and the ones calculated using the SM (see the text for the details) and the BMF approach.

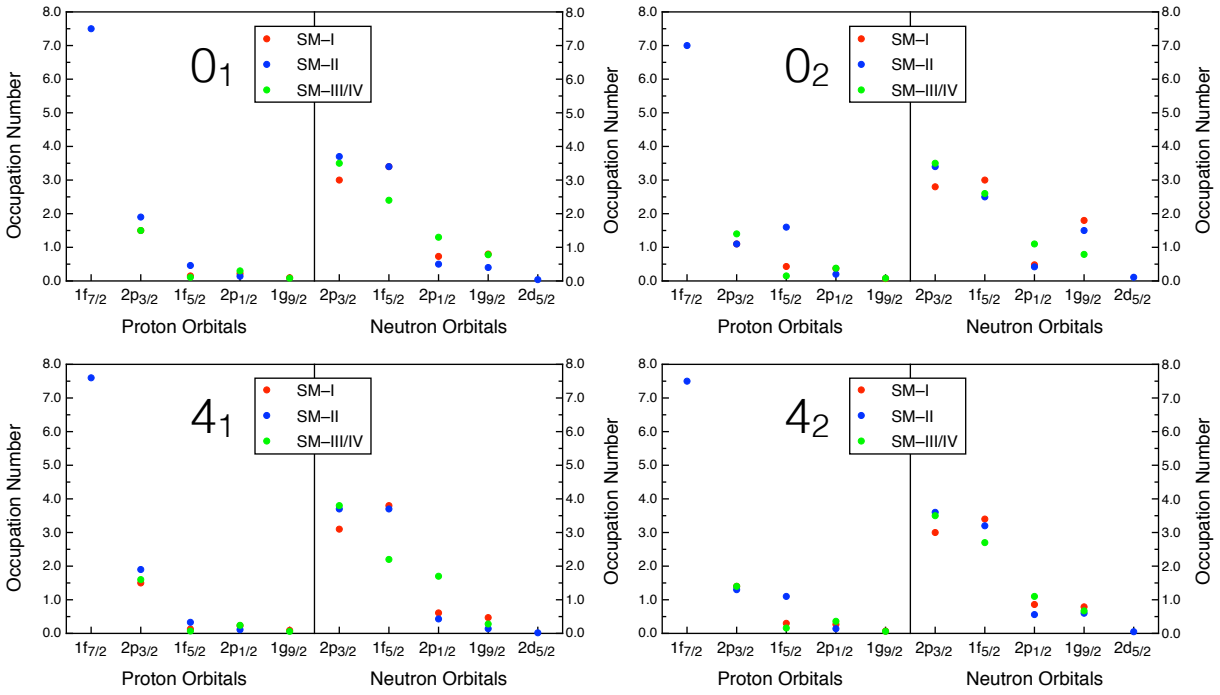

Figure 6.8: Proton and neutron occupation numbers resulting from SM calculations for the 0_1^+, 0_2^+, 4_1^+ and 4_2^+ states.

$Q_s\left(2_1^+\right)$ value was predicted only by the Projected Hartree-Fock-Bogoliubov method [134] used in [35]. It is also interesting to notice that the signs of the experimental Q_s values of the first two 2^+ states are exchanged with respect to the predictions. However, their magnitudes are well reproduced by SM-I, SM-III, SM-IV calculations.

The proton and neutron occupation numbers obtained for the 0_1^+, 0_2^+, 4_1^+ and 4_2^+ states by SM calculations are reported in figure 6.8. From the SM-II results, it is visible the non-negligible role played by proton excitations from the $1f_{7/2}$ orbital, suggesting that a ^{48}Ca inert core is preferable to the ^{56}Ni core. The influence of the proton $1g_{9/2}$ and neutron $2d_{5/2}$ orbitals seems instead negligible, so that these orbitals could be omitted in the calculations. On the contrary, the role of the neutron $1g_{9/2}$ orbital appears to be important, in particular in the case of the 0_2^+ state. Since the SM-III/IV calculations seem to be the ones that better reproduce the $B\left(E2\right)$ values from the 0_2^+ state, this could be an indication that the role of the neutron $1g_{9/2}$ orbital is overestimated in the SM-I/II calculations.

The calculations presented in table 6.5 are still preliminary, and will be further refined to obtain definitive conclusions about the structure of ^{66}Zn. However, this preliminary comparison, seems to suggests that ^{66}Zn cannot be simply considered as a vibrational or a rotational nucleus. The microscopic degrees of freedom seems to be important in its description, in which also triaxiality has to be taken into account.

CHAPTER 7

CONCLUSIONS AND FURTHER PERSPECTIVES

In this thesis, the first experiment using the newly implemented heavy-ion detector SPIDER has been described. The detector has been coupled to the GALILEO γ–ray array, recently installed at LNL, to study the structure of the low-lying states in ^{66}Zn using the low-energy Coulomb excitation technique. Reduced transition probabilities and spectroscopic quadrupole moments have been deduced from a set of matrix elements obtained from the experimental γ–ray yields, by performing an analysis with the least-squared minimization code GOSIA. In particular, the $B\left(E2\right)$ values for the $0_2^+ \longrightarrow 2_1^+$, $0_2^+ \longrightarrow 2_2^+$, $2_3^+ \longrightarrow 2_2^+$, the $B\left(E1; 3_1^- \longrightarrow 2_2^+\right)$ value and the $Q_s\left(2_2^+\right)$ value have been obtained for the first time. The precision achieved permits to solve discrepancies present in the literature regarding the $B\left(E2; 4_1^+ \longrightarrow 2_1^+\right)$ and $B\left(E2; 2_2^+ \longrightarrow 2_1^+\right)$ values, which are crucial observables to investigate the collective properties of ^{66}Zn. Also, the first Coulomb excitation measurement of the $B\left(E3; 3_1^- \longrightarrow 0_1^+\right)$ in this nucleus has been obtained. Combining the obtained set of matrix elements using the quadrupole sum rule, the Hill-Wheeler parameters, which describe the nuclear quadrupole deformation, have been deduced for the ^{66}Zn 0_1^+ and 0_2^+ states. The results of this work have triggered new shell model and "beyond mean field" calculations, which are now in progress. A preliminary comparison between experimental and theoretical values obtained from shell model calculations, already demonstrates which is the best model space to be considered for the description of the structure of the low-lying states in ^{66}Zn. The results obtained in this work appear to be generally consistent with the preliminary shell model and BMF predictions, except for the sign of the quadrupole moments of the 2_1^+ and 2_2^+ states, which will be the object of further investigation. As a conclusion, ^{66}Zn cannot be simply considered as a vibrational or a rotational nucleus, as supposed in previous works. Microscopic degrees of freedom and triaxiality play an important role in its description. These results can be useful also

to get new insights into the structure of nuclei in the same mass region.

The good agreement of the present results with the ones already available in the literature proves the high performances of the GALILEO and SPIDER setup. SPIDER has been implemented during this thesis by performing simulations and tests, both in the laboratory and in-beam environments. SPIDER has been adapted to the GALILEO vacuum chamber with the aim to make its employment very easy, allowing to modify the setup in a less than one hour. This is particularly important since GALILEO is often used with different ancillary devices during the same experimental campaign. The existing GALILEO codes have been modified in order to include the data acquired with SPIDER in the analysis. The final software can be used in future experiment changing only few input parameters (such as mass and charge numbers of projectile and target).

The analysis of the SPIDER response to irradiation with heavy ions has led to new results regarding radiation damage and cross-talk/charge-sharing effects in silicon strip detectors. In particular, the results from the radiation damage analysis offer the possibility to optimize the beam current in future experiments. Also, the GEANT4 simulations, which provide the shape of the γ–ray and particle energy spectra, have been validated. The high-quality of the energy spectra measured with SPIDER allows to have a good control of possible systematic errors in Coulomb excitation analysis, such as uncertainties in the beam energy or in the target thickness/composition.

A number of new experiments with the GALILEO and SPIDER setup have been already planned using the stable beams available at LNL using the Tandem-PIAVE-ALPI accelerator complex. One of these will be performed in the next year:

- **Probing collectivity and configuration coexistence in ^{94}Zr with low-energy Coulomb excitation.** *Spokespersons: D. Doherty (University of Surrey, UK), M. Rocchini and M. Zielińska (CEA Salcay, France)*
  Aim of the experiment is to study how collectivity evolves in Zr isotopes, and the coexistence observed between various single-particle configurations (see figure 7.1). This investigation is now possible thanks to the state-of-the-art Monte Carlo shell model calculations that have recently been performed for the zirconium isotopic chain. Such calculations, with large model spaces, have allowed for detailed studies of the consequences of the collective motion of many nucleons, such as the nuclear shape. The investigation of the intrinsic shapes of the 2_1^+ and 2_2^+ states, through the measurement of their quadrupole moments, is a key goal of this experiment.

Other experiments using stable beams are also under discussion, for instance the investigation of core-excitation in ^{58}Ni and shape evolution in Xe isotopes. Several letters of intent have been submitted to use the SPIDER array as an ancillary detector for Coulomb

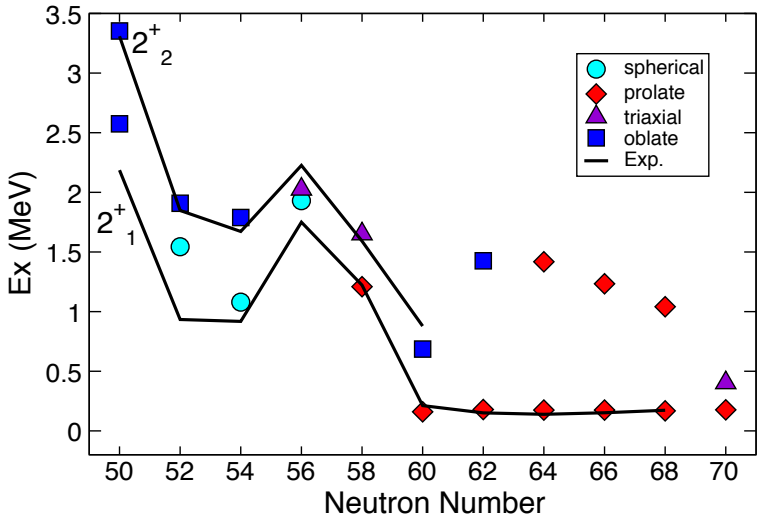

Figure 7.1: Energy of the 2_1^+ and 2_2^+ states in Zr isotopes, as a function of the neutron number. Symbols are theoretical results reported in [135] with the shape classification as shown in the legend. Solid lines denote experimental data [100].

excitation experiments with the radioactive beams delivered by the SPES facility at LNL: these include studies of nuclei close to ^{132}Sn[1].

The possibility to add other detectors to the GALILEO and SPIDER setup is also under study. $LaBr_3$:Ce detectors can be coupled to detect high-energy γ–rays, a plunger device can be simultaneously used to measure lifetimes and a radiation-resistant heavy-ion detector, composed by plastic scintillators, can be used at forward angles to increase the angular coverage of the detected heavy ions.

In conclusion, a new experimental setup for Coulomb excitation measurements is now available at LNL, composed by the GALILEO and SPIDER arrays. The first experiment has been successfully performed, paving the way for future experimental campaigns, in particular, by exploiting the first radioactive beams which will be provided by the SPES facility in the next future.

[1]SP: B. Melon and M. Rocchini (INFN, Sezione di Firenze, Firenze, Italy).

ACKNOWLEDGEMENTS

In order to get a Ph.D., it is necessary to read many books and many articles. However, looking back at these three years, I found that most of what I learned is because the people with whom I had the pleasure of working. I had many teachers during my Ph.D. and three of them have been really fundamental in my education.

First of all, I want to thank my supervisor, Prof. Adriana Nannini. She always encouraged my activity, following constantly my work and giving me new ideas and suggestions. I really enjoyed the possibility to follow a project from the preparation of the proposal up to the final analysis, as well as the pleasant working atmosphere that she has been able to create in Florence. Most of all, she taught me to look always to the next step, without resting on what has been done. It is difficult for me to imagine a better supervisor.

The University of Florence does not allow to have any official co-supervisor. However, it cannot forbid me to say that I consider, definitely, Katarzyna Hadyńska-Klęk my co-supervisor "de facto". She has followed the project of coupling SPIDER to GALILEO from the very beginning, working with me shoulder-to-shoulder for almost one year, from the preparation of the proposal up to the experiment. Moreover, she was also my personal GOSIA teacher, and she was always available for discussions about the analysis. Really thank you, Kasia.

I would like also to thank prof. Pietro Sona. His experience and knowledge regarding the many aspects of nuclear physics have been a constant guideline during my Ph.D.. I cannot count all the times in which he helped me. He is, without any doubt, the physicist who I would like to become one day.

The work described in this thesis involved many people and it is only thanks to all of them if I had the chance to write this thesis.

A huge thanks to all the γ-spectroscopy group of Florence, who started to think about SPIDER before my arrival, in particular: Marco Ottanelli, who I consider a sort of "Swiss

army knife" technician, since he has expertise of almost everything, Barbara Melon who did a lot of work for SPIDER before me, Andrea Perego, who developed the acquisition system and analysis software for the SPIDER tests in Firenze (and made us all laugh many times with his jokes) and Angela Giannatiempo, who carefully read the final draft of this thesis giving me important advice.

The use of SPIDER with GALILEO would not be possible without the interest of José Javier Valiente Dobón, who have followed the project from the very beginning, supervising each step of the work. I spent a lot of time in Legnaro and it was always a pleasure to work with the LNL γ-spectroscopy group. I would like to thank in particular: Alain Goasduff, who developed the GEANT4 simulations reported in this thesis and the original GALILEO data analysis software, helping me a lot during my analysis, Philipp John, who took care about the HPGe detectors (which were perfect during the experiment), Dmitry Testov and Daniele Mengoni, for their help with the SPIDER electronics, Marco Siciliano, who helped me and Kasia many times and in many aspects, Dino Bazzacco and Francesco Recchia, who took care about the data acquisition during the ^{66}Zn experiment. I would like to thank also the technicians of LNL and Padova: Paolo Cocconi, who designed the printed circuit board to adapt SPIDER to the GALILEO preamplifiers, Loris Ramina and Mirco Rampazzo, who designed the SPIDER holder for the GALILEO vacuum chamber and Davide Rosso who always helped us with the HPGe detectors.

Special thanks to Magda Zielińska, who found for us the perfect physics case for the first experiment for SPIDER and GALILEO, ^{66}Zn.

I want also to thank the Warsaw collaborators: Pawel Napiorkowski, Magdalena Matejska-Minda and Michalina Komorowska who provided a valuable contribution to the ^{66}Zn experiment, as experts of Coulomb excitation measurements.

Many tests have been performed at LABEC in Firenze, for this, I have to thank Massimo Chiari, who gave a significant contribution to this work helping with the accelerator and taught me how to use the SIMNRA code, and Caroline Czelusniak, who provided us the ^{7}Li beam.

The theoretical calculations presented in this thesis have been performed by Tomas Raul Rodriguez (BMF calculations), by Houda Naidja (SM-I/II) and Angela Gargano (SM-III/IV). I want to thank all of them for their work.

Final thanks also to the people that support me during these three years, above all: my mother, my father, Alvaro Brittoli, Martina Pasquini and Filippo Mazzinghi.

BIBLIOGRAPHY

[1] SPES Web Page (`http://web.infn.it/spes`).

[2] J. J. Valiente-Dobón *et al.*, LNL-INFN Annual Report, 95 (2014).

[3] S. Akkoyun *et al.*, Nucl. Instrum. Methods Phys. Res. A **668**, 26 (2012).

[4] R. Brun and F. Rademakers, Nucl. Instrum. Methods Phys. Res. A **389** 81 (1997).

[5] T. Czosnyka, D. Cline and C. Y. Wu, Bull. Am. Phys. Soc. **28**, 745 (1983). `http://www.slcj.uw.edu.pl/gosia`

[6] S. Agostinelli *et al.*, Nucl. Instrum. Methods Phys. Res. A **506**, 250 (2003).

[7] ISOLDE Web Page (`http://isolde.web.cern.ch`).

[8] ISAC Web Page (`http://www.triumf.ca/research-program/research-facilities/isac-facilities`).

[9] RIBF Web Page (`http://www.nishina.riken.jp/RIBF`).

[10] LNL Web Page (`http://www.lnl.infn.it`).

[11] H. Yukawa, Proc. Phys. Math. Soc. Jap. **17**, 48 (1935).

[12] J. F. Berger, M. Girod and D. Gogny, Nucl. Phys. A **428**, 23 (1984).

[13] T. H. R. Skyrme, Phil. Mag. **1**, 1043 (1956).

[14] J. D. Holt, T. Otsuka, A. Schwenk and T. Suzuki, J. Phys. G: Nucl. Part. Phys. **39**, 085111 (2012).

[15] T. Otsuka, T. Suzuki, J. D. Holt, A. Schwenk and Y. Akaishi, Phys. Rev. Lett. **105**, 032501 (2010).

[16] S. S. M. Wong, *Introductory Nuclear Physics*, John Wiley and sons, 1998.

[17] `http://www.triumf.info/hosted/iupap/icnp/result2a.html`.

[18] G. Gneuss, U. Mosel, and W. Greiner, Phys. Lett. B **30** 397 (1969).

[19] R. F. Casten, *Nuclear Structure from a Simple Perspective*, Oxford Science Publications, 2000.

[20] F. Iachello and A. Arima, *The interacting boson model*, Cambridge University Press, 1987.

[21] NuPECC Long Range Plan 2017, *Perspectives in Nuclear Physics* (`http://www.nupecc.org`).

[22] W. Leidemann and G. Orlandini, Prog. Part. Nucl. Phys. **68**, 158 (2013).

[23] L. Coraggio, A. Covello, A. Gargano, N. Itaco and T. T. S. Kuo, Prog. Part. Nucl. Phys. **62**, 135 (2009).

[24] J. L. Egido, Phys. Scr. **91**, 073003 (2016).

[25] H. Hergert, S. K. Bogner, T. D. Morris, A. Schwenk and K. Tsukiyama, Phys. Rep. **621** 165 (2016).

[26] R. Machleidt, Phys. Rev. C **63**, 024001 (2001).

[27] R. B. Wiringa, V. G. J. Stoks and R. Schiavilla, Phys. Rev. C **51**, 38 (1995).

[28] R. Machleidt and D. R. Entem, Phys. Rep. **503**, 1 (2011).

[29] J. P. Elliott *et al.*, Nucl. Phys. A **121**, 241 (1968).

[30] S. Bogner, T. T. S. Kuo and L. Coraggio, Nucl. Phys. A **684**, 432c (2001).

[31] M. Schumaker, Ph.D. Thesis, 2009.

[32] A. Bohr and B. R. Mottelson, *Nuclear Structure Volume II*, World Scientific, 1998.

[33] L. Fortunato, Eur. Phys. J. A **26**, 1 (2005).

[34] D. N. Simister *et al.*, J. Phys. G, 1127 (1978).

[35] M. Koizumi *et al.*, Eur. Phys. J. A **18**, 87 (2003).

[36] J. Leske *et al.*, Phys. Rev. C **73**, 064305 (2006).

[37] E. Browne and J. K. Tuli, Nuclear Data Sheets A = 66, 1093 (2010).

[38] C. H. Druce, J. D. McCullen, P. D. Duval and B. R. Barrett, J. Phys. G: Nucl. Phys. **8**, 1565 (1982).

[39] R. 0. Sayer, J. S. Smith III and W. T. Milner, Atomic Data and Nuclear Data Tables **15**, 85 (1975).

[40] A. Gade, H. Klein, N. Pietralla, and P. von Brentano, Phys. Rev. C **65**, 054311 (2002).

[41] T. R. Rodrigues, *Private communication.*

[42] W. Z. Jiang, Z. Z. Ren, T. T. Wang, Y. L. Zhao and Z. Y. Zhu, Eur. Phys. J. A **25**, 29 (2005).

[43] Y. Toh *et al.*, J. Phys. G **27**, 1475 (2001).

[44] Y. Toh *et al.*, Eur. Phys. J. A **9**, 353 (2000).

[45] B. Kotlinski *et al.*, Nucl. Phys. A **519**, 646 (1990).

[46] A. E. Kavka *et al.*, Nucl. Phys. A **593**, 177 (1995).

[47] L. M. Robledo, EPJ Web of Conferences **66**, 02091 (2014).

[48] L. M. Robledo, Eur. Phys. J. A **52**, 300 (2016).

[49] M. Honma *et al.*, Phys. Rev. C **69**, 034335 (2004).

[50] O. Kenn *et al.*, Phys. Rev. C **65**, 034308 (2002).

[51] K. Moschner *et al.*, Phys. Rev. C **82**, 014301 (2010).

[52] M. Honma *et al.*, Phys. Rev. C **80**, 064323 (2009).

[53] D. Mücher *et al.*, Phys. Rev. C **79**, 054310 (2009).

[54] O. Kenn *et al.*, Phys. Rev. C **63**, 064306 (2001).

[55] I. N. Boboshin and S. Yu. Komarov, Bulletin of the Russian Academy of Sciences: Physics **73**, 1446 (2009).

[56] O. Sorlin *et al.*, Phys. Rev. Lett. **88**, 092501 (2002).

[57] A. Chakraborty *et al.*, Phys. Rev. C **83**, 034316 (2011).

[58] M. Koizumi *et al.*, Nucl. Phys. A **730**, 46 (2004).

[59] M. Koizumi *et al.*, JAERI Tandem Annual Report 2002, 22 (2003).

[60] V. de Walle *et al.*, Phys. Rev. C **79**, 014309 (2009).

[61] M. Niikura *et al.*, Phys. Rev. C **85**, 054321 (2012).

[62] C. Louchart *et al.*, Phys. Rev. C **87**, 054302 (2013).

[63] W. D. Hamilton, *The Electromagnetic Interaction in Nuclear Spectroscopy*, North-Holland, 1975.

[64] T. Kibédi and R. Hspear, Atomic Data and Nuclear Data Tables **80**, 35 2002.

[65] L. C. Biedenharn and P. J. Brussaard, *Coulomb Excitation*, Clarendon Press (Oxford), 1965.

[66] B. Mottelson, *Intern. Phys. Conf.*, Copenhagen, 1952.

[67] T. Huus and C. Zupancic, Mat. Fys. Medd. Dan. Vid. Selsk **28**, No. 1 (1953).

[68] C. I. McClelland and C. Goodman, Phys. Rev. **91**, 760 (1953).

[69] F. S. Stephens, R. M. Diamond and I. Perlman, Phys. Rev. Lett. **3**, 435 (1959).

[70] C. Y. Wu *et al.*, Nucl. Phys. A **607**, 178 (1996).

[71] K. Alder and A. Winther, *Coulomb Excitation: A Collection of Reprints*, Academic Publishing (New York) 1966.

[72] arXiv preprint arXiv:1506.04633, Jun 2015.

[73] A. Göergen, J. Phys. G: Nucl. Part. Phys. **37**, 103101 (2010).

[74] E. Clément *et al.*, Phys. Rev. Lett. **116**, 022701 (2016).

[75] K. Hadyńska-Klęk *et al.*, Phys. Rev. Lett. **117**, 062501 (2016).

[76] L. P. Gaffney *et al.*, Nature **497**, 199 (2013).

[77] K. Alder and A. Winther, *Electromagnetic Excitation*, North-Holland, 1975.

[78] D. Cline, Annu. Rev. Nucl. Part. Sci. **36**, 683 (1986).

[79] K. Alder, A. Winther, K. Dan. Vidensk and Selsk, Mat. Fys. Medd. **32**, No. 8 (1960).

[80] J. de Boer and J. Eichler, *The Reorientation Effect*, in: M. Baranger, E. Vogt (eds), *Advances in Nuclear Physics*, Springer, Boston, MA (1968).

[81] M. Rotenberg, R. Bivins, N. Metropolis and J. Wooten, *The 3j and 6j Symbols*, The Technology Press, Cambridge, Mass. (1959).

[82] K. Wrzosek-Lipska *et al.*, Phys. Rev. C **86**, 064305 (2012).

[83] K. Wrzosek-Lipska and L. P. Gaffney, J. Phys. G: Nucl. Part. Phys. **43**, 024012 (2016).

[84] J. F. Ziegler, M. D. Ziegler and J. P. Biersack, Instrum. Methods in Phys. Res. B **268**, 1818 (2010).

[85] D. Cline *et al.*, *Gosia User Manual for Simulation and Analysis of Coulomb Excitation Experiments*, Rochester, NY, US, 2012.
`http://www.pas.rochester.edu/~cline/Gosia/Gosia_Manual_20120510.pdf`

[86] C. Rossi Alvarez, Nuclear Physics News **3**, 10 (1993).

[87] Ö. Skeppstedt *et al.*, Nucl. Instrum. Methods Phys. Res. A **421**, 531 (1999).

[88] W. Męczyński *et al.*, Nucl. Instrum. Methods Phys. Res. A **580**, 1310 (2007).

[89] D. Testov *et al.*, LNL-INFN Annual Report, 73 (2014).

[90] D. Mengoni, J. A. Dueñas and M. Assie, LNL-INFN Annual Report, 58 (2011).

[91] G. Benzoni *et al.*, LNL-INFN Annual Report, 84 (2015).

[92] A. Goasduff *et al.*, LNL-INFN Annual Report, 91 (2015).

[93] L. Kaya *et al.*, Nucl. Instrum. Methods Phys. Res. A **855**, 109 (2017).

[94] M. W. Simon, Nucl. Instrum. Methods Phys. Res. A **205**, 109 (2000).

[95] P. Reiter *et al.*, Nuclear Physics A **701**, 209c (2002).

[96] D. Testov *et al.*, *to be published.*

[97] JUNKOSHA Web Page (`http://www.junkosha.co.jp`).

[98] D. Barrientos *et al.*, arXiv:1406.3925v1.

[99] D. C. Radford , Nucl. Instrum. Methods Phys. Res. A **361**, 297 (1995).

[100] National Nuclear Data Center `http://www.nndc.bnl.gov`

[101] G. Lindsrom, Nucl. Instrum. Methods Phys. Res. A **512** (2003) 30.

[102] CSM Technical Proposal, CERN/LHCC794-38, 1994.

[103] E. Fretwurst *et al.*, Nucl. Instrum. Methods Phys. Res. A **288**, 1 (1990).

[104] M. Jakšić *et al.*, Nucl. Instrum. Methods Phys. Res. B **231**, 502 (2005).

[105] S. Barlini *et al.*, Nucl. Instrum. Methods Phys. Res. A **707**, 89 (2013).

[106] M. Kurokawa *et al.*, IEEE Transactions on Nuclear Science NS-42 (1995) 163.

[107] G. F. Knoll, *Radiation Detection and Measurement*, John Wiley and Sons, 1999.

[108] A. Camaiani, Master Thesis, 2013.

[109] CAEN Web Page (`http://www.caen.it`).

[110] M. Mayer and T. F. Silva, Nucl. Instr. Meth. B **406**, 75 (2017).

[111] J. Lindhard, M. Scharff, and H. E. Schiott, Mat. Fys. Medd. Dan. Ed. Selsk. **33**, 1 (1963).

[112] M. Moll, Ph.D. Thesis, 1999.

[113] SR-NIEL Web Page (http://www.sr-niel.org).

[114] D. Bechevet *et al.*, Nucl. Instrum. Methods Phys. Res. A **479**, 487 (2002).

[115] L. Kaya *et al.*, Nucl. Instrum. Methods Phys. Res. A **479**, 487 (2002).

[116] D. Torresi *et al.*, Nucl. Instrum. Methods Phys. Res. A **855**, 109 (2017).

[117] S. Bettarini, Bachelor Thesis, 2015.

[118] J. Yorkston *et al.*, Nucl. Instrum. Methods Phys. Res. A **262**, 353 (1987).

[119] V. Eremin *et al.*, Nucl. Instrum. Methods Phys. Res. A **500**, 121 (2003).

[120] M. Ogihara *et al.*, Nucl. Instrum. Methods Phys. Res. A **251**, 313 (1986).

[121] G. Tăbăcaru *et al.*, Nucl. Instrum. Methods Phys. Res. A **428**, 379 (1999).

[122] O. B. Tarasov and D. Bazin, Nucl. Instrum. Methods Phys. Res. B **266**, 4657 (2008).

[123] I. Sugai, S. Takaku, T. Hatori and T. Hasegawa, Nucl. Instrum. Methods **167**, 135 (1979).

[124] G. Blondiaux *et al.*, Nucl. Instrum. Methods Phys. Res. **227**, 19 (1984).

[125] K. Wrzosek-Lipska, Ph. D. Thesis, 2010.

[126] K. Hadyńska-Klęk *et al.*, Heavy Ion Laboratory Annual Report 2008, 27 (2009).

[127] A. Perego and L. Carraresi, *Not published.*

[128] D. Bazzacco, *Not published.*

[129] T. Kibédi, T. W. Burrows, M. B. Trzhaskovskaya, P. M. Davidson and C. W. Nestor, Nucl. Instrum. Methods Phys. Res. A **589**, 202 (2008).

[130] T. R. Rodrıguez and J. L. Egido, Phys. Rev. C **81**, 064323 (2010).

[131] P. Ring and P. Schuck, *The nuclear many body problem*, Springer-Verlag, Berlin, 1980.

[132] T. Bengtsson, I. Ragnarsson and S. Aberg, Computational Nuclear Physics **1**, 51 (1991).

[133] S. M. Lenzi, F. Nowacki, A. Poves and K. Sieja, Phys. Rev. C **82**, 054301 (2010).

[134] P. K. Raina, Phys. Rev. C **37**, 1427 (1988).

[135] T. Togashi, Y. Tsunoda, T. Otsuka and N. Shimizu, Phys. Rev. Lett. **117**, 172502 (2016).

LIST OF FIGURES

1.1 Logarithmic nuclide chart in which the regions of applicability of some of the modern theoretical approaches, used to describe the nuclear structure, are shown. To date, ab initio approaches are being extended up to heavy mass nuclei, as shown in figure 1.2. Figure taken from [17]. 9

1.2 Nuclides chart with the reach of *ab initio* calculations in 2005 and 2015. Nuclei (including potentially unbound isotopes), for which *ab initio* calculations based on high-precision nuclear interactions exist, are highlighted. Figure taken from [25]. 10

1.3 Schematic diagram of single-particle energy levels for spherical shell model. The break of degeneracy caused by the angular momentum and spin-orbit terms, which produces the emergence of the magic number in the shell closure, is also visible. The energy values in the first set are the ones of the simple harmonic oscillator. Figure taken from [31]. 12

1.4 Quadrupole deformed shapes as a function of the Hill-Wheeler parameters. Different colors identify the axes of the intrinsic reference frame (green for z, red for y and blue for x). Figure taken from [33]. 16

1.5 Comparison between the low-lying ^{66}Zn experimental decay scheme and the corresponding harmonic vibrational model prediction. The energy of the first 2^+ state has been fixed to the experimental value. In red are shown the predicted $E2$ transitions between the states and the corresponding $B(E2)$ values normalized to $B\left(E2; 2_1^+ \longrightarrow 0_1^+\right)$. The experimental data are taken from [37], more recent results are reported in the text. 18

1.6 The energy levels of low-lying states for even Zn isotopes are reported as a function of the mass number. Data are taken from [37]. Only adopted values with definite spin and parity assignments have been considered. . . . 19

1.7 Single particle orbitals relevant for the Zn isotopes. The Fermi minimum configuration for ^{66}Zn, which is discussed in this thesis, is also shown, together with the three ^{40}Ca, ^{48}Ca, ^{56}Ni closed core configurations. 20
1.8 Experimental excitation energies of the 2_1^+ states (a) and $B\left(E2; 2_1^+ \longrightarrow 0_1^+\right)$ values (b) in even nickel isotopes reported as a function of the mass number. The typical parabolic trend of both the quantities is a signature of the magic character of ^{56}Ni and ^{68}Ni. Figure adapted from [57]. 21
1.9 $B\left(E2\right)$ values of some of the transitions relevant for this work and $Q_s\left(2_1^+\right)$ value for the Zn isotopic chain are reported as a function of the mass. Different measurements corresponding to the same nucleus have been slightly mass-shifted in order to make comparison easier. The adopted values reported in [37] are shown in black. More recent measurements are reported with colors: green [35, 58, 59], blue [60], red [51], orange [61] and purple [62]. In order to simplify the comparison with the large adopted value in ^{66}Zn, the $B\left(E2; 2_2^+ \longrightarrow 2_1^+\right)$ values are reported in logarithmic scale. Only model-independent analyses have been considered. 22
1.10 Low-energy decay pattern of ^{66}Zn of interest for the present work. Levels are shown in black, while transitions in blue (all the values are given in keV). Data taken from [37]. The transition $3_1^- \longrightarrow 0_1^+$ is reported in gray since it has never been directly observed. However, the $B\left(E3; 3_1^- \longrightarrow 0_1^+\right)$ was measured in an electron scattering measurement, as reported in [64]. . 23

2.1 Safe energy, defined in equation 2.4 as a function of the scattering angle in the center-of-mass system. The plot refers to the ^{66}Zn experiment discussed in this thesis, where an enriched ^{208}Pb target was used. The chosen beam energy of 240 MeV is also shown. 27
2.2 Sommerfeld parameter η calculated for different combinations of projectiles and target nuclei. The pink star marks the η parameter calculated for the Coulomb excitation of ^{66}Zn experiment. 28
2.3 (a) The differential cross-section function $df_{E2}\left(\theta, \xi\right)$ is shown, as a function of the center-of-mass scattering angle, for different values of the adiabaticity parameter. The curves have been normalized to unity at $\theta_{CM} = 180°$. (b)-(c) The total cross-section functions $df_{E\lambda}$ and $df_{M\lambda}$ are shown with respect to the adiabaticity parameter and the multipolarity λ. The pictures have been adapted from [77]. The values related to the ^{66}Zn experiment are shown in orange. 31

2.4 The quantity $K(\theta_{CM}, \xi)$ is reported as a function of ξ for different values of θ_{cm}. The picture has been adapted from [77]. The values related to the ^{66}Zn experiment are shown in orange. 34
2.5 A schematic illustration of the $E2$ matrix elements necessary in order to evaluate Q (left) and δ (right) for a $0^+_{g.s.}$ state using the quadrupole sum rule method. Figure taken from [83]. 36
2.6 Coulomb excitation kinematics in the center-of-mass system (a) and in the laboratory system (b). The impact parameter defined in 2.1 is also shown. 37
2.7 Typical experimental setup used in Coulomb excitation measurements when γ-particle coincidences are detected. Figure taken from [83]. 40

3.1 Left: the experimental setup used for the ^{66}Zn experiment composed of the GALILEO and SPIDER arrays. Five $LaBr_3$:Ce detectors are also present, not used in this experiment. Right: detail of the SPIDER array inside the reaction chamber of GALILEO. 43
3.2 View of the GALILEO array in the final configuration. The mechanical structure holding the HPGe detectors with their BGO shields is also shown. In this picture, the 10 triple cluster detectors are positioned at 90 degrees relative to the beam direction. Also some details of the automatic cooling system, used by the HPGe detectors, are visible. 45
3.3 Left: the GALILEO array in the ^{66}Zn experiment configuration. Right: schematic view of the angular positions of the GALILEO HPGe detectors with respect to the beam direction. 46
3.4 Picture (left) and schematic view (right) of one of the SPIDER detector from the junction side. The 8 strips and the guard ring are visible. In the schematic view, the labelling of the SPIDER strips that is used in this thesis is shown. 47
3.5 Half SPIDER array mounted in the disk configuration. 47
3.6 Alpha spectrum relative to strip 0, obtained using a triple alpha source (^{239}Pu + ^{241}Am + ^{244}Cm). The spectrum has been obtained in optimal conditions, in a dedicated test station. 48
3.7 Left: the SPIDER array in the cone configuration inside the GALILEO vacuum chamber (the target holder is also visible). Right: 3D-printed aluminium holder used to arrange SPIDER inside the GALILEO vacuum chamber. 49
3.8 Geometrical description of one SPIDER detector in the cone configuration. The z-axis is opposite to the beam direction and **O** is the target position. . 49

3.9 Simulated γ–ray spectrum for the Coulomb excitation of the ^{66}Zn experiment discussed in the present thesis. 51
3.10 Simulated γ–ray FWHM as a function of the polar (nθ) and azimuthal (nϕ) segmentation in typical experimental conditions for Coulomb excitation experiments using stable beams (see the text for the details). In red is shown the value of the FWHM for the SPIDER configuration used in the ^{66}Zn experiment. 52
3.11 Experimental setup used for the SPIDER commissioning at the INFN LABEC laboratory. Two HPGe detectors and 4 SPIDER detectors, positioned at backward angles, where used in this test. 53
3.12 Particle energy spectra corresponding to a SPIDER strip positioned around $\theta = 120°$. The backscattered ^{7}Li ions impinging on the ^{27}Al target and on the tantalum beam dump positioned at ~ 10 cm from the target are indicated. 54
3.13 Left: the total γ–ray spectrum acquired during the ^{7}Li experiment. Right: the same part of the spectrum after the Doppler correction procedure. . . . 55
3.14 Scheme of the acquisition system of GALILEO and SPIDER at LNL. Pre is the preamplifier, RU is the Readout Unit, LF is the Local Filter, EB is the Event Builder, EM is the Event Merger, GF is the Global Filter and GTS is the Global Trigger and Synchronization system. 57

4.1 Non-linearity effect in one of the HPGe GALILEO detectors (SC4, $\theta = 152°$, $\phi = 288°$). See the text for details. 62
4.2 Left: matrix used for the pileup rejection, in which the short-trace energy is reported as a function of the long-trace one. Right: same picture after applying the pileup rejection procedure. 63
4.3 Total peak statistics (left) and peak-to-total ratio (right) reported as a function of the BGO energy threshold (given in arbitrary units). The plots refer to one GALILEO detector (SC2, $\theta = 152°$, $\phi = 144°$) and to a ^{60}Co source (the sum of the peaks corresponding to the 1173.2 keV and 1332.5 keV transition have been considered). 64
4.4 Absolute photopeak efficiency for the entire GALILEO array as a function of the γ–ray energy. The measured efficiencies are reported in blue, while the fitted function is shown in red. The picture refers to 24 HPGe detectors, since SC0 was not used in the ^{66}Zn experiment. 65

4.5 Energy calibration spectrum acquired by one SPIDER strip. The α-particles emitted by a triple alpha source ^{239}Pu+^{241}Am+^{244}Cm have been detected together with a set of signals, equally spaced in amplitude, provided by a pulser. Non-linearity effects are visible starting from channel $\sim$ 5000. . . . 67
4.6 Signal amplitude as a function of the channel number for the first 6 pulser peaks, measured by one SPIDER strip (D5S3, $\theta = 144.2°$). The data are shown in blue (the error bars are smaller than the marker size), while the linear fit is shown in red. 68
4.7 Calculated energy as a function of the channel number for a single SPIDER strip (the same of figure 4.6). The data are shown in blue (the error bars are smaller than the marker size), while the 6th-order polynomial fit is shown in red (continuous). The first data point (channel $\sim$ 350) is the considered peak of to the α-source. The effect of non-linearity of the SPIDER preamplifiers is visible above an energy of $\sim$ 70 MeV (dashed line). 69
4.8 Left: GALILEO energy as a function of the time. The events with time equal to zero are highlighted in orange. The dashed line is plotted to guide the eyes, and it is not the fit result. Right: the same figure after the time extrapolation. The red arrow represents the shift of the events with time zero in the extrapolated position. 70
4.9 Left: time difference between the reference HPGe detector (SC1) and the other detectors (identified by their domain), γ-γ coincidences have been considered in this matrix. Right: the same plot after the time alignment procedure. 71
4.10 Time difference spectrum of γ-particle coincidences. The time window used for the Coulomb excitation coincidences is highlighted in green, the two time windows used for the random coincidences subtraction in orange. 71
4.11 Possible acquired events (see section 3.4 for the physical meaning): 1) γ-particle, 2) γ-particle-particle, 3) γ-γ-particle, 4) particle singles, 5) γ singles, 6) particle-particle, 7) γ-γ. Higher multiplicity events, which have negligible statistics, are not considered. 72
4.12 Example of energy spectrum relative to a SPIDER strip ($\theta = 158.5°$). The back-scattered projectiles and the noise contribution are visible. 73
4.13 Scheme of the 4 limit cases of ^{66}Zn Coulomb excitation inside the target. The black dots represent the scattering process (the excitation), the coloured dots represent the de-excitation. The target thickness is intentionally exaggerated in order to better identify the different scattering positions. 74

4.14 Example of 3D plot used to determine the SPIDER angles, referred to one strip. The standard deviation of the fitted peak in the γ–ray spectra is reported as a function of the two offset $\Delta\theta_p$, $\Delta\phi_p$ (see the text for the details). 75
4.15 The center-of-mass angles of each SPIDER strip are reported using blue dots. The misalignment with respect to the beam axis is visible. 76
4.16 Standard deviation of the fitted peak as a function of the energy calibration offset ΔE^{cal}_{lab} for one SPIDER strip. The fit results are shown, together with error bars, in blue. The polynomial fit, from which the minimum FWHM is obtained, is shown in red. 77
4.17 Left: calibration offset ΔE^{cal}_{lab} for the different SPIDER strips, as a function of their center-of-mass polar angle obtained from the Doppler correction minimization. An error of ~ 1 MeV has been estimated considering different sets of data. Right: energy difference between the mean energy values obtained from the Doppler correction procedure E'_m and the energy registered in the SPIDER strips. 78
4.18 The detected energies, related to the front surface scattering of ^{66}Zn on ^{208}Pb, are reported using blue dots for each SPIDER strips. The misalignment with respect to the beam axis is visible, as in the case of figure 4.15. 79
4.19 γ–ray energy spectra around 1 MeV and 2.5 MeV acquired in coincidence with the back-scattered ^{66}Zn ions. In the upper panels (No DC) no Doppler correction has been applied, in the middle panels (DC Proj.) the Doppler correction has been applied for the projectile nuclei while in the lower panels (DC Target) for the target nuclei. The spectra are not random background subtracted. 81

5.1 Depth distribution of the number of vacancies created by 2 MeV ^{4}He and ^{16}O ions in silicon according to SRIM calculations [84]. The figure is taken from [104]. It is visible how the vacancies are mainly produced at the end of the range. 84
5.2 Leakage current density J as a function of the backscattered ^{66}Zn flux. The figure refers to the SPIDER strip D4S7 ($\theta = 125.5°$). The data points refer to the start of each partial run (the file in which data are stored changed every $2-4$ h). 85

5.3 The damage factor α as a function of the center-of-mass polar angle of the SPIDER strips is reported in blue for each strip, a mean value for the strips of the same ring is shown in red. The theta angle is slightly different for strips in the same ring due to the imperfect centering of SPIDER inside the GALILEO vacuum chamber. 86
5.4 Left: a simulated energy spectrum for a SPIDER strip positioned at $\theta = 158.5°$ is shown in red, considering the real conditions of the ^{66}Zn experiment except for the target thickness, 1 mg/cm^2. The same spectrum, simulated for a thin target, is reported in green. Right: schematic view of three different impact position of the beam on the target. 87
5.5 Example of fit procedure on an experimental particle spectra acquired by SPIDER, shown in blue. The fitted function (which is reported in equation 5.2) is shown in red, while its free parameters are reported in green. 88
5.6 Left: particle energy spectra acquired by one of the less-irradiated SPIDER strip (D6S0 $\theta = 158.5°$). Right: the same for one of the most-irradiated SPIDER strip (D4S7, $\theta = 125.5°$). Spectra recorded at the beginning and at the end of the experiment are reported in black and red respectively. . . 89
5.7 Comparison between the α-particle energy spectra acquired with an α-source in the target position. In black the energy spectrum before the ^{66}Zn experiment is shown, in red the same after the experiment. The same calibration has been used for the two spectra. One of the most irradiated SPIDER strip is considered (D4S7, $\theta = 125.5°$). 90
5.8 Comparison between the acquired signals at the beginning (black) and at the end (red) of the ^{66}Zn experiment. One of the most irradiated SPIDER strip is considered (D4S7, $\theta = 125.5°$). 90
5.9 Pulse-height correlation matrices, relative to particle-particle coincidences considering the entire SPIDER array. Left: matrix obtained with low energy thresholds. Right: corresponding matrix with increased energy thresholds. The regions with the larger number of counts are labelled from A to E. The matrices refer to different acquisition times and mean beam currents, in particular, the matrix on the right shows twice the statistics of the one on the left. 92
5.10 Examples of negative polarity (left) and noise or cross-talk signals (right) acquired during the ^{66}Zn experiment. A comparison with signals corresponding to backscattered ^{66}Zn ions can be made considering figure 5.8. . . 93

5.11 Left: number of counts registered in the SPIDER strips as a function of the energy and of the domain number. The events are obtained requiring a time coincidence with a given strip (D2S4), in which only scattered ^{66}Zn ions have been selected. Right: the integrals over the low-energy region ($0 - 2$ MeV) of the left figure are reported for the detector D2. 94
5.12 Possible acquired events considering the energy registered in the SPIDER strips: 1) real coincidence, 2) real coincidence with a low-amplitude signal, 3) true double hit event. 95
5.13 The same plot as reported in figure 4.7, with the addition of two points associated to the scattering of the ^{66}Zn beam on the ^{124}Sn and ^{208}Pb target front surfaces. The discrepancy between the calculated energies, obtained thorough the equation 2.43, and the detected ones, obtained from the calibration described in 4.2.1, is also shown. 96
5.14 The γ–ray spectrum obtained by projecting the γ-γ matrix with a gate on the $2_1^+ \longrightarrow 0_{g.s}^+$ in ^{76}Kr. A rough Doppler correction, assuming that all the produced ^{76}Kr are emitted in the forward direction, is applied. The coincidence transition up to spin 12^+ are visible. Other transitions, not associated from ^{76}Kr, are present due to the fact that the spectrum is not background-subtracted. The decay scheme on the right has been taken from [100]. 97
5.15 Schematic picture of the build-up carbon layer effect on the particle energy detected by the SPIDER strips. The carbon layer is indicated in red, while the lead target is indicated in green. The two energy losses, the one before (ΔE_{entry}) and the one after the scattering (ΔE_{exit}) in the lead surface are indicated. 98
5.16 Experimental particle spectrum acquired by one of the SPIDER strips (red) analysed with the SIMNRA code [110] (the result is shown in black). The tail at low-energy is due to the target roughness. 100
5.17 Picture of the ^{208}Pb target taken at the end of the experiment (the diameter of the hole in the aluminium frame is 1 cm). Three different regions are clearly visible. 101
5.18 Picture of the setup used for the RBS measurement of the ^{208}Pb target. One of the used silicon detectors is visible. 102

5.19 Energy spectra acquired by one of the used silicon detectors in the target RBS measurement at LABEC. The irradiated region and the different components are indicated. A portion of the spectra close to the ^{208}Pb region has been reduced by a factor of 10^2, in order to make an easier comparison. Region 1), 2), 3) of the irradiated target are relative to figure 5.17. The measurements of the irradiated target show twice the statistics of the ones relative to the non-irradiated one. 103

6.1 Total γ–ray energy spectrum acquired by GALILEO, in coincidence with the back-scattered ^{66}Zn ions detected by SPIDER. The spectrum is random-background subtracted and the Doppler correction has been applied for ^{66}Zn nuclei. The peaks corresponding to the observed transitions are indicated (cfr. figure 1.10). The total number of counts of the red transitions has been divided into eight different angular ranges, exploiting the full segmentation of SPIDER. Since the number of counts of the transitions indicated in green is relatively low, only two different scattering ranges have been considered (see the schematic picture of SPIDER on top right). . . . 106

6.2 Two examples of number of counts estimation for the $2_1^+ \longrightarrow 0_1^+$ (left) and $0_2^+ \longrightarrow 2_1^+$ (right) transitions (the spectra refers to a single SPIDER scattering angle range). Left: a Gaussian function convoluted with an exponential function on the left side of the peak has been used (shown in purple). The background has been estimated with a step function (shown in green). Right: only an integral has been performed, in purple is shown the region of integration and in green the background regions (each of them has been divided by two in order to normalize to the same energy range). . 107

6.3 Level scheme of ^{66}Zn used in the GOSIA calculations. This is the same as the one reported in figure 1.10, with the addition of the "buffer states" states 5_1^-, 2_4^+ and 4_3^+ and their de-exciting transitions (marked in red). Also the $4_1^+ \longrightarrow 2_2^+$ has been added (see the text for the details). The transitions considered for the preliminary analysis described in the text, aimed at discriminating between different values of $\tau\left(4_1^+\right)$, are shown in green. 108

6.4 Relative population of the 2_2^+ state as a function of the projectile scattering angle (the sum of the relative populations of all the states considered in the level scheme reported in figure 1.10 is 1). The calculations have been performed for three different values of $Q_s\left(2_1^+\right)$. 111

6.5 Results of the simplified analysis considering only the 0_1^+, 2_1^+, 4_1^+ and 6_1^+ states. Left panel: χ^2 value as a function of the absolute value of the $\langle 4_1^+||E2||2_1^+\rangle$ reduced matrix element (black dots); the solid line is a polynomial fit. The dashed, horizontal line marks the $\chi^2 = \chi^2_{min} + 1$ level, corresponding to 1σ error bar. Right: comparison of the $|\langle 4_1^+||E2||2_1^+\rangle|$ reduced matrix element obtained in the present simplified analysis with the values previously obtained by M. Koizumi *et al.* [35] and K. Moschner *et al.* [51]. 112

6.6 Comparison between experimental (dots) and calculated (continuous lines) γ–ray yields for the three most intense transitions observed in the ^{66}Zn experiment. These yields are integrated over the target thickness and the SPIDER rings angular coverage and normalized to the $2_1^+ \longrightarrow 0_1^+$ transition. 115

6.7 Left: Potential Energy Surface (PES) resulting from BMF calculations. Right: Collective Wave Function (CWT) of the ^{66}Zn ground state. The orange/yellow region represents the largest contribution to the wave function, while blue the smallest one. The deformation parameters of the ground state obtained in this work are also shown in red. 118

6.8 Proton and neutron occupation numbers resulting from SM calculations for the 0_1^+, 0_2^+, 4_1^+ and 4_2^+ states. 121

7.1 Energy of the 2_1^+ and 2_2^+ states in Zr isotopes, as a function of the neutron number. Symbols are theoretical results reported in [135] with the shape classification as shown in the legend. Solid lines denote experimental data [100]. 125

LIST OF TABLES

3.1 In column 2 the angle between the z-axis and the $\mathbf{Q} - \mathbf{O}$ vector, where $\mathbf{Q}$ is the position in the middle of each strip, is shown (refer to figure 3.8). This value can be considered as the center-of-mass of the strips with good approximation. In column 3 and 4 are shown the polar and solid angular coverage of each strip. 50

6.1 Spectroscopic values assumed in the present analysis. Values taken from [100]. 110

6.2 Left: matrix elements obtained in this work. A positive sign has been assigned to the ones reported in brackets, while sensitivity was not sufficient to determine the one reported as $\pm$. Right: $B(E2)$ and Q_s values deduced from the matrix elements reported on left. 113

6.3 Spectroscopic data deduced in the present analysis. 116

6.4 Some of the reduced transition probabilities measured in this work are compared with those already reported in previous measurements. 117

6.5 Comparison between the experimental results obtained in this work and the ones calculated using the SM (see the text for the details) and the BMF approach. 120